

INDUCTION PLASMA SYNTHESIS OF Mg-Ni NANOPARTICLES

A THESIS SUBMITTED TO
THE GRADUATE SCHOOL OF NATURAL AND APPLIED SCIENCES
OF
MIDDLE EAST TECHNICAL UNIVERSITY

BY

BURAK AKTEKİN

IN PARTIAL FULFILLMENT OF THE REQUIREMENTS
FOR
THE DEGREE OF MASTER OF SCIENCE
IN
METALLURGICAL AND MATERIALS ENGINEERING

SEPTEMBER 2013

Approval of the thesis:

INDUCTION PLASMA SYNTHESIS OF Mg-Ni NANOPARTICLES

submitted by **BURAK AKTEKİN** in partial fulfillment of the requirements for the degree of **Master of Science in Metallurgical and Materials Engineering, Middle East Technical University** by,

Prof. Dr. Canan Özgen
Dean, Graduate School of **Natural and Applied Sciences** _____

Prof. Dr. C. Hakan Gür
Head of Department, **Metallurgical and Materials Engineering** _____

Prof. Dr. Tayfur Öztürk
Supervisor, **Metallurgical and Materials Engineering Dept., METU** _____

Examining Committee Members:

Prof. Dr. Macit Özenbaş
Metallurgical and Materials Engineering Dept., METU _____

Prof. Dr. Tayfur Öztürk
Metallurgical and Materials Engineering Dept., METU _____

Assoc. Prof. Dr. H. Emrah Ünalın
Metallurgical and Materials Engineering Dept., METU _____

Assist. Prof. Dr. Y. Eren Kalay
Metallurgical and Materials Engineering Dept., METU _____

B. Murat Kurtuluş, M.Sc.
Engineering Director, Roketsan Inc. _____

Date: 03.09.2013

I hereby declare that all information in this document has been obtained and presented in accordance with academic rules and ethical conduct. I also declare that, as required by these rules and conduct, I have fully cited and referenced all material and results that are not original to this work.

Name, Last Name : BURAK AKTEKİN

Signature :

ABSTRACT

INDUCTION PLASMA SYNTHESIS OF Mg-Ni NANOPARTICLES

Aktekin, Burak

M.Sc., Department of Metallurgical and Materials Engineering
Supervisor: Prof. Dr. Tayfur Öztürk

September 2013, 117 pages

There is a considerable interest in developing magnesium and magnesium alloys in the form of nanoparticles for hydrogen storage purposes. In the current study, induction thermal plasma was used to synthesize Mg-Ni nanoparticles. In this technique, precursors, which are normally powders, are fed to the thermal plasma where they are evaporated and nanoparticles are derived from condensation of this vapor in the quenching zone. RF induction plasma system used in the current work was operated at 25 kW and the reactor incorporated two injectors axially located in the torch, one from above and the other from below. This allowed injection of precursor powder in different temperature zones. Precursors used were mainly elemental Ni and Mg powders, but experiments were also carried out with pre-alloyed Mg₂Ni. The study has shown that Mg, Ni, Mg₂Ni with the additional amount of MgO phase could be synthesized in the form of nanopowders less than 100 nm in size. Upon feeding elemental powders Mg and Ni, Mg₂Ni could be synthesized; but, its fraction was quite low. The fraction was maximized and reached a weight fraction of 0.55 when Ni was fed from the top and Mg from the bottom injector the tip of which was located just below the quenching gas inlet. Hydrogenation of these powders showed fast kinetics, but there was no significant decrease in the dehydrogenation temperature. So as to further reduce the particle size and also to prevent oxidation, additional experiments were carried out where a fraction of argon used as carrier gas was replaced with methane. This has led to a core-shell structure in derived nanopowders. In the case of Ni, nanoparticles of varying sizes, e.g. 5-200 nm were encapsulated by 3-9 graphitic layers. For Mg, core-shell structure with a

comparable clarity was not observed. Instead, nanoparticles which had been embedded in carbonaceous matrix were obtained. The size of these particles could be as small as 5 nm.

Keywords: Induction thermal plasma, Magnesium, Mg₂Ni, Nickel, Hydrogen storage, Core-shell structure.

ÖZ

Mg-Ni NANOPARÇACIKLARIN ENDÜKSİYON PLAZMA İLE SENTEZİ

Aktekin, Burak

Yüksek Lisans, Metalurji ve Malzeme Mühendisliği Bölümü
Tez Yöneticisi: Prof. Dr. Tayfur Öztürk

Eylül 2013, 117 sayfa

Magnezyum ve magnezyum alaşımlarının nanoparçacık formda üretilmesi özellikle hidrojen depolama amaçlı uygulamalar açısından yoğun ilgi gören bir alandır. Bu çalışmada, Mg-Ni nanoparçacıklar endüksiyon ısıl plazma yöntemi ile üretilmişlerdir. Bu yöntemde, genellikle toz formunda olan başlangıç malzemesi ısıl plazmaya beslenmekte ve var olan yüksek sıcaklık sayesinde buharlaştırılmakta, sonrasında da reaktörün soğuk bölgesinde yoğunlaşarak nanoparçacıklara dönüşmektedir. Deneysel 25 kW gücünde RF endüksiyon plazma reaktörü kullanılarak gerçekleştirilmiş, reaktöre malzeme besleme işlemi üst ve alt enjektör kullanılmak sureti ile iki kaynaktan yapılmıştır. Beslemenin bu tarzda yapılması başlangıç tozlarının farklı sıcaklık bölgelerine beslenmesine olanak sağlamıştır. Deneysel başlangıç malzemesi olarak Ni ve Mg kullanılmış, bazı durumlarda önalaşımlandırılmış Mg_2Ni tozları da kullanılmıştır. Yapılan üretimle, 100 nm'den küçük Mg, Ni, Mg_2Ni nanoparçacıklar bir miktar MgO ile birlikte başarı ile üretilmişlerdir. Çalışma özellikle Mg_2Ni faz oranının artırılmasına odaklanmış ve bu oranın, nikelin üst enjektör ve magnezyumun alt enjektör ile beslenmesi durumunda önemli miktarda arttığı görülmüştür. Alt enjektörün soğutma gazı besleme noktasının hemen altında olması durumunda Mg_2Ni , 0.55'lik ağırlık oranı ile en yüksek değerine erişmektedir. Bu tarzda elde edilen Mg_2Ni , hidrürlenme davranışı açısından değerlendirilmiş, nanoparçacıkların hidrojenlenme ve hidrojeni bırakma reaksiyonlarına hızla girdikleri tespit edilmiştir. Bununla birlikte, çok küçük boyutlarına karşın hidrojen bırakma sıcaklığında önemli bir düşüş olmadığı, bu sıcaklığın klasik öğütme yöntemleri ile elde edilen Mg_2Ni 'den çok farklı olmadığı tespit edilmiştir.

Çalışmanın ikinci kısmında parçacık boyutunu daha düşük değerlere indirmek ve aynı zamanda oksitlenmeyi de engellemek amacıyla nanoparçacıklar metan kullanılmak sureti ile sentezlenmişlerdir. Bu çalışmada, taşıyıcı gaz olarak kullanılan argon gazının bir kısmı metan gazı ile değiştirilmiş ve üretim sonucunda, kabuklu yapıda nanoparçacıklar elde edilmiştir. Başlangıç tozu olarak Ni kullanıldığında, 5-200 nm boyutlarında Ni nanoparçacıklar 3-9 tabakalı grafitle sarmalanmış olarak rahatlıkla üretilebilmiştir. Mg ile yapılan üretimde benzer yapıda sarmalanmış parçacıklar elde edilememiş; ancak bunun yerine karbon bir anayapı içerisinde gömülü olarak, 5 nm boyutunda, çok küçük Mg parçacıklar elde edilmiştir.

Anahtar Sözcükler: Endüksiyon ısı plazma, Magnezyum, Mg₂Ni, Nikel, Hidrojen depolama, Kabuklu yapı.

Dedicated to my family

ACKNOWLEDGEMENTS

I would like to express my greatest appreciation to my supervisor Prof. Dr. Tayfur Öztürk for his valuable guidance and support throughout this thesis work. I am indebted for the inspiring and enlightening discussions we had together.

I would also like to thank to Assist. Prof. Dr. Y. Eren Kalay, especially for the material characterization and Assist. Prof. Dr. Gülhan Çakmak, for her valued suggestions. Their help is highly appreciated.

I acknowledge Serkan Yılmaz for his help and support during TEM studies and Necmi Avcı for his help in XRD measurements. It was a great chance to share the same laboratory with the members of ESM Research Group; I would like to thank to Fatih Pişkin, Alptekin Aydınlı, Ezgi Onur and Cavit Eyövge.

I owe great debt to my friends E. Erkan Aşık, Emre Mülazımoğlu, Aktöre Zeyrek, Yunus Uzer, Masumi Uehara, Çağdaş Yalçın, Aybüke Köseömeroğlu, Ayşe Mirza, Mustafa Topper, İrem Yüksekol, Alişan Genç, Neşe Ersoy and others who supported me during my thesis studies.

Finally, I would like to thank to my parents, Meliha Aktekin and Arif Aktekin for their endless support, patient and encouragement. I also thank to my brother, Yalçın Aktekin and his kind wife Didem Aktekin. I could not complete this work without their support.

TABLE OF CONTENTS

ABSTRACT.....	v
ÖZ.....	vii
ACKNOWLEDGEMENTS	x
TABLE OF CONTENTS	xi
LIST OF TABLES	xiii
LIST OF FIGURES	xiv
CHAPTERS	
1. INTRODUCTION	1
2. LITERATURE REVIEW	3
2.1 HYDROGEN STORAGE IN MAGNESIUM BASED METAL HYDRIDES	3
2.1.1 Introduction.....	3
2.1.2 Compositional Alterations	7
2.1.3 Structural Modifications.....	8
2.2. INDUCTION THERMAL PLASMA SYNTHESIS OF NANOPARTICLES	13
2.2.1 Introduction.....	13
2.2.2 Effect of Operating Conditions on the Plasma and Products	20
2.2.3. Overview of the Powders Synthesized by Induction Thermal Plasma	28
3. INDUCTION PLASMA SYNTHESIS OF Mg ₂ Ni.....	33
3.1 INTRODUCTION	33
3.2 EXPERIMENTAL.....	39
3.2.1 Materials	39
3.2.2 Induction Plasma System with Nanopowder Reactor.....	39
3.2.3 Materials Characterization	47
3.2.4 Determination of the Hydrogen Storage Properties	47

3.3 RESULTS & DISCUSSION	52
3.3.1 Synthesis of Nickel Nanoparticles.....	52
3.3.2 Synthesis of Nanoparticles from Pre-alloyed Mg ₂ Ni Powders	55
3.3.3 Synthesis of Nanoparticles from Mg and Ni Elemental Powders	56
3.3.4 Maximization of Mg ₂ Ni	57
3.3.5 Hydrogenation of Mg ₂ Ni Nanoparticles	62
3.4. CONCLUSIONS.....	65
4. CARBON ENCAPSULATION OF Mg-Ni NANOPARTICLES	67
4.1 INTRODUCTION.....	67
4.2 EXPERIMENTAL	74
4.3 RESULTS & DISCUSSION	74
4.3.1 Encapsulation of Nickel	74
4.3.2 Encapsulation of Magnesium Nanoparticles	78
4.3.3 Encapsulation of Mg ₂ Ni Nanoparticles	84
4.4 CONCLUSIONS.....	86
5. GENERAL CONCLUSIONS	87
REFERENCES.....	89
APPENDIX: SPARK DISCHARGE SYNTHESIS OF Mg-Ni NANOPARTICLES ...	105

LIST OF TABLES

TABLES

Table 3.1 Phases observed in products when five different mixtures were used as precursors (Umemoto and Udaka 1998).....	37
Table 3.2 Technical details of the pressure gauges used in the PCT apparatus.	49
Table 3.3 Elemental analysis results of the products collected from the powder collector (Pure Mg ₂ Ni: 45.3 wt% Mg – 54.7 wt% Ni).	59

LIST OF FIGURES

FIGURES

Figure 2.1 Volumetric and gravimetric storage capacities of various hydrogen storage materials and hydrocarbons (Schlapbach and Züttel 2001).	6
Figure 2.2 Hydrogen absorption behaviors of polycrystalline and nanocrystalline Mg ₂ Ni at 200°C (Zaluska <i>et al.</i> 2001).	9
Figure 2.3 Schematics of a) DC transferred arc, b) DC non-transferred, c) RF inductively coupled plasma torch configurations (Seo <i>et al.</i> 2012).	15
Figure 2.4 Photograph (left) and schematic drawing (right) of an RF-ICP torch (Boulos 2011).	17
Figure 2.5 Particle heating in the plasma (Boulos 1991).	18
Figure 2.6 Gas phase particle growth of nanoparticles (Zachariah and Carrier 1999). ...	19
Figure 2.7 (a) Conventional helicoidal coil with 2.5 turns, (b) double stage coil, (c) planar coil, (d) elliptical shaped coil (Bernardi <i>et al.</i> (2003).	20
Figure 2.8 Temperature (upper half) and velocity (lower half) distribution at different pressures, (Pristavita <i>et al.</i> 2011).	22
Figure 2.9 (a) Temperature contour lines and (b) mass fraction path lines for three different quenching positions (Mendoza-Gonzales <i>et al.</i> 2006).	24
Figure 2.10 Numerical analysis of the thermal plasma revealing the temperature distribution and particle trajectory with also the change in particle size, (a) 0.33 g/min, (b) 1.7 g/min, (c) 3.5 g/min, (Kobayashi <i>et al.</i> 2008).	25
Figure 3.1 Particle formation in a two component system (Gurav <i>et al.</i> 1993).	34
Figure 3.2 Mg-Ni phase diagram (Okamoto 2007).	38

Figure 3.3 (a) Schematics of the induction plasma torch together with the nanopowder reactor, (b) photograph of the plasma torch and (c) the nanopowder reactor.	41
Figure 3.4 Photograph of the vibrational powder feeder system.	42
Figure 3.5 Photographs of the bottom injection probe. The position of the probe can be adjusted by using inserts in the assembly. Images show the probe at its maximum height (a) and at its minimum height (b).	43
Figure 3.6 Schematic of the induction plasma system.	44
Figure 3.7 Photographs of (a) induction plasma system, (b) detachable and airtight powder collector, (c) powder collection unit and (d) cyclone unit.	45
Figure 3.8 Photograph showing the bottom collector, cyclone collector, large and small capacity powder collector, respectively (from left to right).	46
Figure 3.9 Schematic representation of the purpose-built Sievert's apparatus.	50
Figure 3.10 A photograph showing the general view of the current PCT setup in our laboratory (assembly of thermal insulation is in progress).	51
Figure 3.11 SEM images of (a) initial powders and product collected from (b) bottom collector.	53
Figure 3.12 SEM images of powders collected from cyclone; (a) a large particle decorated by fine particles and (b) a large agglomerate made up of fine particles.	54
Figure 3.13 SEM image of powders collected from the powder collector.	55
Figure 3.14 X-ray diffractograms of the samples obtained from pre-alloyed Mg ₂ Ni precursors using the top injection probe and bottom injection probe.	56
Figure 3.15 X-ray diffractograms of the samples obtained by feeding Ni (1.8 g/min) and Mg (1.2 and 1.6 g/min) separately (Ni - top injector, Mg - bottom injector).	57
Figure 3.16 XRD patterns of samples obtained by feeding Ni via top injector and Mg via bottom injector while the position of the latter (z) changed from 372 to 172 mm.	58
Figure 3.17 Rietveld refinement of the X-ray diffractogram of powder synthesized when z = 272 mm (Rw = 24, sig = 2.24).	60
Figure 3.18 SEM image of powders synthesized using Ni (top injector, z = 0) and Mg (bottom injector, z = 272 mm) precursors.	61

Figure 3.19 High magnification SEM images (a) and (b) of powders synthesized using Ni (top injector, $z = 0$) and Mg (bottom injector, $z = 272$ mm) precursors.	61
Figure 3.20 Temperature programmed sorption curves for Mg_2Ni nanoparticles. The curves refer to initial nominal hydrogen pressure of approximately (a) 9.7 bar, (b) 6 bar, (c) 2.9 bar.....	64
Figure 4.1 Effect of local carbon/metal ratio on the possible formation mechanisms for particles and carbon structures (Elliott <i>et al.</i> 1997).	69
Figure 4.2 Geometrical representation of graphene lattice (upper image) and pore size (lower image), (Berry 2013).	72
Figure 4.3 Carbon encapsulated nickel nanoparticles synthesized using top injector for nickel and bottom injector for methane feeding.	75
Figure 4.4 HR-TEM image of a nickel nanoparticle covered with 7-9 graphitic layers. Graphite shell ($d_{002} = 0.3347$ nm, ICSD #031829) and nickel core ($d_{111} = 0.2041$ nm, NIST #23929). Insets show a close-up image from the core and also its FFT image.	75
Figure 4.5 TEM image of nanoparticles synthesized using Ni and methane precursors.	76
Figure 4.6 TEM image of carbon encapsulated nickel nanoparticles synthesized using top injector for methane and bottom injector for Ni feeding.	77
Figure 4.7 HR-TEM image of a Ni nanoparticle covered with 2-3 graphitic layers, these encapsulating layers have discontinuities as seen in the figure. Insets show a close-up image from the core and also its FFT image.	77
Figure 4.8 XRD patterns of powders synthesized by feeding Mg (0.25 g/min) and methane (1 slpm or 0.1 slpm) using the top injector.	78
Figure 4.9 XRD pattern of powders synthesized by feeding only methane through the top injector.	79
Figure 4.10 HR-TEM image of crystalline carbon structures.	80
Figure 4.11 TEM image of a single Mg nanoparticle encapsulated by several graphitic layers. Insets show a close-up image from the particle and its FFT image.	80
Figure 4.12 HR-TEM image of magnesium nanoparticles. Inset is the FFT image.	81

Figure 4.13 X-ray diffractograms of the powders obtained feeding (a) Mg and methane through top, (b) Mg with top and methane with bottom, (c) Mg with bottom and methane with top injector.	82
Figure 4.14 TEM image of the powders obtained using top injector (Mg) and bottom injector (methane).	83
Figure 4.15 TEM image showing the presence of MgO phase in the products. Inset is the FFT image.	83
Figure 4.16 X-ray diffractogram of sample synthesized by feeding pre-alloyed Mg ₂ Ni with methane.	84
Figure 4.17 HR-TEM image of a carbon encapsulated Ni nanoparticle	85
Figure 4.18 HR-TEM image of carbon encapsulated Ni and MgNi ₃ C.	85

CHAPTER 1

INTRODUCTION

Magnesium and its alloys are among the most promising materials for solid state hydrogen storage since they are lightweight and low cost materials and have high hydrogen capacity. However, obstacles such as high stability of these hydrides and slow reaction kinetics are needed to be overcome for their practical applications. In order to enhance hydrogen storage characteristics, numerous approaches have been reported mainly involving compositional alterations as well as reduction in structural scale. Mg-Ni based materials are promising candidates for this purpose and particularly Mg₂Ni is a well-known composition among this material group that could store 3.6 wt% hydrogen forming its hydride, Mg₂NiH₄. Synthesis of this compound in nano-scale by various methods has been reported and these mainly include methods such as ball milling, melt-spinning and combustion synthesis. While improvements in the hydride stability and reaction kinetics have been attained, hydrogen storage requirements for on-board applications have not yet been fulfilled.

In this study, inductively coupled plasma is proposed as an alternative method for the synthesis of Mg-Ni based materials in nano-scale and particularly Mg₂Ni intermetallic alloy in the form of nano sized powders. In this method, precursors are fed into plasma torch, where the temperature is high enough (up to ~10,000 K) for complete vaporization of powders, which then condenses into nanoparticles further down in the reactor. The method offers one step and continuous synthesis of nanopowders in large scale and allows in-situ mixing of other elements in the high temperature plasma region. As far as we know, at the time of writing, synthesis of Mg-Ni based hydrogen storage alloys with RF induction thermal plasma method has not been reported. In this work, Mg-Ni based nanoparticles have been synthesized in nano-scale by feeding Mg and Ni elemental powders using separate injection probes. Optimum processing parameters for the Mg₂Ni composition formation have been investigated. In the second part of the study, carbon encapsulation feasibility of Mg and Ni powders were also investigated and methane gas was used as the carbon source. Feeding location and feeding rate of precursors were studied for this purpose.

CHAPTER 2

LITERATURE REVIEW

2.1 HYDROGEN STORAGE IN MAGNESIUM BASED METAL HYDRIDES

2.1.1 Introduction

Fossil fuels such as petroleum, coal and natural gas are primary energy sources and more than 85% of world energy consumption is based on these carbon based energy sources (Ghoniem 2011). However, fossil fuel reserves on Earth are limited and it is expected that they will run out since generation of these sources by nature is incomparably slow than their worldwide consumption. Moreover, carbon emission caused by the burning of fossil fuels is believed to be responsible for the global warming and climate change. Therefore, a transition from fossil fuels to clean and renewable energy sources is highly desirable.

Hydrogen is considered to be a key element in this transition. Hydrogen is not an energy source like naturally occurring fossil sources. Rather, it is an energy carrier like electricity. In contrast to electricity, which cannot be stored directly, hydrogen can be stored in a variety of ways after its generation.

A significant portion of the total worldwide energy consumption is used up on transportation. This portion is mainly based on fossil fuels and it correspondingly results in large amounts of carbon emission to the atmosphere. Unlike large-scale applications such as energy generation in power plants where carbon emission could be captured, such measures are not applicable for carbon emission in transportation. For this reason, replacement of conventional fuels used in vehicles with other means of clean energy sources such as hydrogen is extremely important.

Today, hydrogen is mostly produced from hydrocarbons, e.g. via reformation of natural gas, resulting in the carbon emission, i.e. CO₂. So as to reduce emission, in the large scale synthesis of hydrogen, CO₂ may be captured, but since there are limited hydrocarbon resources, this would not be a sustainable approach in the energy production.

Hydrogen could be generated from nuclear energy, but as nuclear energy having its own problems (Ghoniem 2011); the best approach would be to generate hydrogen from renewable sources.

For instance, solar energy available only on the desert regions is about 27,360,000 TWh and collecting 10% of this available energy with 10% efficiency would supply five times the total energy requirement worldwide alone (Abbott 2010). Hydrogen generated from solar energy (or from other renewable energy sources), is a clean and zero emission fuel that could be used for transportation as well as for other mobile and stationary applications. Hydrogen generated in this way can simply be used in internal combustion engines or more efficiently in fuel cells. Unfortunately, the lack of a compact and safe storage method restricts the utilization of hydrogen for such applications (Mandal and Gregory 2010).

There are mainly three methods to store hydrogen; gas, liquid and solid storage. Gas storage is mostly accomplished in high pressure gas cylinders. This type of storage is not suitable for onboard applications due to safety concerns and the need for high volume cylinders. Atomic weight of hydrogen is quite small and correspondingly volumetric density of cylinders is below the desired values. Even some advanced composite cylinders, which can withstand 800 bar pressure, have volumetric density of approximately 36 kg/m^3 . Alternatively, hydrogen can be stored in liquid form. Volumetric density of liquid hydrogen is 70.8 kg/m^3 (Züttel 2004). While it has relatively higher volumetric density, a significant amount of energy is consumed during the liquefaction process. Thermally insulated cryogenic vessels are used to store hydrogen; but still some leakage is allowed for safety reasons resulting in additional decrease in the efficiency.

Pressurized gas and liquid storage of hydrogen seem more suitable for stationary applications. On the other hand, hydrogen storage in a solid medium is considered more advantageous for mobile applications. Solid state storage can be achieved in two different forms; hydrogen-solid bonds may be physical or chemical in nature (Mandal and Gregory 2010).

In physical storage, or physisorption, hydrogen atoms are attached to the high surface area of the host material, such as in carbon nanotubes and metal organic frameworks. Adsorption of hydrogen occurs mainly as a result of the intermolecular forces as van der Waals forces; but such type of storage usually requires very low temperatures. In addition, normally high pressures are required to reach high storage capacity (Suh *et al.* 2011).

In chemical storage, hydrogen atoms are chemically bonded to the host material. Two main materials in this group are complex hydrides and metal hydrides.

Light hydrides of alanes $[\text{AlH}_4]^-$, amides $[\text{NH}_2]^-$ and borohydrides $[\text{BH}_4]^-$ are well known complex hydrides (Orimo *et al.* 2007). Sodium alanate (NaAlH_4) has a storage capacity of 5.6 wt%, first it forms Na_3AlH_6 by releasing 3.7 wt% hydrogen and then forms NaH by releasing 1.85 wt% hydrogen. It is also a low cost material; but, it has reversibility and kinetics problems. Likewise, LiAlH_4 has a capacity of 10.5 wt%, but its stability is quite high. Li_3N shows two different plateaus. It has a similar storage capacity which is 10.4 wt% and 55% of this stored hydrogen can be desorbed at 230°C. Very high storage capacities are also attainable, LiBH_4 capacity reaches 18 wt%; but desorption temperature is again quite high which is above 470°C. Hydrogen capacity of sodium borohydride (NaBH_4) is 10.8 wt%, it is stable up to 400°C and for this reason it is considered not suitable for onboard solid-gas applications (Bogdanovic *et al.* 2000, Sakintuna 2007).

Most interest is focused on the hydrolysis reaction of NaBH_4 with water which occurs according to reaction below (Santos and Sequeira 2011).



Hydrolysis reaction is irreversible; on the other hand it has the advantage of using the hydrogen coming from the water in addition to its own hydrogen content. Excluding the mass of the water, hydrogen storage capacity would correspond to 21 wt% (Santos and Sequeira 2011); but, it is an irreversible process and therefore outside the scope of this thesis.

Ammonia borane (NH_3BH_3) with a storage capacity up to 19.6 wt% is considered as a promising candidate among boron hydrides (Jiang and Xu 2011). It can release its hydrogen content by thermal decomposition or by hydrolysis, or alternatively by dehydrocoupling in non-aqueous solutions. Thermal decomposition occurs in three steps; third step requires very high temperatures and practical solid state storage capacity is considered as 13 wt%. Thermal decomposition process has problems such as slow kinetics, contamination and irreversibility. Alternatively, ammonia borane can liberate hydrogen by hydrolysis when suitable catalysts (e.g. PVP-stabilized cobalt(0) nanoclusters) are added (Metin and Özkır 2009). An ammonia borane hydrolytic dehydrogenation system can store 7.8 wt% hydrogen; but, again this route has problems as slow kinetics, impurity and irreversibility (Jiang and Xu 2011). There are several approaches to regenerate ammonia borane from the spent fuel; but onboard application requirements have not yet been fulfilled (Wang 2012).

Extensive research has been carried out on complex hydrides to decrease stability, improve kinetics and reversibility (Bogdanovic and Schwickardi 1997, Ichikawa *et al.* 2004, Vajo *et al.* 2005). Even some appreciable improvements have been achieved; a storage material with suitable hydrogen capacity and thermodynamics is still missing (Wang *et al.* 2013).

Metal hydrides, which can be regarded as the hydrides of intermetallics, metals and metal alloys, are another group of well-known reversible storage materials. Metal hydrides are generally formed under relatively moderate temperature and pressure; they show good reversibility and also have higher volumetric density compared to both pressurized gas and liquid storage (Sakintuna 2007).

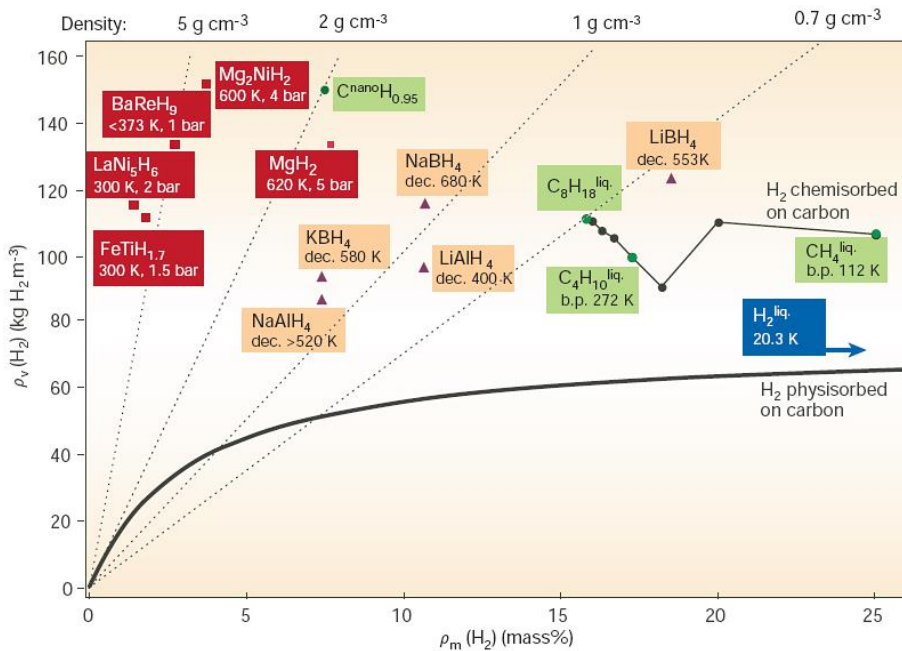


Figure 2.1 Volumetric and gravimetric storage capacities of various hydrogen storage materials and hydrocarbons (Schlapbach and Züttel 2001).

Intermetallic compound of AB₅ type LaNi₅ has been well studied and commercially used as electrode material in metal hydride batteries; but, it is not suitable for onboard applications due to its low gravimetric capacity. As an example, maximum capacity of this AB₅ is about 1.4 wt%. Similarly, intermetallic FeTi has a hydrogen capacity about 1.9 wt% and it requires high temperature and high pressure activation before its reproducible utilization (Sakintuna 2007).

Metal hydrides of Mg and Mg based alloys are quite promising for hydrogen storage purposes. Hydride of pure magnesium, MgH₂ has high hydrogen capacity (7.7 wt%) with good reversibility. It is also abundant in Earth's crust with low cost. A graphical comparison of various hydrogen storage materials (or methods) in terms of their gravimetric and volumetric capacities are shown in Figure 2.1, (Schlapbach and Züttel 2001).

Hydriding reaction of Mg occurs according to the reaction,



However, kinetics of this reaction is fairly slow and high temperatures (300°C - 400°C) are required for the desorption of hydrogen. In order to enhance hydrogen storage characteristics, numerous approaches have been reported mainly involving catalytic oxide additions, compositional alterations (transition metal additions, or alloying) as well as reduction in structural scale including methods as ball milling or thin film deposition.

2.1.2 Compositional Alterations

Compositional alterations made to improve hydrogen storage characteristics of Mg and Mg based hydrides include additions of transition metals as Ni, Cu, Co, Ti, Fe, Pd, Cr, Mn and V (Reilly and Wiswall 1968, Jain *et al.* 2010, Aminorroaya *et al.* 2011, Vyas *et al.* 2012, Liang *et al.* 1999). In addition, oxides such as Fe₃O₄, V₂O₅, Cr₂O₃, TiO₂ and Mn₂O₃ can be used as catalysts to accelerate reaction kinetics (Oelerich *et al.* 2001).

Reilly and Wiswall (1968) synthesized Mg-Ni alloys using induction furnace, they reported the formation of Mg₂Ni and MgNi₂ phases. Mg₂Ni formed Mg₂NiH₄ under 24 bar hydrogen at 350°C, while MgNi₂ did not react with hydrogen. Formation reaction of Mg₂Ni is as follows;



Formation enthalpy of this exothermic reaction is 64.5 kJ/mole, while formation enthalpy of MgH₂ is 75 kJ/mole (Andreassen 2004). On the other hand, storage capacity is 3.6 wt% which is relatively low compared to MgH₂. Despite its low storage capacity, extensive research has been carried on Mg₂Ni compound since it has relatively low reaction enthalpy and shows fast reaction kinetics. Moreover, its stability in air is higher compared to pure Mg that easily forms its oxide.

Synthesis of Mg₂Ni by conventional methods such as arc melting requires several precautions to be taken since the difference between the vapor pressure and melting temperature of Mg and Ni is quite high. Mg loss due vaporization may occur or some portion of the Mg can oxidize at elevated temperatures.

Several production methods reported in literature are mechanical alloying (Liang *et al.* 1998), isothermal casting process (Hsu *et al.* 2007), laser sintering (Si *et al.* 2007), hydriding combustion synthesis (Li *et al.* 2004), induction field activated combustion synthesis (Kodera *et al.* 2007), etc.

Liang *et al.* (1998) have carried out a study on the mechanical alloying of Mg-Ni system. Mg and Ni were added in proportion corresponding to Mg₂Ni stoichiometry and in another batch, excess Mg was added compared to Mg₂Ni stoichiometric proportion. Crystallite sizes were reported as 20 nm for Mg and 10 nm for Mg₂Ni powders. In the first absorption cycle, nanocrystalline Mg₂Ni showed better kinetics compared to Mg+Mg₂Ni powder mixture; but after activation step, the latter showed better hydrogenation kinetics which would be explained by the catalytic effect of Mg₂Ni on Mg and also enhanced diffusion due to presence of interphase boundaries. Desorption enthalpy of Mg₂Ni in the composite material was 69.3 ± 0.2 kJ/mole H₂.

Aminorroaya *et al.* (2011) synthesized Mg-10wt%Ni alloys by casting, the alloys contained up to 1 wt% Nb and casting was followed by ball milling with addition of 5 wt% multi-walled carbon nanotubes (MWCNTs). Samples were further mechanically alloyed with 1.5–3–5 wt% Nb. It was reported that Nb additions improved hydrogenation properties and decreased desorption temperature by 100°C. It was reported that intermetallic Mg₂Ni formed in the sample acted as catalyst by easing the dissociation of hydrogen molecules.

Cermak and Kral (2012) have studied the effect of Si, Ge, Sn and In addition on the Mg/Mg₂Ni alloy. It was reported that the addition of In was more beneficial than the others by increasing the reaction kinetics and decreasing the activation enthalpy of hydrogen desorption.

Ding *et al.* (2012) have studied the effects of B, C and Si additions to Mg₂Ni by performing density functional theory calculations. It was stated that the thermodynamic stabilities of Mg₂Ni and its hydride decreased linearly with the increasing non-metal additions. Dehydrogenation energies were calculated as 58.4, 58.1, 55.8 and 55.3 kJ/mole H₂ for Mg₂NiH₄, Mg₂NiB_{0.5}H₄, Mg₂NiC_{0.5}H₄ and Mg₂NiSi_{0.5}H₄, respectively.

2.1.3 Structural Modifications

It is a well-known fact that decreasing the particle size down to nanoscale dramatically changes the physical and chemical properties of materials. Reduction in structural scale usually has a beneficial effect on hydrogen storage properties. However, it may require several precautions to be taken since structural reduction also increases tendency towards undesirable reactions such as oxidation of the material.

Beneficial effect can be related to the much larger surface area available for hydrogen uptake, shorter distance required for hydrogen diffusion and reduced blocking effect of newly formed hydrides against further hydrogen diffusion. Additionally, defects introduced during the processing of starting materials cause internal strain or distortion in the structure which would again make the diffusion of hydrogen atoms easier.

Wagemans *et al.* (2005) theoretically studied the effect of crystal size on the stability of magnesium hydride. According to authors, decreasing crystallite size to 0.9 nm would significantly decrease the enthalpy to 63 kJ/mole H₂ and desorption temperature to 200°C at 1 bar pressure.

As stated by Bardhan *et al.* (2011), in addition to crystallite size, factors such as surface energy, material interfaces and crystallographic planes may also contribute to the overall storage properties. Steps, kinks, edges, corners and defects that may be generated within nanocrystals would cause a difference between the theoretical and experimental results.

As it is seen in the literature, compositional alterations and structural modifications are usually performed together. Focus in this thesis will mainly be on the studies regarding the Mg-Ni based materials. Among these studies, ball milling has been widely used to achieve these goals (Zaluska *et al.* 1999). Other methods include melt spinning (Zhang *et al.* 2011), acetylene plasma-metal reaction (Zhang *et al.* 2011), mechanically activated self-propagating high temperature synthesis (Atias-Adrian *et al.* 2011), thin film deposition (Akyıldız and Öztürk 2010), melt infiltration (Jongh *et al.* 2007), solution based methods (Jeon *et al.* 2011), etc.

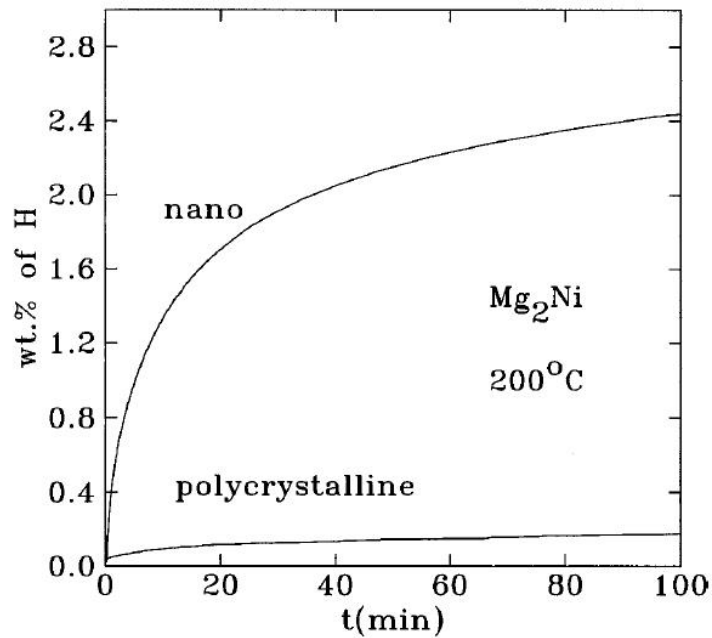


Figure 2.2 Hydrogen absorption behaviors of polycrystalline and nanocrystalline Mg₂Ni at 200°C (Zaluska *et al.* 2001).

Zaluska *et al.* (1998) synthesized nanocrystalline Mg powders by ball milling which improved the morphology and surface activity of powders. Palladium nanopowders were also added as catalyst and resulting powders were reported to show very fast kinetics at lower hydrogenation temperatures without activation. In another study of the same authors, similar effects were observed for other materials such as Mg₂Ni. A comparison of polycrystalline and nanocrystalline Mg₂Ni at 200°C is shown in Figure 2.2 (Zaluska *et al.* 2001).

Orimo and Fujii (1997) have studied the hydrogen storage properties of nano-scaled Mg-Ni alloys. Mg₂Ni powders with and without Ni powders were ball milled under 10 bar hydrogen atmosphere. In Mg₂Ni system, it was found that the most hydrogen was in the inter-grain region leading to 1.6 wt% hydrogen dissolution. Mg₂NiH₄ peaks were not observed in X-ray diffractograms. Dehydrogenating of this hydrogen content was reported to start at 140°C which was quite low compared to the dehydrogenating temperature of Mg₂NiH₄. In another experiment, excess Ni was added (43 and 50 at% instead of 33 at% in Mg₂Ni) and it was seen that the amorphous MgNi phase was also present. Hydrogen content increased to 2.2 wt% and dehydrogenating temperature was lowered down to 100°C in this system.

Bouaricha *et al.* (2000) have investigated the effect of carbon containing compounds on the hydrogen storage properties of nanocrystalline Mg₂Ni powders produced by ball milling. Carbon compounds used in this study were fullerenes (C₆₀), graphite and Vulcan carbon black (XC72) and these additives were mixed in 5 wt% except for C₆₀ which was added 10 wt%. For 5 wt% addition, highest specific surface area was obtained with graphite addition. In this condition, highest storage capacity was also attained, which was 3.45 wt% hydrogen. It was seen that, absorption kinetics did not change with carbon addition; but, desorption kinetics was improved, it was 2-3 times faster compared to the carbon free Mg₂Ni. Interestingly, desorption kinetics was similar for different types of carbon materials, despite differences in the specific surface area values.

Güvendirren *et al.* (2003) have shown that Al₂O₃ and graphite are effective additives that can be used during ball milling of Mg powders. With graphite (5 wt%) addition, 4 wt% hydrogen desorption was achieved in 250 seconds at 350°C.

Bobet *et al.* (2004) have reported the hydrogen storage properties of graphite modified Mg produced by ball milling. Two mixtures were prepared; 90 wt% Mg₂Ni + 10 wt% C and 75 wt% Mg₂Ni + 15 wt% Mg + 10 wt% C. Hydrogenating kinetics were improved by carbon addition. The composite 75 wt% Mg₂Ni + 15 wt% Mg + 10 wt% C was reported to have high hydrogen capacity (5.2 wt% at 573 K) and fast absorption and desorption kinetics. Desorption kinetics was two times faster than the non-graphite modified sample of the same composition. In another study, Janot *et al.* (2004) synthesized Mg₂Ni/C (10 wt% C) by ball milling and also decorated the alloy particles with palladium (5 wt%) using the polyol process. Desorption of 2.7 wt% in 60 minutes was obtained at 150°C.

Vyas *et al.* (2012) have investigated the effect of Cu catalyst on the hydrogenation and dehydrogenation properties of Mg₂Ni. Cu was mixed with Mg₂Ni in different proportions (0, 2, 5, 10 wt%) during ball milling. Storage capacity of Mg₂Ni + 10 wt% Cu was reported to be 1.81 wt% and the formation enthalpy was 53.4 kJ/mole-H₂. MgCu₂ phase which did not absorb hydrogen was also identified in this composition. It was proposed that it catalyzed the hydrogenation process. The same authors (Vyas *et al.* 2012) also studied the effect of Cr, but it was reported that Cu addition was more effective than the Cr addition.

Li *et al.* (2004) have reported the synthesis of Mg₂Ni powders by hydriding combustion synthesis. Hydrogen capacity was 3.25 wt% after the synthesis without any activation treatment. Mean size of particles was 4 μm. The absorption and desorption enthalpies were 57.9 ± 1.6 kJ/mole and 69.2 ± 2.9 kJ/mole, respectively, showing no improvement in thermodynamic properties.

Zhang *et al.* (2011) synthesized Mg₂Ni-type Mg_{2-x}La_xNi (x=0, 0.2) alloys in nanocrystalline and amorphous form by melt spinning technique. It was observed that there was no amorphous phase present without La addition. La promoted the amorphous phase formation and hydrogen absorption kinetics was faster for La-substituted samples.

Shao *et al.* (2004) synthesized Mg₂Ni nanoparticles by using Mg and Ni nanoparticles produced by hydrogen plasma-metal reaction method. Previously prepared nanoparticles compacted and then brought to 350°C. At this temperature, sample was hydrogenated at 40 bar H₂ and later dehydrogenated under vacuum. Product was mainly Mg₂Ni with small amount of MgO. Mean size of Mg₂Ni particles was 30-50 nm. Products did not require activation and showed enhanced absorption kinetics. Hydride released 86.1 wt% of its hydrogen content at 250°C, where the plateau pressure was 0.8 bar. In another study, Zhang *et al.* (2011) have synthesized ultrafine Mg particles having an average size of 40 nm using the acetylene plasma metal reaction technique. Acetylene sent into the plasma decomposed and subsequently formed carbon which confines the Mg growth. Products were reported to have better reaction kinetics compared to bulk Mg and desorption enthalpy was 69 kJ/mole H₂.

Atias-Adrian *et al.* (2011) synthesized nanostructured Mg₂Ni alloy by mechanically activated self-propagating high temperature synthesis (MASHS), which is simply a combination of mechanical alloying and combustion synthesis methods. Size of powders ranged between a few nanometers to 160 nm. Powders were hydrogenated in 15 minutes under 20 bar pressure at 300°C. Desorption temperature observed in DSC curve was around 240°C with a heating rate of 3°C/min.

Vons *et al.* (2011) have studied the synthesis of magnesium nanoparticles generated with the spark discharge technique. Primary particle size of the agglomerated products was about 10 nm and these particles were covered with MgO shells of 1-2 nm in thickness.

Hydrogen desorption temperature extended over a broad temperature range (77°C – 427°C) stated to be the result of oxide layers covering the particles. Pd nanoparticles were added to the products during the in-situ spark discharge generation and this addition was reported to improve sorption kinetics. Average hydrogen storage characteristics of the powders were comparable to ball-milled MgH₂; but desorption started at low temperatures. This was considered to be promising and was taken as a sign that some of the Mg powders had quite favorable properties as a result of their nano size.

There has been also a significant research on the processing of hydride forming materials via thin film deposition. This method is out of the scope of this thesis; but valuable information can be obtained concerning the relation between the hydride stability and the material size. For instance, Akyıldız and Öztürk (2009) have shown that amorphous structure Mg₉₀Cu₁₀ thin film in 300 nm thickness would desorb hydrogen at nearly 100°C. It is obvious that, formation mechanisms of thin films and powders are quite different. Thin films are in contact with substrates and as a result, different defect mechanisms and residual stresses are present. However, it is important to see that particles larger than the theoretically predicted sizes (a few nanometers) would still provide the sufficient decrease in the hydride stability.

It is seen that Mg nanoparticles less than 5 nm in size have been synthesized in recent years by several authors (Jongh *et al.* 2007, Nielsen *et al.* 2009, Li *et al.* 2007, Kalidindi and Jagirdar 2009, Jeon *et al.* 2011). De Jongh *et al.* (2007) synthesized carbon supported Mg nanoparticles by melt infiltration technique. Size of crystallites changed between 2-5 nm to less than 2 nm depending on the pore size of the carbon material used; but hydrogen storage properties of these powders were not reported. Nielsen *et al.* (2009) have reported the synthesis of magnesium hydride nanoparticles embedded in two different carbon aerogel scaffold materials with pore sizes of 22 and 7 nm. Desorption kinetics of hydride phase was reported to be improved with decreasing pore size; however, no improvements in thermodynamic properties were observed.

Li *et al.* (2007) synthesized magnesium nanowires by a vapor-transport approach using commercial magnesium powders. Nanowires were few micrometers in length and had diameters ranging from 30-50 nm to 150-170 nm depending on the argon flow rate. Small diameter samples showed enhanced absorption-desorption kinetics and released 3.28 wt% hydrogen within 30 minutes at 200°C. Desorption enthalpies were 65.3 kJ/mole-H₂ for small diameter (30-50 nm) and 67.2 kJ/mole-H₂ for large diameter (150-170 nm) nanowires.

Kalidindi and Jagirdar (2009) synthesized magnesium hydride nanoparticles having 2-3 nm size using solvated metal atom dispersion (SMAD) method with the addition of hexadecylamine. Nanoparticles started dehydriding at 115°C; but only a small amount of particles dehydrided at this temperature, whereas most of the sample dehydrided at 300°C - 350°C.

Jeon et al. (2011) have reported the synthesis of a new air stable composite material in which Mg nanoparticles of 5 ± 2 nm were embedded in a PMMA polymer matrix. This polymer matrix show selective permeability towards hydrogen while it does not allow oxygen transport. It also has sufficient flexibility to compensate the volume expansion encountered during the hydride formation. Total capacity of 4 wt% hydrogen storage was reported at 200°C for this composite material, improved kinetics (loading less than 30 minutes) was observed; but this has deteriorated after the third cycle. No thermodynamic data was reported for this sample.

In summary, it is seen that a variety of materials such as metal hydrides, complex hydrides, carbonaceous materials have been proposed for hydrogen storage; but none of these materials completely meets the onboard storage requirements. The research on Mg and Mg based metal hydrides has mainly focused on increasing the reaction kinetics and decreasing the hydride stability. Two general approaches aiming to solve these problems are compositional alteration and structural modification. Findings of these studies show that the kinetics problem can be largely solved; but unfortunately the problem of high hydride stability has not yet been solved. However, recent theoretical and experimental studies have reported that the very fine particles (< 10 nm) show promising results, indicating that the new processing approaches could decrease further the hydride stability.

2.2. INDUCTION THERMAL PLASMA SYNTHESIS OF NANOPARTICLES

2.2.1 Introduction

Plasma can be defined as a partially or fully ionized gas form including free electrons, positive ions and negative ions. Due to the presence of these mobile charge carriers, plasmas are considered as electrically conductive and this conductivity depends on the intensity of charge carriers. In practice, plasmas are partially ionized and the proportion of ions to the sum of neutral atoms and ions is termed as the degree of ionization. Ionization process needs a certain amount of energy (i.e. ionization energy) to be transferred to the atoms/molecules and during this process, overall charge remains neutral. The source of energy required to initiate and to sustain the plasma can be nuclear fusion, external heating, presence of electrical and magnetic field, impact of electrons/ions/photons. Most common and widely known examples of the plasma form can be seen in fluorescent lamps, welding arcs, plasma display TVs, the Sun and other stars, etc. In the scope of plasma processing of materials, only artificial plasmas generated and sustained by direct current (DC) or alternating current (AC) electrical and magnetic fields are considered.

Plasma used in materials processing can be classified into thermal and non-thermal plasma. In thermal plasma, temperature of electrons is assumed to be equal to the temperature of heavy particles (ions and neutrals), i.e. plasma is assumed to be in thermal equilibrium. For this reason, this type of plasma is also called equilibrium plasma. Typical examples include DC arcs generated between electrodes, microwave induced plasmas and RF inductively coupled plasmas. Deviations from the thermal equilibrium are likely to occur in practical plasma systems, especially for low temperature plasmas where collision rates are not sufficiently high for the rapid transfer of energy among the plasma (Henne 1999).

Non-thermal plasma, also called non-equilibrium plasma differ from thermal plasma by having lower energy density and higher energy difference between electrons (e) and heavy particles (h) ($T_e \gg T_h$). While thermal plasmas have relatively high electron densities (10^{23} to 10^{28} m^{-3}) and low electron temperatures (1-2 eV), non-thermal plasmas usually have lower electron densities ($< 10^{20}$ m^{-3}) and higher electron temperatures (Boulos 1991). Typical examples of non-thermal plasmas include glow discharge and corona discharge. In non-equilibrium plasmas, presence of electric field accelerates electrons and charged ions, but due to the electron and ion mass difference, electrons accelerate much faster than the heavier ions and reach higher energies. It is known that the collision probability of electrons with heavier ions and neutral particles increases with higher pressure, lower electric field and higher temperature (Eliasson and Kogelschatz 1991). As a result of these facts, non-thermal plasmas are generally characterized as low pressure, low temperature and slightly ionized plasmas. The latter can be related to the decreasing electrical conductivity (accordingly increasing electrical field) of plasma with the decreasing ionization degree. While both thermal and non-thermal plasmas could be called as cold plasmas (relative to fusion plasmas), generally thermal plasmas are referred as hot and non-thermal plasmas as cold plasmas.

Thermal plasmas are used in applications requiring heat and high temperature such as cutting, spraying, welding and ultrafine particle synthesis. On the contrary, processes such as etching and deposition of thin films, in which heat and high temperature are undesired, it is necessary to use non-thermal plasmas (Bogaerts *et al.* 2002).

As mentioned, generation of thermal plasma is required for the plasma synthesis of ultrafine particles, because thermal plasma torches offer a plasma fireball with large heat capacity, in which plasma temperatures range between 3,000 K and 25,000 K. It is possible to reach fast heating rates more than 10^6 K/s (Henne 1999). Widely used thermal plasma generators are mainly DC transferred arc torches, DC non-transferred plasma torches and electrodeless RF inductively coupled plasma torches, as shown in Figure 2.3, (a)-(c), respectively.

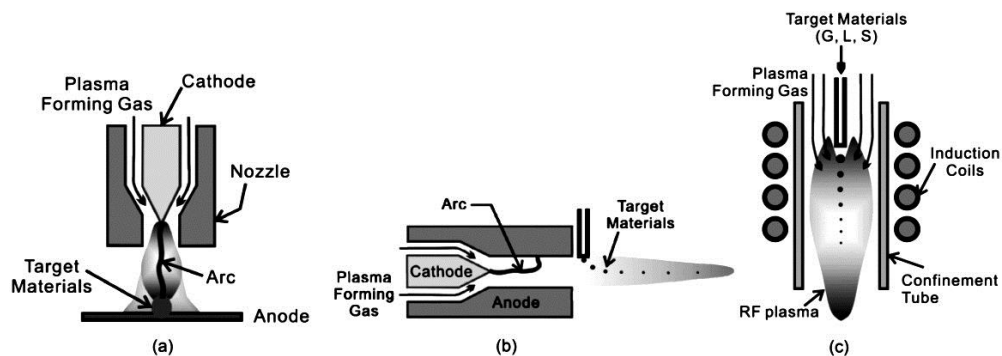


Figure 2.3 Schematics of a) DC transferred arc, b) DC non-transferred, c) RF inductively coupled plasma torch configurations (Seo *et al.* 2012).

These three torches are usually operated at atmospheric pressure. Transferred DC arc plasmas are generally used for such treatments as melting of metals, slag vitrification or the toxic waste destruction applications (Bonizzoni and Vassallo 2002). This type of plasma is also used for the synthesis of nanoparticles having sizes around 50 nm and electrode materials are used also as the precursors (Kogelschatz 2004). In this process, plasma arc evaporates metal electrode and subsequently vapor condenses into fine particles; therefore, it is not a continuous process because anode electrode should be changed periodically. Distance between anode and cathode is relatively large, it may range between a few centimeters to a meter, where the larger distance between electrodes requires higher operating voltage and higher plasma power for the same arc current (Boulos 1991).

In non-transferred DC plasma torches, electrodes are used only to generate plasma flame. Precursors are sent to the plasma flame normally at the exit of the torch and accordingly it is a continuous process. Plasma temperatures may reach up to 20,000 K and torch power of different designs ranges between 20-60 kW (Henne 1999). Plasma hot core volume (area where $T > 10,000$ K) typically has a diameter of 5 mm and length of 20 mm (Boulos 1991). It is mostly used in plasma spraying as well as nanoparticle synthesis and waste treatment, etc. As reported by Young (1985), powder feeding at the exit of the torch results in ineffective powder trajectories and prevents some portion of the precursors' evaporation, though designs are available which allow axial rather than the side feeding of precursors (Ross 1991).

In RF inductively coupled plasma (RF-ICP), torch is electrodeless and it provides continuous production ability forming contamination free plasma. Properties including high enthalpy, high chemical reactivity, large plasma volume, central injection and long residence time of precursors make RF-ICP torches advantageous for the synthesis of sub-micron powders (Cheng 2012, Jiayin *et al.* 2010). In this technique, plasma is basically formed by the coupling of the energy provided by an RF power generator to the

streaming plasma gas via electromagnetic fields. As stated by Faraday's law, a time dependent electrical field E is accompanied by a time dependent magnetic field H ;

$$\nabla \times \mathbf{E} = -\varepsilon_0 \frac{\partial \mathbf{H}}{\partial t} , \quad (2.4)$$

where ε_0 is magnetic permeability of free space ($4\pi \times 10^{-7}$ H/m) and $\nabla \times$ is the curl vector operator. Electromagnetic field in RF-ICP torch is produced by induction coils acting as an antenna. In analogy to the induction heating of metals, in this type of torch, streaming plasma gas can be thought of as an electrically conductive metal piece but with a lower electrical conductivity. In the coupling process, oscillating magnetic field generates eddy currents in the external shell of the plasma volume and accelerated free electrons sustain the plasma. Thickness of this shell can be represented with the following expression with the assumption of cylindrical geometry, uniform temperature and conductivity among the shell volume (Boulos 1985),

$$\delta = \left[\frac{1}{\pi \varepsilon_0 \sigma f} \right]^{\frac{1}{2}} , \quad (2.5)$$

where δ is shell thickness, ε_0 is magnetic permeability, σ is averaged electrical conductivity and f is oscillator frequency. It is important to note that lower frequency results in higher shell thickness according to this expression. Early inductive plasmas had small shell thicknesses causing them to glow brighter peripherally and for this reason they had also been called as ring discharges. Ring effect is observable especially in high pressure plasmas (Hopwood 1992).

Inductive circuit elements may be conductive metals in helical or planar (flat spiral) geometry. In powder processing applications generally helical induction coils are used. Various coil designs have been evaluated by Bernardi *et al.* (2003) and results from this study will be given in next pages.

Plasma torches are constructed from materials which are transparent to RF radiation and which have high melting temperatures. Quartz tubes (as seen in Figure 2.4) or some other ceramic materials may be used for this purpose. An inner tube usually made of quartz is present inside the confinement tube where in between the tubes sheath gas is fed. The main purpose of sheath gas is to protect the body of the torch from excessive heat of the plasma. Design of confinement tube and induction coils influences the coupling efficiency, for instance as the ratio of plasma diameter to coil diameter increases, coupling efficiency increases. This implies that large diameter torches are more efficient in terms of energy coupling. A variety of torches with frequencies ranging between 9.6 kHz to 40 MHz and power ranging between 0.5 kW to 1.0 MW have been designed (Boulos 1985).

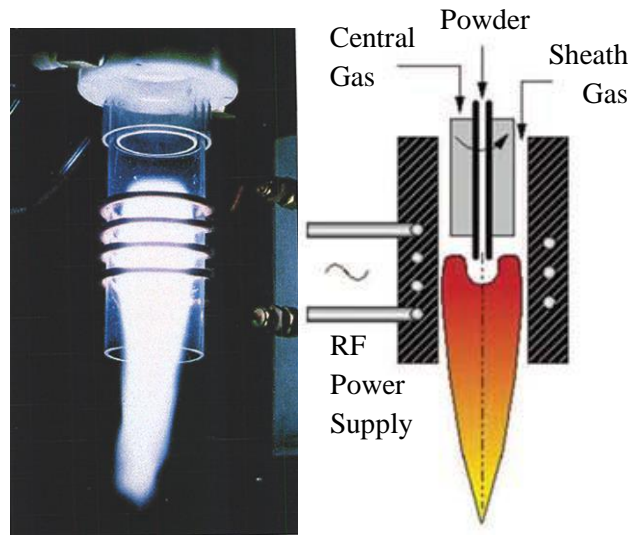


Figure 2.4 Photograph (left) and schematic drawing (right) of an RF-ICP torch (Boulos 2011).

Argon gas is usually used as central plasma gas and it is sent to the torch from the inner tube which is positioned at the first turn of the coil. It has low heat capacity and low thermal conductivity making the starting and sustaining of the plasma easier. Usually only argon gas is used at the starting of the plasma and then air, helium, oxygen or mostly hydrogen is added to the system. As long as sufficient power is supplied and damage to the tube walls due to excessive heat is eliminated, these gases can sustain the plasma (Reed 1960). Plasma is normally started at low pressures, since minimum sustaining power depends on operating pressure (as well as on gas composition). Pressure is increased gradually while the other gases are added progressively. During this, in order to avoid extinction of plasma, gradual increase of power is required. Another phenomenon observed after the ignition of the plasma is E-to-H transition. At the beginning, a low density, capacitively coupled plasma is generated due to direct electrostatic field generated by the coils. As the power is increased, a sharp increase in plasma density is observed indicating the onset of H-discharge, i.e. inductive coupling (Turner and Lieberman 1999).

In addition to the plasma forming gas, powder carrier gas is also added to this gas axially from the center of the inner tube. Precursor injection probes, torch and induction coils are generally water-cooled for the protection against high temperature.

In the applications of RF-ICP torches aiming to synthesize ultrafine particles, precursors are fed into the plasma region through axially located injection probes located at the top of the plasma. According to Ishigaki (2007), for a lab-scale ICP torch with electrical power over 10 kW and a frequency of MHz order, plasma diameter is 30-40 mm, axial

velocity of the plasma is 10-30 m/s and particle exposure time in the high temperature region (also called the dwell time) is 10-20 ms. Initial powders are melted and evaporated in the high temperature region and condense into fine particles at the exit of the plasma. It is possible to control the properties of these condensed particles with a variety of processing parameters such as injection probe location, operating power, pressure, gas flow rate, quenching gas addition, etc. Effects of these processing parameters will be given in the following sections of this chapter.

When the initial powders are fed to the plasma, heat is transferred to the particles through thermal conduction and convection. The difference between this energy and the energy loss due to radiation of the particle gives the total amount of heat absorbed (Boulos 1991). Heating rate of the particles for a given particle size is expected to depend on the plasma temperature distribution and particle flow rate inside the plasma. In very short exposure times (up to a few tens of ms) particles are melted and evaporated depending on the heat transfer capacity of the plasma. As long as sufficient plasma power and exposure time is ensured, complete vaporization of precursors are achievable.

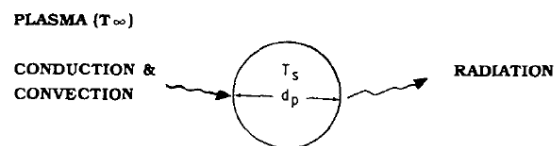


Figure 2.5 Particle heating in the plasma (Boulos 1991).

Evaporated precursors encounter rapid temperature decrease towards the tail of the plasma and it is assumed that gas molecules first nucleate homogeneously, in which rapid cooling is enhancing the homogeneous nucleation. Condensation on existing particles and heterogeneous nucleation on the existing particles follow the homogeneous nucleation. Coagulation in accordance with collisions between particles during their random motion together with the rapid surface growth forms the primary particles which are in near-spherical shapes. Aggregation of primary particles follows this phenomenon and growth continues also with the further agglomeration of existing fractals (Gonzales *et al.* 2008), indeed, when the characteristic coalescence time is greater than the characteristic particle-particle collision time, agglomerates preferentially start to be formed rather than spherical particles as seen in Figure 2.6 (Siegel 1994, Zachariah and Carrier 1999).

Large Brownian motion increases collision frequency resulting in sticking and mutual growth of nanoparticles. If the bonds between particles are weak as in the case of van der Waals bonding, it is called soft-agglomeration. If the particles are sintered to each other,

it is called hard-agglomeration and in this case particles start to behave as micron-sized particles (Leparoux *et al.* 2010, German 2005, Esawi and Borady 2008). It is obvious that the vapor pressure of the precursor material effects the nucleation and particle growth behavior. A particle growth model and an expression for the nucleation rate can be found in the studies of Girshick (1990) and Gonzales *et al.* (2008).

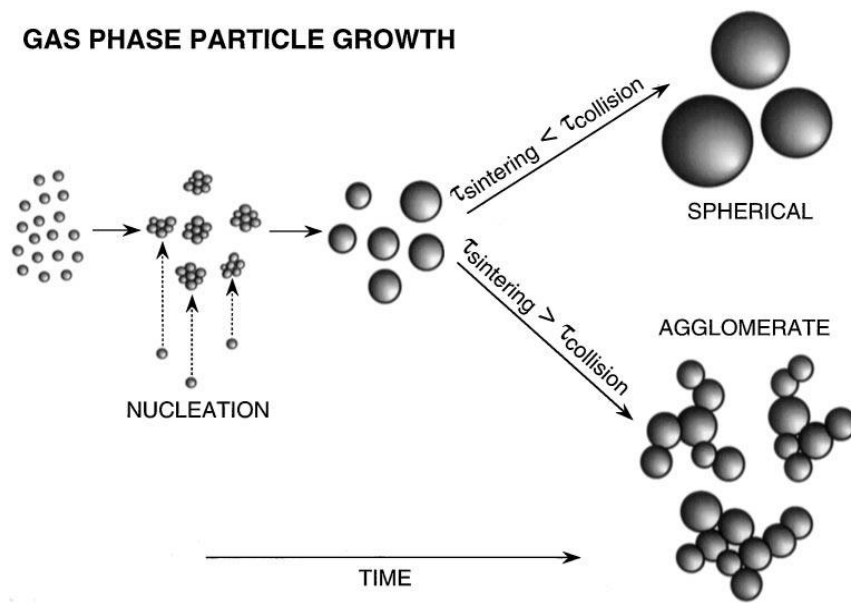


Figure 2.6 Gas phase particle growth of nanoparticles (Zachariah and Carrier 1999).

A wide range of nanopowders have been synthesized by means of RF-ICP torches, these include pure metals, carbides, nitrides, oxides, nanocarbons, etc. A brief summary of the literature on synthesized powders is given at the end of this chapter, but prior to this, effect of process parameters on the plasma and product properties will be given.

In addition to the experimental studies, theoretical studies predicting the plasma behavior under different conditions by means of numerical simulation techniques will also be reported which take into account the thermo fluid dynamics, trajectories of initial powders, thermal history of particles, plasma – particle interaction, vapor diffusion, nucleation and growth of particles (Colombo 2012).

2.2.2 Effect of Operating Conditions on the Plasma and Products

Bernardi *et al.* (2003) investigated effects of coil and torch geometry with a 3-D numerical model for an argon atmospheric pressure RF-ICP torch. In this study; conventional helicoidal, double stage, planar coil geometries and an elliptical cross-section torch were compared.

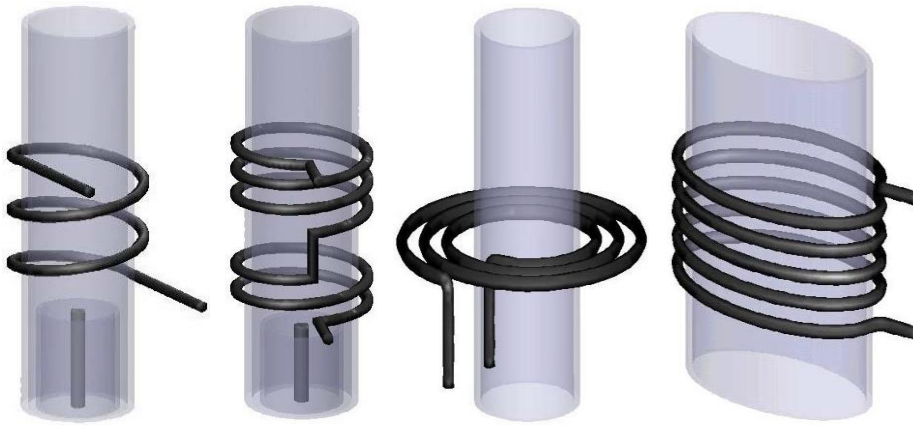


Figure 2.7 (a) Conventional helicoidal coil with 2.5 turns, (b) double stage coil, (c) planar coil, (d) elliptical shaped coil (Bernardi *et al.* (2003).

With the conventional coil, a displacement of plasma towards the confinement tube (towards the front and rear ends of the coil) is reported due to non-symmetry of the induction coils. In the case of double stage geometry, plasma volume extends axially and RF power is dissipated on the upper part of the torch. In planar torch, axial symmetry of power and temperature distribution is observed while elliptical coils show non-symmetry along the minor axis. Conventional helicoidal turns are usually used in powder synthesis applications with several number of coil turns depending on the plasma operating power and powder production capacity. Since the change of induction coils for an existing ICP system is not usually practical, it can be considered as a constant parameter in most cases, after a choice of the proper plasma system was made.

As it can be seen in Equation 2.5, skin depth increases with decreasing working coil frequency. Colombo *et al.* (2010) compared the particle trajectories under two different coil frequencies (3 MHz and 13.56 MHz) for a RF-ICP torch with a non-axisymmetric reaction chamber; and it was shown that for the 3 MHz frequency, larger particles follow a straight line but smaller particles deviate from the axial direction. Frequency is changed during the tuning of RF generator, but usually altered within the allowable limits, so it may not be changed freely when studying with a specific RF-ICP torch.

Soucy *et al.* (2001) have examined the influence of process parameters during the in-flight nitridation of MoSi₂ in an induction plasma reactor. The plasma system under study was RF with a power of 50 kW. The process parameters studied were plasma plate power, chamber pressure, sheath gas composition and quench gas flow rate. The results obtained via an enthalpy probe for a plasma flow without the injection of MoSi₂ powders showed that, maximum temperatures were 7400 K and 6500 K for plate power of 40 and 25 kW respectively, at a chamber pressure of 0.4 bar. Additionally, at high power, the plasma volume was larger. Gas velocity at the lower plate power was 65 m/s. It was stated that an increase in plate power resulted in higher gas velocity in the plasma. Thus at 40 kW, it was 85 m/s. As for the effect of pressure, they found that the plasma temperature was about 1000 K higher in the case of 0.8 bar compared to 0.4 bar pressure (25 kW plate power). The maximum velocity was 47 m/s at 0.8 bar. This should be compared to the velocity of 72 m/s at 0.4 bar. In a similar study, Nishiyama *et al.* (1996) have described the control characteristics of the gas temperature and velocity fields of a RF induction argon plasma. When the power was increased, gas temperature increased slightly in all regions of the plasma, axial velocity in the central region increased and maximum point of the velocity shifted towards the center axis. Similar findings have been reported by Punjabi *et al.* (2012); Ar, N₂ and air were used as plasma gas and it was seen that higher plate power resulted in higher plasma core temperature and expanded plasma volume.

Pristavita *et al.* (2011) have studied carbon nanoparticle production and looked at the effect of pressure in RF plasma. In this work 0.6 – 7 vol% methane gas was added to the plasma (argon) gas. Plasma torch was attached to conical shaped reactor with 50 cm length and 14° angle of expansion. Figure 2.8 was taken from their work and it shows simulation results for temperature and velocity distribution at different pressure levels. As seen in this figure, with increasing pressure (0.2, 0.55 and 1 bar) at 10 kW power, gas velocities decreased and plasma temperatures remained almost unchanged.

In the study of Wang *et al.* (2003), effect of ambient gas and pressure on fullerene synthesis was investigated. Induction plasma torch used had 1.67 MHz oscillator with maximum power of 200 kW, pressure changed between about 0.2, 0.5 and 0.67 bar, under Ar and He/Ar mixed gas. C-Si mixed precursors were fed to the plasma with a rate of 5 g/min and plate power was kept at 30 kW. It was found that addition of helium gas and operation at low pressure were beneficial for the fullerene synthesis. Calculations in this study revealed that, maximum axial velocity had a value of 160, 90, 75 m/s for 0.2, 0.5 and 0.67 bar pressure, respectively. In this study, three different gas compositions were tested; pure Ar, 70%He-30%Ar mixture and pure He. It was observed that the values of highest temperature were almost equal in all gas compositions. The axial temperature decrease, however, was influenced by the gas composition; the highest decrease with a value of 7300 K occurred with pure He. The corresponding values were 5200 K and 1700 K for 70%He-30%Ar and pure Ar, respectively.

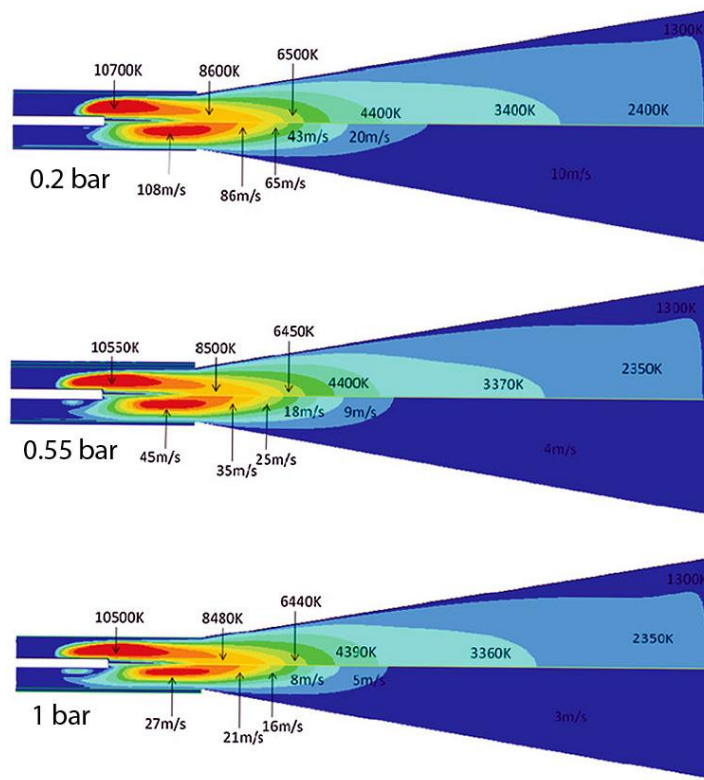


Figure 2.8 Temperature (upper half) and velocity (lower half) distribution at different pressures, (Pristavita *et al.* 2011).

Similarly Kim *et al.* (2010), using 2-D numerical model, have investigated the effect of pressure and gas composition for fullerene synthesis taking into account the plasma - precursor interaction. They similarly found that Ar/He mixture was more efficient than the Ar as plasma gas alone. Elevated gas pressure was found more desirable for obtaining higher fullerene yield; but this is in contrast to the opposite case reported by Wang *et al.* (2003). Similarly, the beneficial effect of high gas pressure was also reported by Cota-Sanchez *et al.* (2005). According to Kim *et al.* (2010), Ar-He plasma cools down easily and the volume of the high temperature zone is smaller compared to Ar plasma since He has higher thermal conductivity. While high temperature volume is smaller, high thermal conductivity and high temperature rise of Ar-He plasma provides higher evaporation efficiency for the precursors. Axial velocity in the hot region of the Ar-He plasma is higher and this reduces the unwanted photochemical destruction of fullerenes synthesized. Higher velocity is the result of higher temperature and lower mass density. The high velocity decreases the residence time of particles inside the plasma; but this does not lead to a decrease in the yield as it is compensated by the higher evaporation efficiency.

Punjabi *et al.* (2012) have conducted a 2-D numerical simulation of an RF-ICP torch (with 3 MHz frequency and 50 kW power capabilities) at atmospheric pressure. Plasma forming gases under consideration were argon, nitrogen, oxygen and air. When the plate power was kept constant at the 15 kW, in the case of argon, maximum core temperature was 10600 K. For the nitrogen, oxygen and air, maximum temperatures were 9100 K, 9000 K and 6600 K, respectively. The largest plasma volume was observed in the case of argon gas, and smallest volume was observed when oxygen was used. Argon was the best choice as it enabled the highest temperature and the largest plasma volume.

Nishiyama *et al.* (1996) have studied on a numerical model focusing on the control characteristics of gas temperature and velocity field by injecting helium gas axially in atmospheric pressure argon plasma. As being one of the process parameter, helium gas was injected as carrier gas or sheath gas together with Ar in a RF torch. When the helium was injected as a carrier gas, central temperature increased which can be explained by active thermal diffusion of He with its higher thermal conductivity. In the case of injection as a sheath gas, temperature decreased considerably even with a low injection rate. High temperature region decreased in size as a result of a decrease in Joule heating accompanied by the lower electrical conductivity.

Mostaghimi *et al.* (1984) have studied various parameters theoretically in a RF inductively coupled plasma. Carrier gas flow rates were 1, 3, 5 and 7 slpm (standard liter per minute) under atmospheric pressure and power level, the frequency were 3 kW and 3 MHz, respectively. As a result of increasing carrier flow rate (while sheath gas flow rate was changed to keep the total gas flow rate constant), area around the centerline close to the injection point cooled down and high temperature region shifted towards the confinement tube wall. In order to see the effect of total gas flow rate, carrier gas flow rate was kept constant while sheath and plasma gas rates were changed giving the total gas flow rates of 20 to 50 slpm at atmospheric pressure (at the power level of 5 kW). Results showed that, area close to the confinement tube was cooler and the point of maximum heat flux moved downstream of the induction coil with increasing gas flow rate.

Ye *et al.* (2007) have synthesized alumina nanoparticles with Ar-O₂ inductively coupled RF plasma (30 kW, 4 MHz). In this study, effect of flow rate and injection position of quenching gas was investigated with regard to synthesized powders. The quench gas was axially added to the reactor at two different radial positions on top of the reactor, with radius of 36 mm and 65 mm, separately or concurrently. It was observed that the increasing flow rate of the inner injection probe from 100 slpm to 500 slpm changed particle sizes from 49.6 to 17.8 nm. It was reported that the effect of the quenching through the inner injection probe was more effective compared to the outer tube. Another finding of this study was the deteriorating effect of very high quenching rates which would result in recirculation flow zones at the upper sections of reactor where particles might be trapped.

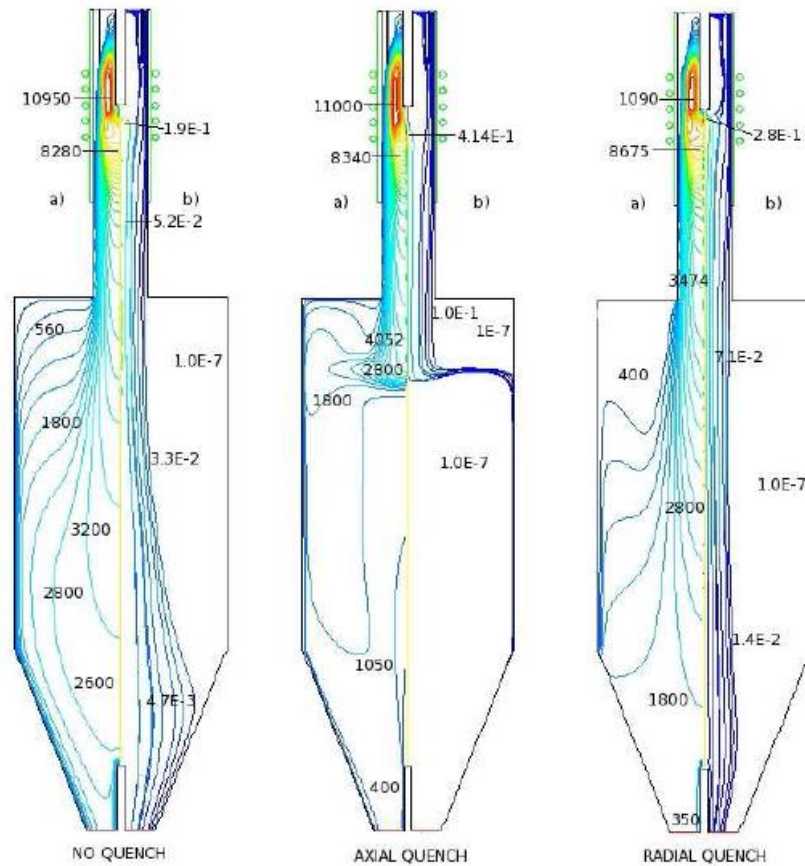


Figure 2.9 (a) Temperature contour lines and (b) mass fraction path lines for three different quenching positions (Mendoza-Gonzales *et al.* 2006).

Mendoza-Gonzales *et al.* (2006) have examined the effect of quenching position and initial precursor feed rate using a 2-D axisymmetric turbulent model of an ICP reactor (40 kW). The induction tube had dimensions of 28 cm (length) and 2.5 cm (radius). Quenching conditions examined included no-quench case, axial injection case in the counter direction flow from the bottom of the reactor and thirdly a radial injection case applied at the entrance of the reactor. Figure 2.9 taken from this study shows temperature distributions and precursor (silica) mass fraction path lines for different quenching conditions. Highest temperature achieved in the plasma was predicted to be 11000 K. While temperature decreased gradually from the central axis to the reactor wall for the no-quench case, an abrupt decline in temperature was observed when the axial counter flow quenching was applied from the bottom of the reactor. In the case of radial quenching, temperature decreased near to the quench zone and mass fraction was concentrated in the axial direction. Largest particles (around 90 nm) were reported for the no-quench case. Particles near to the walls and reactor exit were larger for all three

cases due to recirculation and lower temperatures there. As a second parameter, feeding rate was changed and it was seen that with the increasing amount of precursors fed to the plasma, final particle size increased for all quenching positions. The case of the counter flow cooling was also investigated by Shigeta and Watanabe (2008) using a plasma power of 3 kW. It was found that the counter flow cooling would cause a drastic decrease in temperature of the plasma tail resulting in the promotion of nanoparticle formation. While nanoparticles were formed near to the reactor walls for the cooling without counter flow position, they were produced in the downstream region (below plasma fireball) of counter flow in addition to the region near the reactor wall for the case of counter flow cooling. Additionally, growth mechanisms of materials including B, Cr, Fe, Mo, Pt and Si were also studied in this work and dominant nucleation mechanism was predicted.

Kobayashi *et al.* (2008) have examined copper powder production in a RF induction plasma with a plate power of 40 kW and 2 MHz frequency. Parameters under study were the powder feed rate, reactor pressure and gas flow rate of hydrogen. Both experimental and numerical studies were conducted. They postulated that when the powder feed rate was low, more heat was absorbed by the particle, and as a result, there was an increase in the evaporation ratio; which can be defined as the weight ratio of fine particles to coarse particles assuming that the coarse particles were not condensed from the vapor phase. The effect of powder feed rate is seen in Figure 2.10.

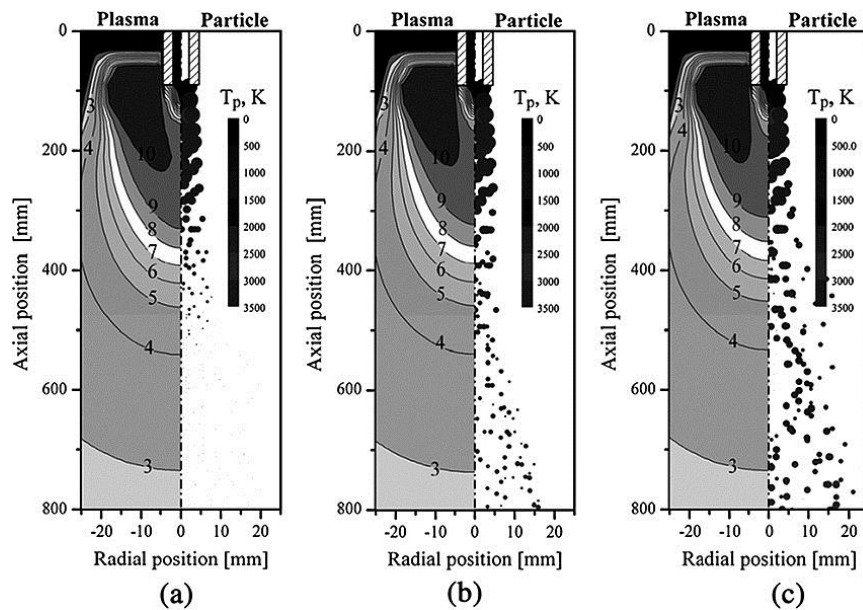


Figure 2.10 Numerical analysis of the thermal plasma revealing the temperature distribution and particle trajectory with also the change in particle size, (a) 0.33 g/min, (b) 1.7 g/min, (c) 3.5 g/min, (Kobayashi *et al.* 2008).

In their study, Kobayashi *et al.* (2008), they further stated that when the powder rate was 0.33 g/min, almost all precursors were evaporated. This was in contrast to a feed rate of 1.7 and 3.5 g/min where there were non-evaporated particles. With the increasing powder feed rate, the amount of total evaporated powder increased but evaporation ratio decreased. Increasing the rate of feeding thus resulted in larger particles (condensed from the gas phase). In order to see the effect of pressure, the reactor pressure was adjusted to 0.39, 0.53 and 0.67 bar and the feeding rate was kept constant at 1.7 g/min. Particle residence time increased when the pressure was raised to a higher value. The amount of evaporation was smallest for the lowest pressure, 0.39 bar. It was also seen that, with the increasing amount of copper vapor, degree of supersaturation was increased resulting in larger particles due to enhanced heterogeneous nucleation. As a third process parameter, flow rate of hydrogen added to the sheath gas was changed and it was reported that the addition of hydrogen increased the evaporation ratio and particle size due to high thermal conductivity of hydrogen.

The study of Shin *et al.* (2006) have experimentally demonstrated the effects of precursor feed rate and central gas flow rate by using suitable plasma diagnostics techniques such as enthalpy probe technique, optical emission spectroscopy and laser light extinction measurements. Alumina powders with a mean diameter of 4.7 μm were fed to a RF-ICP torch (20-35 kW, 13.56 MHz) operating at 0.4 bar pressure (Ar-H₂). Precursor feed rate and central argon gas flow rate changed between 1.4-4.7 g/min and 6-27 slpm, respectively. Decreasing carrier gas flow resulted in an increase in specific enthalpy and higher temperature gradient in the core of the plasma. Also when the carrier gas flow was low the amount of plasma treated precursors and the amount of fine powders that were collected were higher. Optical emission spectroscopy results revealed that with high feeding rate of precursors, Al emission intensity decreased, indicating a tendency from precursor deficient regime to energy deficient regime with increasing feeding rates (Al emission intensity was assumed as a measure of precursor vaporization).

Guo *et al.* (1997) studied on the synthesis of the ultrafine SiC powder by RF plasma (3 MHz frequency, power up to 52.2 kW). Effect of plasma plate power, position of the injection probe and gas composition on the products was investigated. Powders were synthesized through the reaction of silicon and methane, silicon was added axially to the center of coils by using argon as carrier gas. Methane was mixed with the carrier gas. They found that the plasma gas composition influenced the proportions of α - and β -SiC in the resulting products. The ratio (α / β) was less than 1 for the Ar/N₂ mixture while it was larger than 1.5 for the Ar/H₂ plasma gas mixture, also particles were finer for the latter. Injection position was important because it determines the temperature that powders would attain and also particle residence time in the plasma. When the probe tip was located at the distance of 53 mm below the center of discharge, there was 7 wt% free (non-reacted) carbon and when it was located at 21 mm below the center of discharge,

free carbon content was negligible implying longer residence time for silicon was favorable for the reaction of silicon carbide. When probe tip was located at the center of the discharge, reaction was even more favorable but plasma became unstable and extinguished frequently which may be due to the decomposition reaction of methane which absorbs considerable amount of heat.

In summary, it is possible to control plasma properties, correspondingly product characteristics by changing process parameters. Coil and torch geometry mainly determine the plasma shape and temperature distribution in the plasma. Coil frequency affects the skin depth of the plasma and usually high power systems operate at lower frequencies. These parameters are not simply controllable for a given plasma system; consequently these are required to be considered before the establishment stage of a system on the basis of the general requirements for the intended research area. Two important parameters that could easily be controlled are plate power and torch pressure. Plate power mainly affects the plasma volume and temperature, hence the heat capacity of the plasma. Higher operating power results in larger plasma volume and higher temperature. Another effect is seen in the gas velocity where increasing level of power causes to higher axial gas velocity. Although power has an effect on the gas velocity, it is primarily affected by the operating pressure. Increasing pressure significantly decreases the velocity, while the plasma temperature might slightly be increased. Particle residence time is directly dependent on the plasma gas velocity since it determines the exposure time of particles to the plasma. Consequently, it might be said that lower torch pressure results in low residence time and comparatively less efficient evaporation of the precursors. The composition of the gases fed into the torch is another important parameter as a result of their different thermal and electrical properties. Volume of the high temperature zone in the plasma has been reported to be larger for the Ar gas, compared to He, N₂, O₂ and air. Addition of gases having higher thermal conductivity (such as He and H₂) to Ar plasma gas provides more efficient thermal treatment of precursors in the plasma. Addition of He into Ar was reported to increase temperature gradient in the plasma tail. It is also seen that, feeding location of a secondary gas is also important, for instance, addition He as a carrier gas was reported to increase axial temperature of the plasma as a result of its high thermal conductivity. In contrast, addition with the sheath gas was stated to decrease high temperature zone volume of the plasma due to its lower electrical conductivity (skin effect). As it might be expected, quenching gas flow rate is significantly affecting the particle size of the products. Quenching prevents further growth of the particles and with increasing flow rates, finer particles are collected from the system. In terms of quenching gas injection location, it is observed that counter flow quenching results in an abrupt temperature decrease in the plasma tail. Precursor feeding rate and location affects primarily the evaporation ratio. Higher feeding rate increases the amount of vaporized particles but also it results in higher non-evaporated precursor ratio and larger particle size.

2.2.3. Overview of the Powders Synthesized by Induction Thermal Plasma

Induction thermal plasma torches have been used for the synthesis of nanoparticles of a variety of materials. As stated previously, these materials can be listed as mainly pure metals, carbides, nitrides, oxides, nanostructured carbon-based materials and metallic alloys. Synthesis can be achieved via a physical process (evaporation-condensation) or a chemical process (evaporation-reaction-condensation). Metal nanoparticles are mostly generated through physical processing route and examples include Al, Cu, Ag, Ni, Fe, Co, Mo, W, etc. (Jiayin *et al.* 2010).

Bai *et al.* (2009) have reported the synthesis of nickel nanopowders through the hydrogen reduction of nickel hydroxide and nickel carbonate in a radio-frequency plasma. Products consisted spherical nanoparticles with an average diameter of 60 -100 nm. Characterization of nanopowders collected from the filter and large powders collected from the bottom of the reactor indicated that the formation of nickel, as a result of reduction, was achieved in vapor phase rather than in liquid phase. This was concluded because large particles collected at the bottom of the reactor when nickel hydroxide was used as precursor had similar sizes with the starting powders and had smooth, spherical geometry. These powders were melted-solidified particles and x-ray diffraction pattern showed that the main phase was nickel hydroxide indicating no reduction had occurred.

Yoshida and Akashi (1981) produced ultrafine iron particles with a mean size of 10 nm by passing pure iron powders through RF argon plasma. Plate power was 11.2 kW and powder feed rate was 0.04-0.2 g/min. Products had the morphology common to fcc metals while electron diffraction results did not show any traces of fcc γ -phase, meaning that the particles first formed in γ -phase and then transformed into α -phase.

Károly *et al.* (2011) synthesized SiC powders with a RF torch operating at 25 kW plate power and 3-5 MHz frequency. Precursors were commercial silica powder and carbon sources were graphite, char, carbon black and carbonaceous residue of tire pyrolysis. Conversion rate of silica to carbide varied from 60 wt% to 73 wt%, the pyrolytic soot giving the highest yield. Products composed of mainly β crystallites and small amounts of α phase, particle size was around 20-30 nm. Similarly, Ko *et al.* (2012) synthesized SiC nanopowders using organic precursors tetraethylorthosilicate ($C_8H_{20}O_4Si$), hexamethyldisilazane ($C_6H_{19}NSi_2$) and vinyltrimethoxysilane ($C_5H_{12}O_3Si$). RF induction plasma was operated at 18 kW plate power and under approximately atmospheric pressure. Products included SiC, free carbon and amorphous silica with a size range of 30-100 nm. Free carbon and amorphous silica were removed by the subsequent thermal treatment (at 800°C) and HF treatment, respectively.

Baba *et al.* (1989) synthesized ultrafine AlN powders by direct nitridation of Al precursors treated inside the RF plasma operating at 20 kW power and 13.56 MHz frequency. Ar-N₂ mixture was used as the plasma forming gas and pure Al powder together with NH₃ gas were introduced as precursors. High purity AlN particles had an average size around 60 nm.

Li *et al.* (2006) have studied on the synthesis of TiO₂ nanoparticles. Atomized liquid precursors of titanium tetrabutoxide and diethanolamine were fed into the Ar-O₂ induction thermal plasma. TiO₂ nanoparticles with an average size of 20 nm were synthesized through the oxidation of precursors. Effect of the location of quenching gas injection (transverse or counter injection) and gas type (Ar or He) was investigated. It was reported that counter flow injection of quenching gas from the bottom of the reactor using especially He was more effective to obtain finer particles. Wang *et al.* (2006) have demonstrated the synthesis of Fe-doped TiO₂ nanoparticles by oxidative pyrolysis of organometallic precursors dissolved in ethanol. Precursor solution was sent into the thermal plasma operating at 25 kW plate power. Identified phases in the products were anatase and rutile, average particle size was about 40 nm. Anatase was the major phase despite rutile's being thermodynamically more stable, because degree of super cooling for TiO₂ was quite high. Iron concentration changed from 0.05 to 20 atomic percent (Fe/Ti). With the increasing amount of Fe, anatase content decreased and this was attributed to the higher tolerance of rutile for the interstitial iron cations. Zhang *et al.* (2011) synthesized Nb⁵⁺ - Fe³⁺ codoped TiO₂ nanoparticles via RF thermal plasma (2 MHz, 40 kW) by oxidizing liquid precursor mist with various concentrations of Fe³⁺ and Nb⁵⁺. The average crystal sizes of anatase and rutile were 30-40 nm and 56-74 nm, respectively. Powders were characterized for their magnetic properties. Kobayashi *et al.* (2011) have reported the synthesis of Barium strontium titanate ((Ba, Sr)TiO₃) nanosized powders via spray pyrolysis of liquid precursors in an Ar-O₂ RF plasma. Titanium butoxide (Ti(OBu)₄) stabilized with diethanolamine and aqueous solutions of barium nitrate (Ba(NO₃)₂) and strontium nitrate (Sr(NO₃)₂) stabilized with citric acid were mixed and fed into the plasma. Pure and highly crystallized products were 45 nm in size.

Ye *et al.* (2007) synthesized nanosized alumina (Al₂O₃) powders by oxidation of aluminum in an Ar-O₂ RF plasma. Particle size of 16.7 nm was attained with the optimization of quenching gas flow rate and gas injection position. Mohai *et al.* (2007) synthesized zinc ferrite particles in micro and nano scale with radio frequency thermal plasma operating at 15 and 25 kW plate power. Iron and zinc nitrates; Fe(NO₃)₃·9H₂O and Zn(NO₃)₂·6H₂O powders (with a Fe/Zn molar ratio of 2) were dissolved in ethanol and injected into the plasma. Main reaction product was reported as ZnFe₂O₄ with small amount of FeFe₂O₄.

Szépölygi *et al.* (2008) investigated the synthesis of SiO₂ and LaB₆ nanopowders using a RF thermal plasma reactor. In order to synthesize SiO₂, tetraethyl-silicate (TES) liquid precursor was fed to the Ar-O₂ plasma where atomized droplets combusted with the oxygen gas. Plasma torch was operated at nearly atmospheric pressure under 20 kW plate power. In the synthesis of LaB₆, precursor was a mixture of solid La₂O₃ and amorphous B, plasma gas was Ar-H₂ or Ar-He. Particle size of silica was reported as 12-42 nm. It was possible to reduce particle size by lowering precursor feed rate or by increasing the atomization gas flow rate as reported for the synthesis of silica powders. For the synthesis of LaB₆, high yield was obtained at a molar ratio of 20 for B/La₂O₃ in an Ar/He plasma (>30% He) operating at 30 kW power. Mean particle size was 10-50 nm. Both He and H₂ were found beneficial for a higher yield of LaB₆ due to higher thermal conductivity of these gases compared to argon which improve heat transfer between precursors and the plasma.

Lee *et al.* (2012) have reported the RF thermal plasma synthesis of indium zinc tin oxide nanopowders. In₂O₃, SnO₂ and ZnO were used as precursors and mixed at the cation ratios of 6:2:2 and 2:1:1, and subsequently ball milled for 6 hours. This mixture was axially fed to the plasma operating at 26.6 kW plate power. XRD analysis of synthesized powders showed that only IZTO powders with a single phase of In₂O₃ was present for both cation ratios of precursors. Particles were less than 50 nm in size. Substitution of Zn and Sn into In₂O₃ was stated to be possible up to 40-50 at. % and it was further indicated that the quenching with argon (100 slpm) enabled the co-condensation of elements without separate precipitation of Zn and Sn.

Cheng *et al.* (2011) produced titanium boride nanoparticles by RF induction thermal plasma (30.5 kW) under atmospheric pressure. Mixed powders of boron and titanium were fed with a rate of 0.1 – 1.0 g/min and boron content changed between 25 at% and 83.3 at%. Average crystal diameter was between 10 to 30 nm. Boron rich precursor feeding with low feeding rate was reported as the ideal condition for the easy synthesis of TiB₂.

Watanabe *et al.* (2003) have demonstrated the induction plasma synthesis of conductive materials such as borides and mixture of nitrides/borides by correlating the composition of product with thermodynamic considerations including vapor pressure, nucleation temperature and Gibbs free energy. 4 MHz power supply was used and plate power was 20 kW for the argon plasma and 25 kW for the argon-nitrogen plasma. When Ti and B mixture were used as precursor under Ar-N₂ plasma (Ti-B-Ni system), smaller amount of TiN and larger amount of TiB₂ were produced at larger B content of the precursors. It is important to note that the nucleation temperature of Ti is lower than that of B. For Co-B-N system, products were mainly boride which can be attributed to the high Gibbs free energy of nitridation and low Gibbs free energy of boridation. For the Ta-B-N system, products were mainly composed of nitride even the Gibbs free energy of boridation was

low, because Ta has a higher nucleation temperature than boron. Nucleation and solidification of Ta occurs simultaneously in the downstream of plasma and B nucleates around the solidified Ta particle leading only a slight formation of Ta boride particles.

Cota-Sanchez *et al.* (2005) carried out a study focusing on the synthesis of carbon fullerenes using carbon black and nickel precursors. Effect of operating parameters such as reactor pressure, power and precursor feed rate was investigated both theoretically and experimentally. It was shown that increased reactor pressure had a positive effect on the fullerene yield, changing pressure from 0.40 bar to 0.66 bar (40 kW power and 4 g/min carbon feed rate) resulted in an increase in the production rate which was about ~20 wt%. This increase can be explained by the longer residence time of precursors inside the plasma for the high pressure case. Similarly, plate power had a positive effect on the fullerene yield. When the power was increased from 20 kW to 40 kW, yield gain was about ~60 wt%. Higher power inputs increase the temperature of the plasma and enhance the vaporization of carbon and catalyst agglomerates making the fullerene formation favorable. Increasing the powder feed rate resulted in a decrease of the fullerene yield; when the feed rate was increased from 2 g/min to 4 g/min, 33 wt% decrease in the fullerene amount was observed and possible reason of this was explained with the poor vaporization of the injected raw materials in the case of high feeding conditions. When a final production test was conducted with the optimum process parameters that had been determined, the powders collected from the filtration system had a fullerene content of 7.7 wt%.

In another study, Todorovic-Marković *et al.* (2003) have reported the synthesis of fullerenes in RF thermal plasma reactor (3-5 MHz, 27 kW) injecting graphite powders of 1-2 μm in size with a maximum yield of 4.1 % corresponding to a production rate of 6.4 grams/hour.

Kim *et al.* (2007) have demonstrated the synthesis of high quality single wall carbon nanotubes with a RF-ICP torch operating at 60 kW power and 3 MHz frequency. Precursor used was a mixture of carbon black and metallic catalysts. Carbon soot consisted of 40 wt% SWNT and production rate was approximately 100 g/hour. Carbon black precursor with a minimum residue of sulfur was reported to be more favorable for the SWNT production. When He and Ar-He as sheath gas were compared, He gas was found to be more beneficial in terms of the evaporation of precursors inside the plasma as a result of the larger enthalpy content and higher thermal conductivity of the He plasma. In order to see the effect of catalyst content, Y_2O_3 or CeO_2 was added to a mixture of C/Ni/Co as a third catalyst. Ni/Co/ Y_2O_3 catalyst mixture gave the highest product quality.

As seen in the literature, inductively coupled plasma has been used for the synthesis of nanoparticles of pure metals, their oxides, carbides, borides, nitrides together with carbon-based nanostructured materials. When the product consists of more than one element, control of the resulting product composition usually becomes more difficult, especially in the case of metal alloys or nanocomposites. Additional literature regarding the multicomponent systems, mainly focusing on the phase formation mechanisms, will be given in the next chapter (Chapter 3). Also, studies related with the carbon encapsulated metal nanoparticles, particularly synthesized via thermal plasma, will be stated in Chapter 4.

CHAPTER 3

INDUCTION PLASMA SYNTHESIS OF Mg₂Ni

3.1 INTRODUCTION

As reviewed in Chapter 2, thermal plasma is widely used for the synthesis of pure metals, oxides, carbides, nitrides and borides. The synthesis of alloys and intermetallics which involve more than one component has its difficulties. As a result, it would be useful to review the relevant literature before the synthesis of Mg₂Ni intermetallic powders.

A variety of difficulties are encountered during the synthesis of multicomponent materials from the gas phase. Products may have non-uniform composition differing from particle to particle or differing within a single particle. Thermodynamic activities and vapor pressures are usually different for the components. As a result, synthesis of multicomponent materials; especially alloys, intermetallic compounds and composites are quite challenging. Stoichiometry must be precisely controlled and constituents are usually required to be mixed at the atomic scale. Phase segregation or inhomogeneities which may be encountered in a two component system is seen schematically in Figure 3.1. In such a system, nucleation usually starts with one of the component and other component(s) may nucleate on the existing particles, or they may form new particles (Gurav *et al.* 1993).

Vorobev *et al.* (2008) presented a co-condensation model for the synthesis of metal carbide nanoparticles in thermal plasma jet. The model was based on a DC plasma gun operating at 38-40 V, 600 A and under atmospheric pressure (argon). Metals under consideration were Ta, W, Si and Ti. Particle formation scenario was summarized as follows. Element having higher condensation temperature nucleates homogeneously and when stable clusters of this element are formed, remaining atoms together with other component's atoms heterogeneously precipitate on existing clusters. Particles are carried in the gas flow; they collide and coalesce during this movement. Condensation route of TaC and WC systems was different from the SiC and TiC system as a result of the different vapor pressure of components. For Ta and W case, nucleation was predicted to start with the formation of these elements prior to carbon. In the case of Si and Ti,

nucleation started with the formation of carbon nanoparticles directly from gas phase, since carbon does not exist in liquid phase under atmospheric pressure.

Concentration profiles, nucleation rate and particle size inside the reactor were also predicted in this study; but, it was stated that the model would be used for qualitative description of nucleation and growth as a result of the various simplifications made.

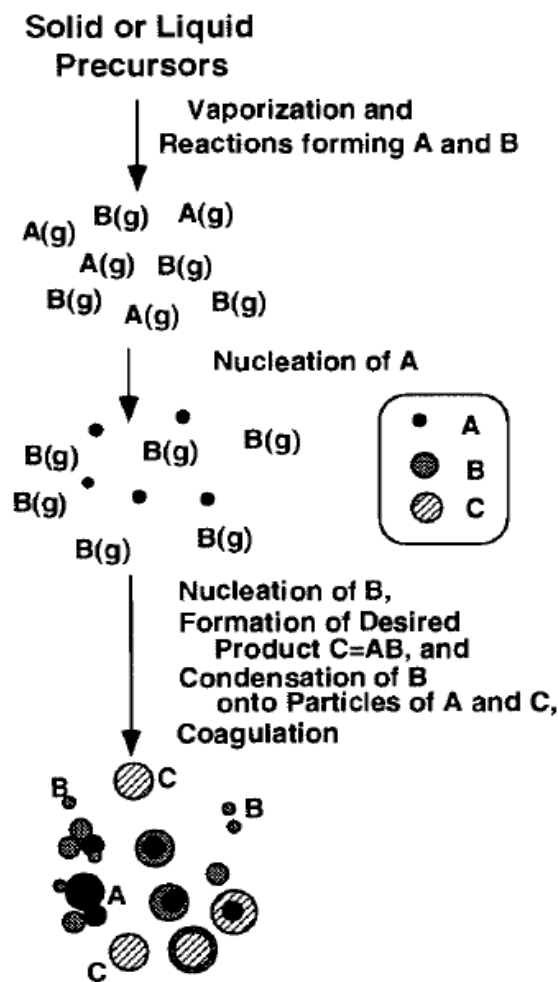


Figure 3.1 Particle formation in a two component system (Gurav *et al.* 1993).

Fan *et al.* (1996) conducted a study focusing on the phase formation in molybdenum disilicide powders during in-flight treatment in Ar-H₂ inductively coupled thermal plasma. In this work, spheroidized powders, melted and solidified without considerable evaporation, were characterized. Metastable β -MoSi₂ (major phase) and stable α -MoSi₂

were observed, products also contained low silicides, Mo_5Si_3 , Mo_3Si and free Si. $\beta\text{-MoSi}_2$ was the major phase, because critical free energy of nucleation for $\beta\text{-MoSi}_2$ is lower than the $\alpha\text{-MoSi}_2$ phase making the metastable β -phase nucleation easier at solidification temperature. Degree of supercooling in the thermal plasma reactor is significantly high and it was stated that as the undercooling degree increases, values of Gibbs free energy of nucleation for both phases approach each other clarifying the presence of these phases together. In this work, effect of reactor pressure, powder feed rate, plasma power and Si content of precursors on the phase formation was investigated. When the reactor pressure was increased, $\beta\text{-MoSi}_2$ amount decreased while Mo_3Si and Si amounts increased. In contrast, $\alpha\text{-MoSi}_2$ content was almost constant (~30 wt%). It was explained with the lowered residence time of precursors inside the plasma in the case of higher pressure, because more Si was evaporated due to its higher vapor pressure. Applying the lever rule on Mo-Si phase diagram, a shift from stoichiometric ratio towards the Mo edge would decrease the MoSi_2 content. As a second parameter, when Si-deficient precursors were sent to the plasma, it was seen that compound Mo_3Si was formed and its content was increased with increasing reactor pressure. Effect of increasing the plasma power was similar to the pressure effects, except that also $\alpha\text{-MoSi}_2$ content increased linearly with increasing level of power; explanation was made regarding the $\beta \rightarrow \alpha$ transformation and enhanced undercooling. Effect of powder feed rate on phase content was mainly due to the unaffected particles inside the plasma due to the overload of starting powders.

Shigeta and Watanabe (2007) have carried out an experimental and numeral study for the Si-based (Mo, Ti) nanoparticle production in an inductively coupled thermal plasma reactor. Numerical study was based on a co-condensation model discretizing the nodal domain of the reactor where nucleation and growth occurred. Experiments and computations were based on RF torch operating at atmospheric pressure (5 kW power and 4 MHz frequency). Initially mixed precursors (in stoichiometric proportion) were sent to the plasma with 0.1-0.3 g/min feeding rate. Precursors' temperature reached their boiling temperature in a very short time, diameters decreased by evaporation keeping the core temperature at boiling temperature. Silicon has the lowest boiling point and first, silicon completed the evaporation, in contrast, molybdenum has the highest boiling point and evaporation was completed at a distance of 47 mm below the injection probe tip which was located at the center of the induction coils. In Mo-Si system, with the temperature decrease, Mo reached its saturation before silicon and it was homogeneously nucleated. Heterogeneous nucleation of Mo followed this and during the growth of Mo nanoparticles, Si reached its saturation point and started to co-condense on Mo nanoparticles. Mo vapor was consumed in 4.9 mm (4.1 ms) and all vapors were consumed in 12.6 mm (12.6 ms). Homogeneous nucleation of Si was not observed. In the Ti-Si system, Si nucleated first, but immediately Si and Ti co-condensed. Silicon content profiles of particles were different depending on the axial position for the Mo-Si case, but they were almost identical in the Ti-Si case due to simultaneous co-

condensation of Mo and Si. It was also seen that higher feed rate of precursors resulted in a larger size; however, the composition of powders was not affected. Precursor composition agreed well with the product composition except for very small particles. Shigeta and Watanabe (2009) modified their study by taking into account compositional variations of the particles which are in the same size range. It was reported that the nanoparticles in the size range of 10-30 nm had the largest population of MoSi₂ and TiSi₂. In their following study, Shigeta and Watanabe (2010) made another modification and they used theories for binary homogeneous and heterogeneous nucleation rather than the theory of unary systems. It was shown that Mo-rich nuclei were formed at the early stage of the growth and then nanoparticles were formed by co-condensation and coagulation among themselves. After 5.91 ms, 97% of Mo and 20% of Si vapor were consumed. During the growth, binary nucleation occurred as well, resulting in extra particles less than 1 nm in size with Si content of 15-75 at%. All vapors of Mo and Si were almost consumed in 24.74 ms in this model. Their earlier work proposed that Mo nuclei was formed first and Si was condensed on Mo nanoparticles which would possibly result in Mo/Si core-shell structure; but, it was shown in this model that nanoparticles were intermetallic compounds (with the consideration of binary nucleation and condensation).

Suresh *et al.* (2008) synthesized intermetallic iron aluminide nanoparticles by using non-transferred DC thermal plasma torch operating at atmospheric pressure. Power level of 9.8 kW and 15.3 kW were applied and initially mixed precursors (85 wt% Fe and 15 wt% Al) were ball milled before being fed into the plasma (14 g/min feeding rate). Liquid iron and aluminum droplets reacted exothermically and they were quenched in atmospheric air. XRD results showed that the products included Fe₃Al and FeAl intermetallic compounds together with Fe₃O₄ and Al₂O₃. Patterns were identical for both power levels. It was observed that more than 60% of the powders were between 30-70 nm in size.

Son and Taheri (2002) synthesized ferrite and nickel ferrite nanoparticles using a RF-ICP torch (50 kW maximum power, 3 MHz). Argon gas was used as the plasma forming gas and air was introduced as an oxygen source to the plasma after the plasma ignition. Precursors were Ni + Fe (Ni: Fe = 1:2) mixture, NiFe permalloy + Fe (Ni: Fe = 1:2) mixture and NiFe permalloy (Ni:Fe = 1:1), respectively. It was observed that most of the starting powders were converted to ferrites (Fe₃O₄ and NiFe₂O₄); also some small peaks were attributed to the unreacted precursors. ICP analysis indicated that Ni + Fe mixture did not result in alloying of Ni and Fe, powders collected from the filter were mainly magnetite and nickel content was nearly 4 at%. In the case of NiFe and Fe mixture, Ni content increased to nearly 14 at%. When NiFe was used as precursor, Ni content was between 40-48 at% demonstrating the viability of Ni ferrite synthesis using NiFe permalloy. In their following work, Son *et al.* (2003) investigated the structure and magnetic properties of Mn and Mn-Zn ferrite nanoparticles synthesized by a RF torch.

Two different samples were used as feeding materials after being ball milled; Mn + Fe mixture (atomic ratio of 1:1) and Mn + Zn + Fe (atomic ratios of 1:1:4). Most of the precursors were transferred into ferrites, MnZn ferrites were close to the $Mn_{0.5}Zn_{0.5}Fe_2O_4$ stoichiometry while Mn ferrites were off stoichiometry regarding the $MnFe_2O_4$.

Scott *et al.* (1997) synthesized Fe-Co alloy nanoparticles using a RF plasma torch. Pre-alloyed FeCo powders and a mixture of Fe and Co powders were used as precursors. Additionally, acetylene gas was injected into the plasma in order to form a protective carbon coating on the particles. Both experiments produced alloy particles, but it was observed that the products had smaller variations in Fe/Co ratio when pre-alloyed powders were used. In a similar study of the same authors, Turgut *et al.* (1998) investigated the magnetic properties and ordering in C-coated Fe_xCo_{1-x} ($x = 0.5, 0.45, 0.4, 0.35, 0.3, 0.25$) alloy nanoparticles. Plasma was formed with a RF torch (50 kW – 3 MHz) and acetylene was used as carrier gas. Fe-Co mixture was used as precursor; products did not include carbides, oxides or hcp ϵ -Co phase. Only α -Fe, f.c.c. Co and graphitic carbon were observed.

Çakmak *et al.* (2010) have reported the synthesis of Mg-Ti nanopowders with a RF plasma torch of 25-27 kW applied power. Size of the magnesium powders were less than 100 nm and titanium powders occurred as separate particles mixed with magnesium particles. Additional MgO (up to 33 vol%) phase was present since the powders were air exposed before the structural characterization.

Table 3.1 Phases observed in products when five different mixtures were used as precursors (Umemoto and Udaka 1998).

Premixed powders	Nitride	Solid Solution and intermetallic compounds
Al - Cu	AlN	Al, Cu(Al), Al_2 (Cu), AlCu, Al_4Cu_9
Al - Ni	AlN	Al, Ni(Al), Al_3Ni_2 , AlNi, $AlNi_3$
Ni - Ti	TiN	Ni
Al - Ti	AlN, TiN	AlTi
Si - Ti	TiN	Si

Umemoto and Udaka (1998) investigated the formation of binary alloys using plasma jet method by using starting powder mixtures of Al-Fe, Al-Si, Fe-Si, Al-Cu, Al-Ni, Ni-Ti, Fe-Cu and Fe-Ti. Chamber pressure was 0.75 bar, Ar- N_2 and Ar- N_2 - H_2 was used in the plasma generation (12 kW). Phases observed in the products include nitrides, solid solutions and intermetallics as can be seen in Table 3.1. For Al-Cu system, an increase in the Al content of the precursor, or a decrease in the argon flow resulted in higher content of intermetallic compounds. On the other hand, addition of hydrogen into the gas flow inhibited the nitride formation. The latter was also observed for the Al-Fe system. In the

case of Al-Fe, aluminum content in the product was less than the source material and changing argon flow from 7 slpm to 3 slpm considerably lowered this composition deviation.

As seen in the literature review given above, the synthesis of nanopowders involving more than one element is not as easy as pure metals, oxides, carbides, etc. As will be reported below, the current work involves the use of a reactor which involves two injection probes. This would provide additional flexibility in the synthesis process where the possibility of obtaining multicomponent nanopowders might be improved.

This chapter aims for the synthesis of Mg-Ni based nanopowders, particularly of Mg₂Ni for the hydrogen storage purposes. The phase diagram of Mg-Ni is given in Figure 3.2. As seen in this diagram, there are two intermetallic compounds in this system; Mg₂Ni and MgNi₂. It should be mentioned that the latter does not form its hydride and its presence lowers the overall hydrogen storage capacity of the product.

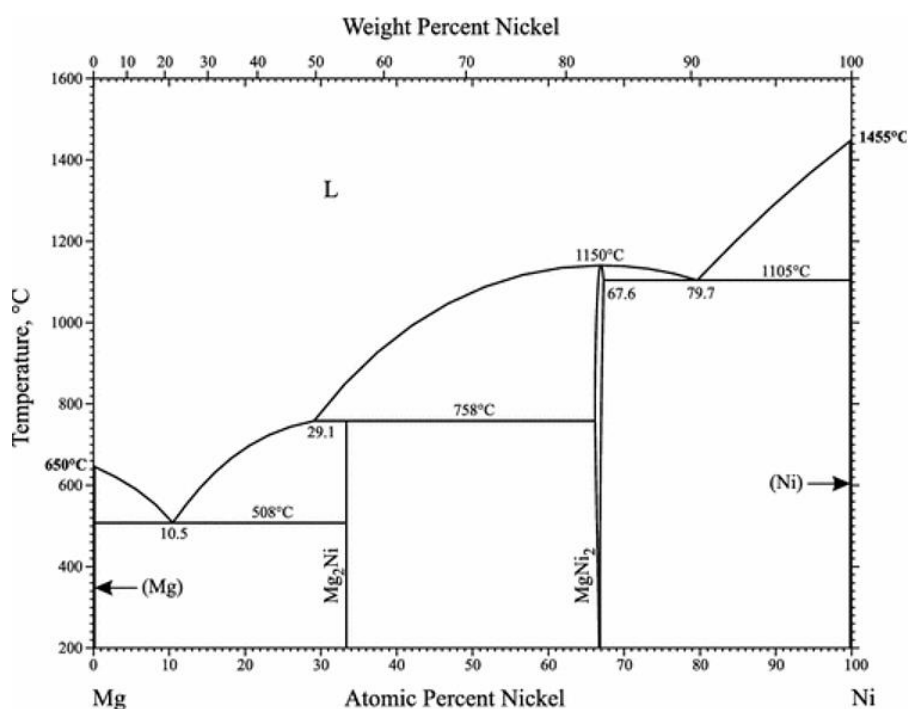


Figure 3.2 Mg-Ni phase diagram (Okamoto 2007).

As reported above, small difference in nucleation temperature of the elemental constituents favors the co-condensation and homogeneous mixing of these species. It should be mentioned that in Mg-Ni system, the difference between the vapor pressures,

melting and evaporation temperatures of Mg and Ni is not small. However, this problem may be overcome by feeding the elemental powders in different temperature zones and also in some extent with the high degree of undercooling in the plasma reactor that would retard the separate nucleation of elemental powders.

In this chapter, Mg-Ni nanoparticles were synthesized in different feeding geometries. First Ni was synthesized by feeding Ni precursor. This was followed by attempts to synthesize Mg₂Ni nanoparticles. In first approach, Mg₂Ni pre-alloyed powders were used as precursor. This was followed by co-feeding of Ni and Mg powders in top and bottom injection probes. A series of experiments were conducted where the position of bottom injector was changed.

3.2 EXPERIMENTAL

3.2.1 Materials

Pure magnesium powder (99.8 % pure, -300 mesh) from Alfa Aesar and pure nickel powder (99.9 % pure, -325 mesh) from Höganäs were used in the experiments. Pre-alloyed (Mg₂Ni) powder was synthesized from magnesium and nickel powders via melting. For this purpose powders were mixed in the stoichiometric proportion and milled with SPEX 8000M for 5 minutes. Resulting mixture was then compacted into discs and then melted under 10 bar argon atmosphere using the Linn HighTherm vacuum/pressure induction melting unit. The resulting product was checked with X-ray diffraction verifying complete Mg₂Ni formation. The product was ground and sieved to -300 mesh.

3.2.2 Induction Plasma System with Nanopowder Reactor

The apparatus used for the nanoparticle synthesis is a 30 kW thermal induction plasma system (Tekna Plasma Systems Inc.). The system consists of a high RF power terminal with a nominal frequency of 2-5 MHz and the inlet power of 50 kVA. The terminal is connected to Tekna PL-35 induction plasma torch in which the electrical energy is largely coupled into thermal energy. Torch is continuously cooled with a closed-circuit DI-water cooling system which is connected to a heat exchanger.

A simple sketch of the plasma torch together with the nanopowder reactor is seen in Figure 3.3(a). As seen in the figure, plasma torch is attached to the top of the reactor and it is enclosed by a Faraday cage. Electrical, cooling water, injector and gas connections

inside the Faraday cage can be seen in Figure 3.3(b). During experiments, induction plasma torch was operated at a constant plate power of approximately 25 kW.

As also seen in Figure 3.3(a), the torch incorporates two probes for feeding the precursor materials. The figure shows the feeding location of both injection probes; bottom injector can be detached from the reactor in which case a bottom powder collector can be connected to the reactor. The addition of this collector is useful for collecting larger particles coming out from the torch.

Central gas (plasma forming gas) used in the experiments was pure argon (Linde, 99.995% purity); it was sent into the torch through the inner quartz tube with a flow rate of 15 slpm. Sheath gas was fed through the annular interspace between the inner tube and the outer confinement tube. Sheath gas was a mixture of pure argon (Linde, 99.995% purity) and pure hydrogen (Linde, 99.995% purity).

Argon flow was provided at 60 slpm before the ignition of the plasma. Following the ignition, hydrogen flow was increased gradually to 6 slpm. This was necessary, since sudden increase of hydrogen content would extinguish the plasma, particularly at the low plasma power. Hydrogen is added mainly to ensure a more efficient protection of confinement tube against the excessive heat and to provide a more effective thermal interaction.

As it is well known, ignition of the plasma is much easier under low torch pressure. For this reason, the starting pressure was kept at approximately 0.28 bar in all experiments. After the ignition of the plasma, the pressure, power and hydrogen flow were increased alternately. The pressure was increased with increments of 0.25 bar. The power was increased slowly again to the set power (25 kW). The hydrogen flow was already increased to the set value (6 slpm) before the power reached 20 kW. Final torch pressure in all experiments was about 0.97 bar. This value is slightly less than the atmospheric pressure.

The reactor also incorporates inlets for the admission of quenching gas, as shown in Figure 3.3(a). For this purpose, nitrogen gas was used with flow rate of 150 slpm. This gas was injected into the reactor radially at an angle. The feeding position of the quenching gas is also seen in Figure 3.3(a).

Precursors were fed into the plasma using either the top or the bottom injection probe, or both of them. Carrier gas was Ar (Linde, 99.995% purity) and flow rate was always kept at 5 slpm. Feeding of metallic precursors was performed using vibrational powder feeder system, as shown in Figure 3.4. Feeding rate is mainly determined by the frequency and amplitude (stroke) of vibration applied to the feeder.

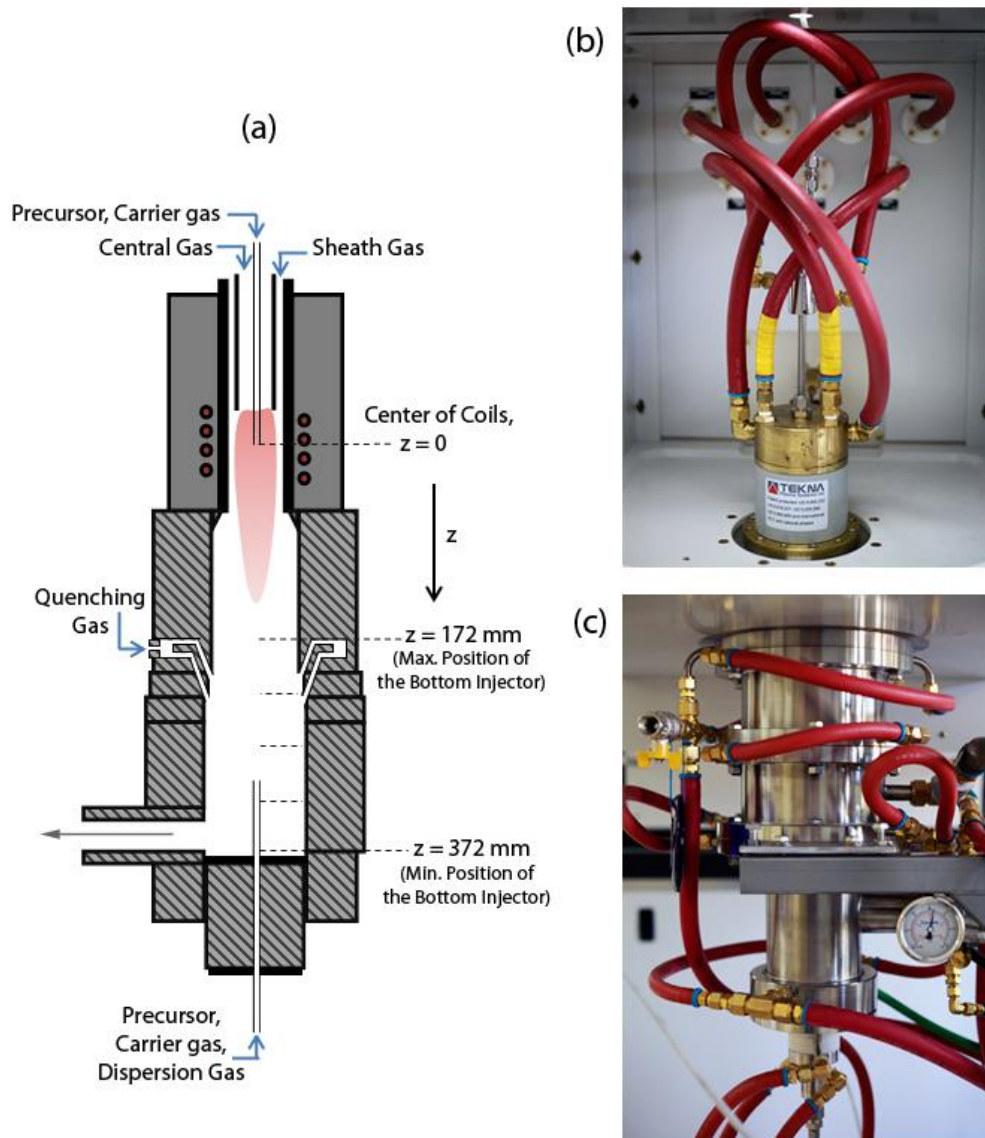


Figure 3.3 (a) Schematics of the induction plasma torch together with the nanopowder reactor, (b) photograph of the plasma torch and (c) the nanopowder reactor.

The feeder was calibrated by measuring the amount of powder it feeds at a prescribed period of time before it was used for the actual synthesis. Frequency and stroke were changed until the desired feeding rate was achieved. Carrier gas was argon maintained at 5 slpm.



Figure 3.4 Photograph of the vibrational powder feeder system.

Since the bottom injector (Figure 3.5) is exposed to higher temperature, in addition to carrier gas, a separate dispersion gas was fed to the injector. This gas was argon which was maintained at 5 slpm in all experiments. The dispersion gas protects the probe tip from excessive heat. Both the top and bottom injectors were cooled with DI-water circulation.

A schematic drawing of the complete plasma system is shown in Figure 3.6. The plasma torch is located at the top of the reactor. So, plasma is generated at the top of the reactor. Precursors sent through the injection probes reach and penetrate into this plasma where the temperature could be as high as $T > 10,000^{\circ}\text{C}$. The precursors are then vaporized and subsequently condensed in the cooler sections of the reactor.

Following the plasma torch, nanopowder reactor comprises three stations for the powder collection which are bottom collector, cyclone collector and powder collector (Figure 3.6). Aerosol flow (particle and gas flow) is forced to make 90° turn at the bottom of the plasma reactor. Only sufficiently small particles are able to follow this aerosol flow.

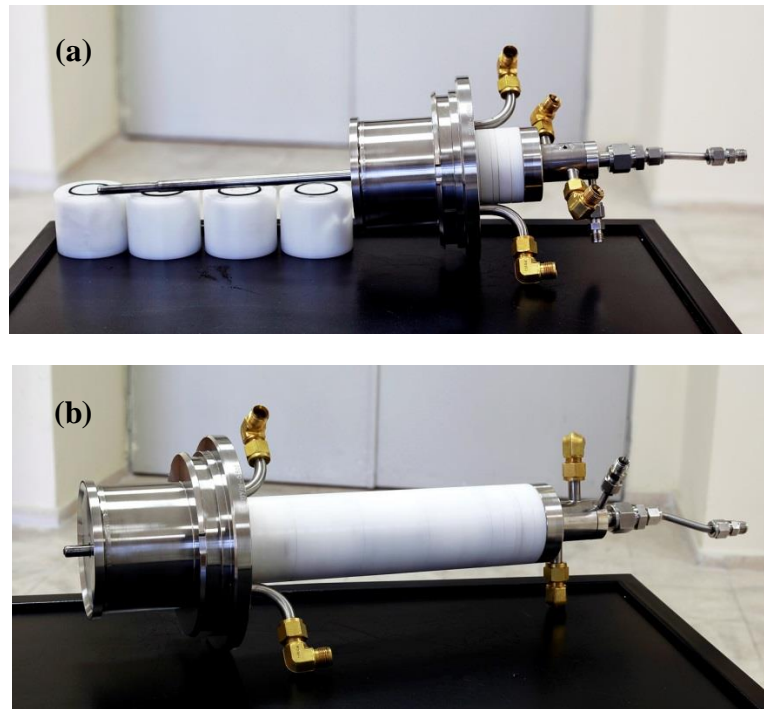


Figure 3.5 Photographs of the bottom injection probe. The position of the probe can be adjusted by using inserts in the assembly. Images show the probe at its maximum height (a) and at its minimum height (b).

The rest, i.e. large particles fall into the bottom collector (this is true when bottom injection probe is not connected to the system since bottom injection probe replaces the bottom collector). These are mainly spheroidized particles which are melted in the plasma rather than being evaporated.

After leaving the plasma reactor, finer particles reach to the cyclone unit and this time aerosol flow is forced to make 180° turn at the bottom of the unit. Here, intermediate size particles ($> 1\text{-}2\ \mu\text{m}$) are separated from the aerosol and collected at the bottom where cyclone collector is placed. Submicron particles usually follow the gas flow and reach to the powder collection unit.

Powder collection unit is shown in Figure 3.7(c). It is made up of a conical portion which houses candles fabricated from porous stainless steel filters. Some proportion of small particles fall into the powder collector, while others deposit on the stainless steel porous filters.

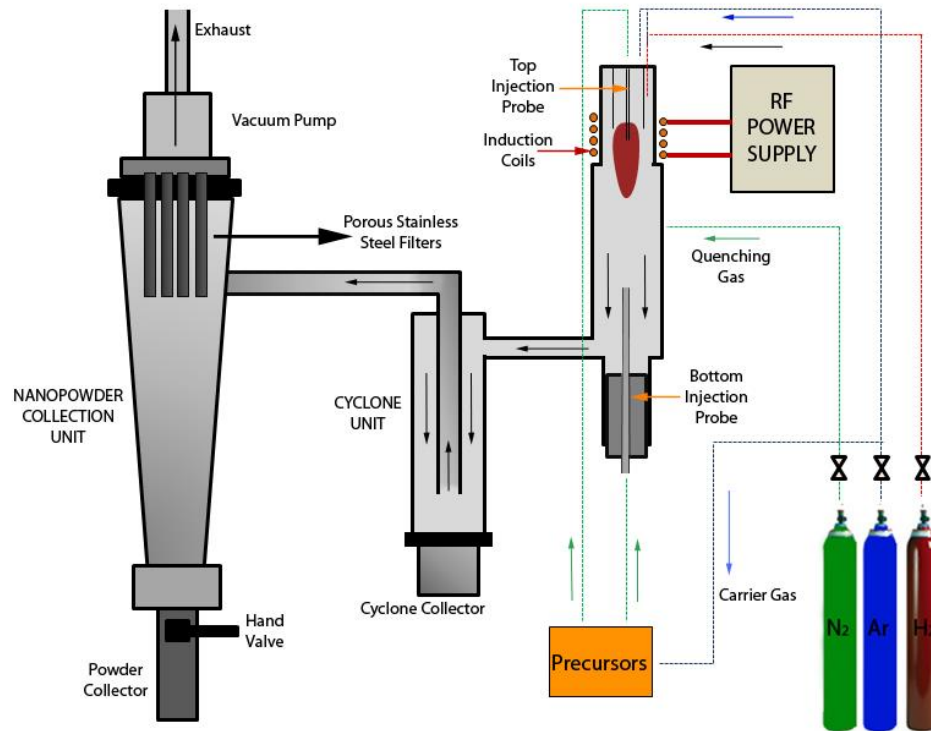


Figure 3.6 Schematic of the induction plasma system.

Powders that are deposited on the candles are blown back at adjustable intervals by applying a pulse of positive pressure and then deposited powders fall into the canister, i.e. powder collector. It is shown in Figure 3.7(b). Gas leaving the bottom collector is fed to a vacuum pump which controls the operating pressure of the whole system and this gas is transported then to the exhaust.

Powders collected in the reactor can be removed when needed. The bottom collector can be removed by hand. Cyclone collector, as seen in Figure 3.7(d), can be detached from the cyclone unit by deactivating the pressure-locked o-ring connection system. Since these are micron sized powders, air exposure does not give rise to significant oxidation. Particles collected from the powder collector are, however, quite reactive in air. Thus, air exposure should be prevented for both the safety reasons and for the intended application, i.e. hydrogen storage. For this aim, after each experiment, air-tight valve of the powder canister was closed and the canister was moved to the glovebox.



Figure 3.7 Photographs of (a) induction plasma system, (b) detachable and airtight powder collector, (c) powder collection unit and (d) cyclone unit.

The canister incorporates a purging inlet with a quick connect. Before the canister is transferred to the glove-box, this inlet was used for 3 argon-vacuum cycles so as to remove the atmosphere existing in the canister. Canister and the purging inlet can be seen in Figure 3.7(b). Currently, a small canister is used for easier handling; but a larger canister is also available for the large-scale synthesis of nanoparticles (Figure 3.8).



Figure 3.8 Photograph showing the bottom collector, cyclone collector, large and small capacity powder collector, respectively (from left to right).

In current study, initial experiments were carried out with Ni. For this purpose, induction plasma system was operated at approximately 25 kW. Ni powders were fed using the top probe at a feed rate of 3 g/min. The system was operated for approximately 15 minutes. Powders were collected from the bottom collector, cyclone and powder collector.

So as to obtain Mg_2Ni nanoparticles, two sets of experiments were carried out. First, pre-alloyed Mg_2Ni powders were injected using either the top injector, or the bottom injector. Bottom injector tip was positioned at its minimum height, $z = 372$ mm. With the bottom injector, in addition to carrier gas, dispersion gas was introduced at the injector tip with 5 slpm flow rate.

The second set of experiments involved the use of elemental powders; Mg and Ni. Pure Ni powders were fed (1.8 g/min) through the top injector while pure Mg powders were fed via the bottom injector (1.2 g/min or 1.6 g/min). Also, position of the top injector was kept constant (at $z = 0$), while the position of the bottom injector was changed.

Accordingly, magnesium powders were fed (1.2 g/min) at five different locations; $z = 372, 322, 272, 222, 172$ mm, respectively. The carrier and dispersion gas flow rates were the same as in the previous set of experiments.

3.2.3 Materials Characterization

Powders synthesized by the thermal plasma system were characterized by X-ray diffraction, SEM and BET analysis. The instrument used in the XRD analysis was Rigaku DMAX 2200 (Cu- K_{α}). Most samples examined with X-ray were air passivated and therefore no special precautions were taken during handling and measurements. However, where necessary, the samples were also examined using an air-tight sample holder that is transparent to X-rays. The diffraction patterns obtained with XRD were refined by Rietveld method when required (Rietveld 1969) using Maud Software (Lutterotti 2011).

Powder morphology was observed via FEI Nova Nano 430 scanning electron microscope which is equipped with a field emission gun. Double sided conductive carbon tape was used for the attachment of samples to aluminum stub holders. Particle size was also analyzed using SEM images, via ImageJ software. EDX analysis was performed on particles so as to determine their chemical make-up.

Specific surface area of the nanopowders was obtained by using Quantachrome Corporation Autosorb-6 BET analysis instrument. Average particle diameter was derived from this value by Equation 3.1 (assuming all the particles are spherical in shape),

$$d_{BET} = 6/(S_{BET} \cdot d) , \quad (3.1)$$

where d_{BET} is the average diameter of the particles, S_{BET} is the specific surface area value obtained from the analysis and d is the density of the material.

3.2.4 Determination of the Hydrogen Storage Properties

Hydrogen storage characteristics of the powders were determined by a purpose-built Sievert's PCT apparatus. It is an automated instrument that is capable of making measurements for the pressure-composition-temperature (PCT) isotherms as well as absorption/desorption kinetics, temperature programmed absorption/desorption and absorption/desorption cycles.

The instrument is based on the Sievert's method which measures the amount of hydrogen gas absorbed or desorbed by recording the pressure change of a closed system of known volume and temperature. In a typical PCT test, the total system volume is divided into

two different volumes that are “sample system volume” and “measuring system volume”. Two systems are connected to each other through a valve and a pressure gauge is attached to the measuring system.

Measurements are carried out in a few dozens of steps. At the beginning of the each step, while the two systems are in equilibrium, pressure is recorded and *separating valve* is then closed so that the pressure of sample system is known. If the test is in the absorption stage, after closing the valve, pressure inside the measuring system is increased slightly by introducing some hydrogen into the system and then the pressure is recorded. After opening the *separating valve*, pressure will clearly change. If no absorption occurs, new equilibrium pressure can be calculated with the ideal gas law,

$$P . V = n . R . T , \quad (3.2)$$

where R is gas constant and n is the number of moles of the gas. If absorption occurs, the final pressure will obviously be different than the calculated value and the amount of gas absorbed in this step can easily be calculated by the difference in pressure using the same relation, i.e. Equation 3.2.

In other tests such as absorption/desorption kinetics, temperature programmed absorption/desorption and absorption/desorption cycles, additional gas is not added to the system (and separation valve is always open) during the measurements; so amount of absorbed gas can be calculated easily using the pressure change (and temperature change in temperature programmed tests). Equation 3.2 may require some modifications under high pressure, since gas behavior starts to deviate from linearity.

A schematic layout of the set-up is shown in Figure 3.9. Set-up is made up of three major parts; measurement system, sample system (with a furnace) and automation module.

Measurement system consists of a reservoir, pressure gauges and pneumatic valves. The reservoir makes up the greater portion of the measurement system. Three different pressure gauges are installed, pressure ranges of these gauges are 70 bar (P1), 15 bar (P2) and P3 (2 bar). P1 is always connected to the measurement system; but other gauges are protected by pneumatic valves.

Depending on the operating pressure of the test, proper gauge is chosen and data obtained from the chosen gauge is used in calculations. P1 is only used for online checking of the pressure, if the read value is larger than the range of the chosen gauge, pneumatic valve of the gauge is automatically closed. Therefore the volume of the measurement system (V_r) depends on the gauge chosen, so three different values of V_r were measured and these values are used in calculations. The measured values at 25°C are 48.7 cc with P1, 52.4 cc with P2 and 51.5 cc with P3.

Measurement system has three connections; vacuum, hydrogen and argon. A fourth gauge is used to observe the vacuum level. Vacuum gauge (Pv) is only operated under vacuum conditions and it is protected against positive pressure by one of the pneumatic valves (V1), i.e. it could not be opened, or immediately be closed (if already open) unless the pressure read by P1 is less than 1 bar. Technical details of these four gauges are listed in Table 3.2.

Table 3.2 Technical details of the pressure gauges used in the PCT apparatus.

Pressure Gauge	Technical Details
P1, Druck PMP-4010	Max. 70 bar, $\pm 0.04\%$
P2, Druck PDCR-130	Max. 15 bar, $\pm 0.1\%$
P3, Keller PAA-23	Max. 2 bar, $\pm 0.2\%$
Pv, Alcatel AHC 1010	Min. 5×10^{-19} mbar, 15% deviation, 5% repeatability

Sample system starts from the valve V5 and it consists of a filter unit, a manual valve and the sample reactor. Sample reactor is detachable through a fitting connector and it can be moved to a glovebox without exposing its content to air. A furnace can be moved upwards to heat-up the sample reactor, the temperature of which is controlled by the automation module. The sample system without the sample in it had a total volume of 16.2 cc referred to 270°C reactor temperature.

Automation module consists of Gefran Gilogik II high performance distributed I/O system which comprises 8 input A/D converter with 16 bit resolution for measurements of temperature and pressure, digital input and output modules for the control of pneumatic valves (as well as the furnace) via solid state relays. The unit also comprises 24V – 6.5A power supply unit, for connection of pressure/vacuum gauges as well as for activation of solid state relays. Automation platform is connected to a computer where the process flow is followed and controlled by a dedicated program.

Communication between the platform and computer is provided by the Ethernet module using the TCP protocol. A graphical user interface was designed including all the codes related with the process inputs and outputs, i.e. opening a valve, heating the furnace, reading pressure output and converting the value to real pressure unit, etc. The user interface was designed by means of Microsoft Visual Studio 2010 software, using the Visual Basic programming language.

In addition to the manual control of the system and process monitoring, codes regarding the automatically controlled measurements or experiments together with online data collection were implemented into the graphical user interface.

Pneumatic valves (Swagelok, diaphragm-sealed) are operated by compressed air maintained at 6 bar pressure via solid state relays. These are controlled by the digital output module where the signals are sent to relay which (de)activates a solenoid valve either providing or releasing the pressurized air to the pneumatic valve. Pneumatic valves are opened if the pressurized air is higher than a specific value and indicator switch sends a back signal to the digital input module if the valve is opened so that the opened and closed valves could be monitored in the graphical interface.

The signals that come from the gauges (pressure/vacuum gauges) are in volts which are converted to signals in mA in Gefran Gilogik II by external signal isolators and then digitized. Digital values are then converted to real pressure units by the program.



Figure 3.10 A photograph showing the general view of the current PCT setup in our laboratory (assembly of thermal insulation is in progress).

Similarly, signals coming from the thermocouples are received by an analog-to-digital converter, but these signals are first passed through the analog signal isolator where the operating temperature span is adjusted for every thermocouple. In this way, data resolution of the A/D converter is used more efficiently.

Temperature of the system volume inside the thermally insulated enclosure and also the temperature of the piping remaining between the enclosure and the sample reactor are measured using a J-type thermocouple (Tr). Two K-type thermocouples were used inside the furnace; first one is used for the sample temperature measurement (Ts) and the second one is used for the furnace temperature measurement (Tf). The temperature of the furnace was controlled by a PID algorithm embedded in the program through a relay in on-off control mode.

3.3 RESULTS & DISCUSSION

3.3.1 Synthesis of Nickel Nanoparticles

Preliminary experiments with thermal plasma synthesis were carried out with Ni. This is one of the constituent in Mg₂Ni. Ni was preferred over Mg since it has a higher melting - boiling point and also it is less reactive.

The plasma system was operated at 25 kW using parameters given in section 3.2.2. The unit was operated for 15 minutes with Ni powder at a feed rate of 3 g/min. Powders collected in bottom, cyclone and powder collector were removed and examined with SEM. Powders collected from the bottom collector are given in Figure 3.11(b). These powders are quite comparable to the starting powder given in Figure 3.11(a) except for their shape. They are spherical in shape which was derived from powders melted rather than evaporated. Powders have taken up spherical shape so as to minimize their surface energy.

Powders collected from the cyclone unit were also spherical in shape but much smaller (around several microns) in size and were decorated with nanoparticles, Figure 3.12(a). These have probably originated from incompletely vaporized liquid droplets, or highly coagulated nanoparticles. Another reason could be the relatively high exposure of some nuclei to moderate temperatures so that more time was available for the particle growth. Large agglomerates of fine particles were also present in the cyclone, Figure 3.12(b).

SEM image of powders collected from the powder collector are shown in Figure 3.13. Here the particles are quite fine and they are again spherical in shape. Mean particle size was 80 nm with a standard deviation of 15 nm (determined over nearly 50 particles analyzed from SEM images). These were obviously derived from the evaporation-condensation process.

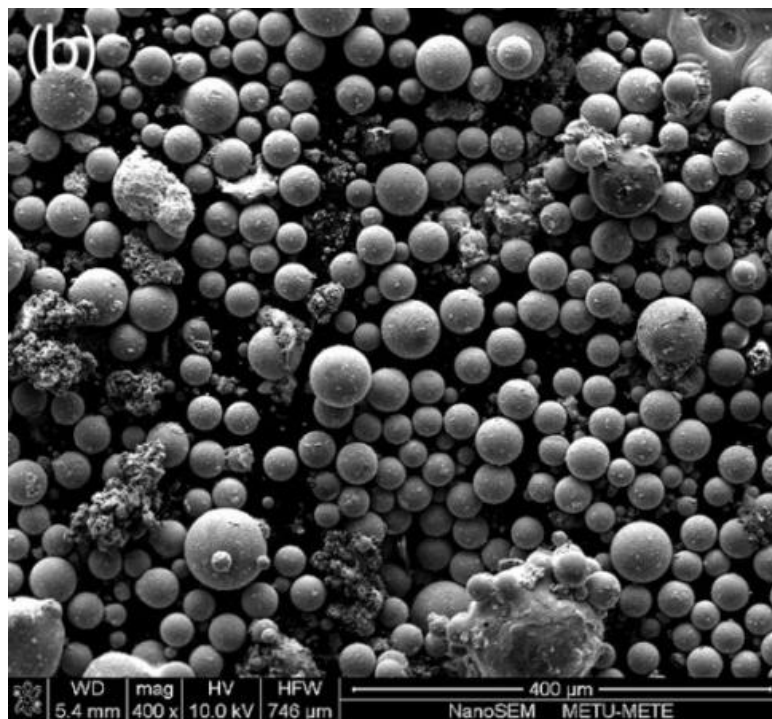
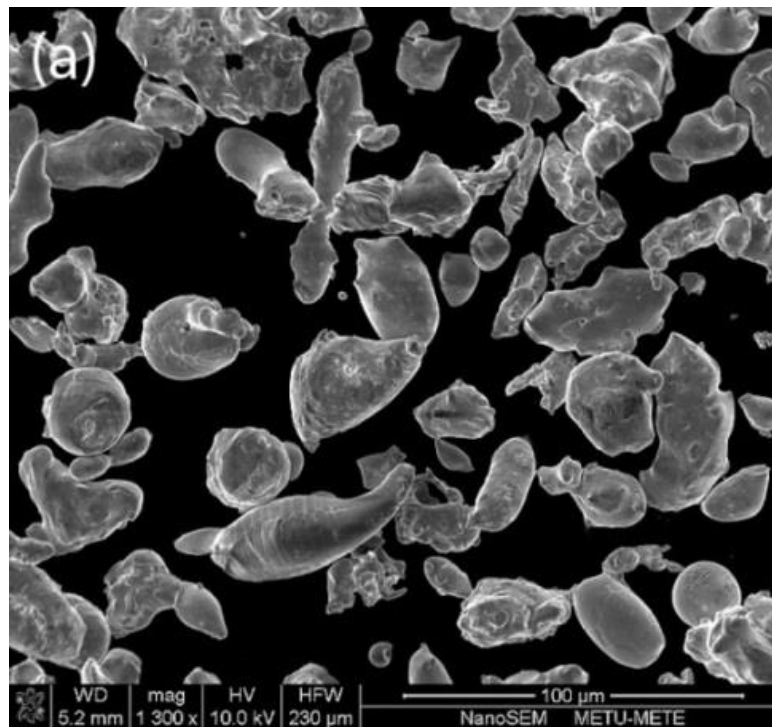


Figure 3.11 SEM images of (a) initial powders and (b) product collected from bottom collector.

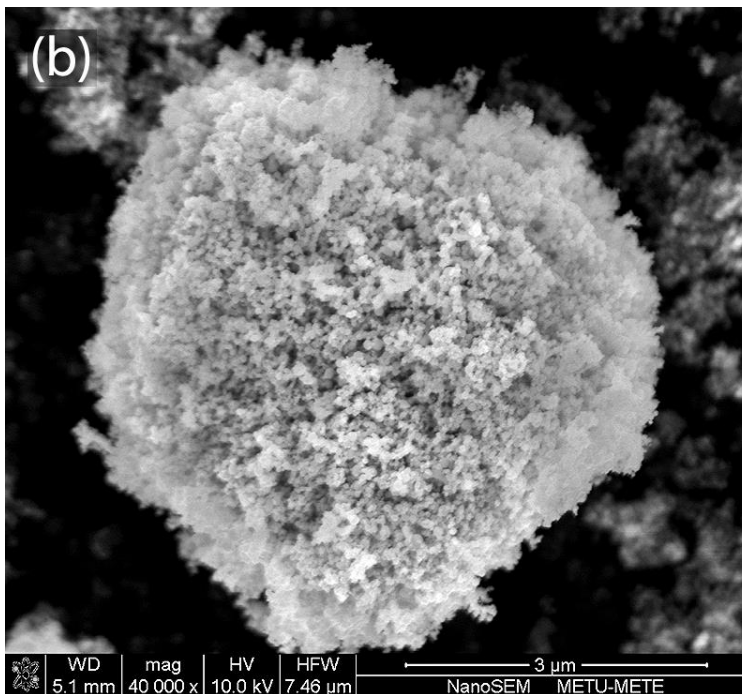
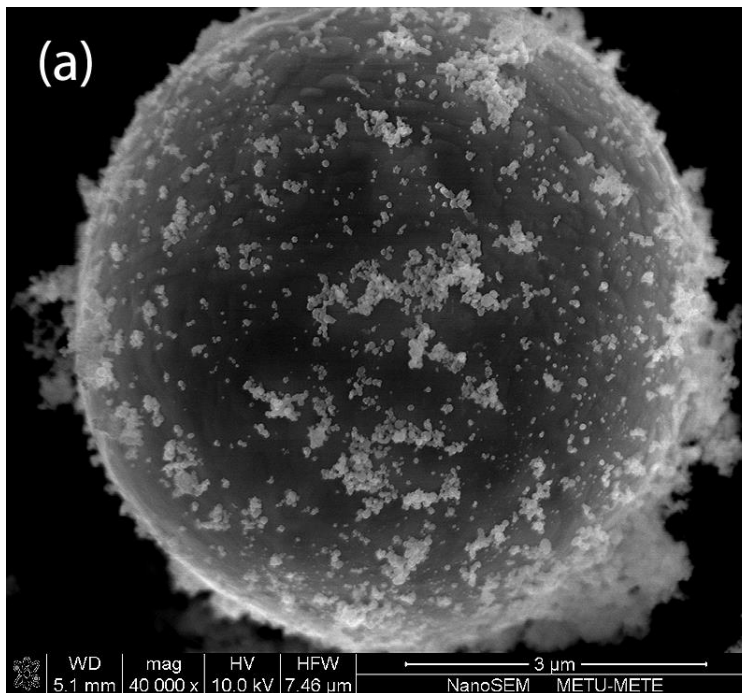


Figure 3.12 SEM images of powders collected from cyclone; (a) a large particle decorated by fine particles and (b) a large agglomerate made up of fine particles.

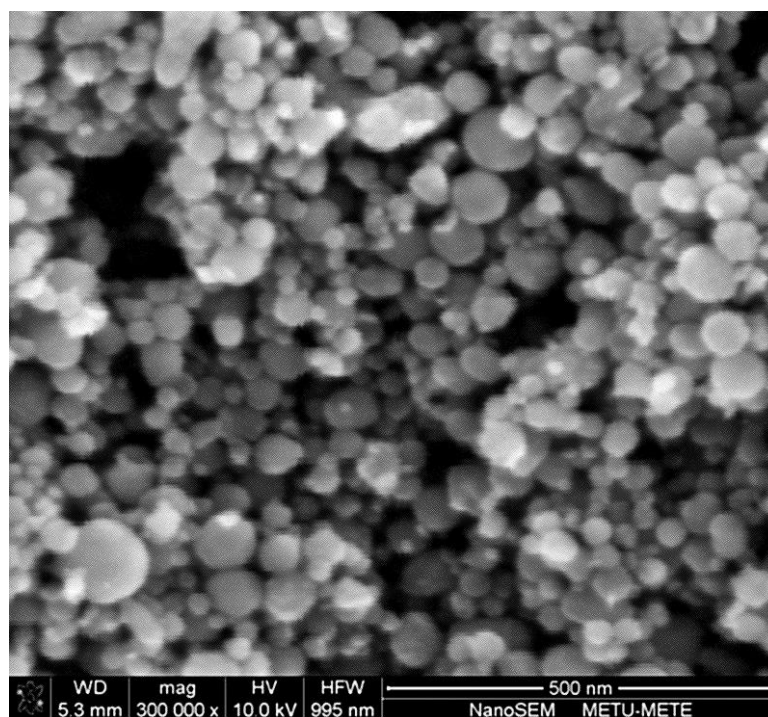


Figure 3.13 SEM image of powders collected from the powder collector.

3.3.2 Synthesis of Nanoparticles from Pre-alloyed Mg₂Ni Powders

Two different experiments were conducted with the pre-alloyed powders. They were either injected using the top injection probe or injected from the bottom probe. Samples collected were characterized with X-ray diffraction.

X-ray diffractogram of the nanopowders (collected from the powder collector) obtained using the top injection probe is given in Figure 3.14. Phases present in this sample were mainly Ni (ICDD# 4-0850) and MgO (ICDD# 45-0946). No significant Mg₂Ni was present in this sample. This implies that Mg₂Ni disintegrated within the plasma into its elements. Moreover, Mg formed in this way was oxidized to MgO.

The use of bottom probe allows the injection of the powders into a plasma zone of a lower temperature. The injection probe in this experiment was located at $z=372$ mm. XRD pattern of nanoparticles collected in this geometry is included in Figure 3.14. Here, the main phases present were Ni (ICDD# 4-0850), Mg (ICDD# 35-0821) and a small amount of MgO (ICDD# 45-0946). A trace of Mg₂Ni (ICDD# 35-1225) could also be detected in the diffractogram located at 20.8° (2θ), i.e. (003) plane.

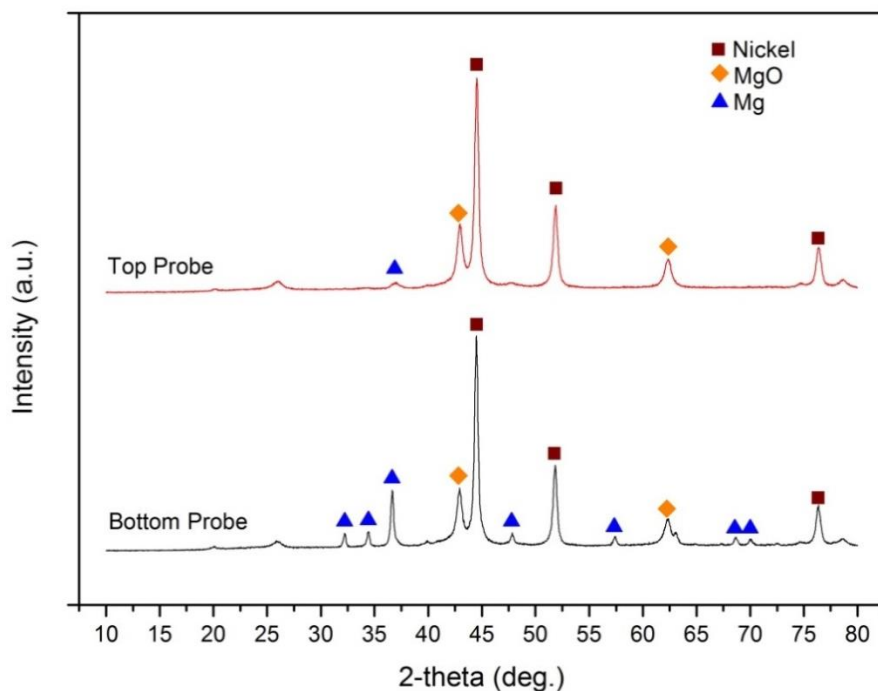


Figure 3.14 X-ray diffractograms of the samples obtained from pre-alloyed Mg_2Ni precursors using the top injection probe and bottom injection probe.

3.3.3 Synthesis of Nanoparticles from Mg and Ni Elemental Powders

In this part, Mg and Ni were sent into the plasma separately. Since boiling and melting temperatures of Mg are lower than those of Ni, it was decided that Ni could be fed through the top probe as it provides a more effective heat transfer between the plasma and the particles, while Mg could be fed through the bottom probe (positioned at $z = 372$ mm). Also, results of the previous experiment with the Mg_2Ni precursor showed that, the use of bottom probe was more successful in preventing/reducing the tendency for the oxide formation.

XRD pattern of nanopowders obtained in this geometry is given in Figure 3.15. Considerable fraction of the sample was Mg_2Ni (ICDD# 35-1225). The other phases present were Ni (ICDD# 4-0850), Mg (ICDD# 35-0821) and MgO (ICDD# 45-0946). The amount of Ni in the sample was quite comparable to that of Mg_2Ni .

In order to maximize the amount of Mg_2Ni , a new experiment was performed. Here, in order to compensate the unreacted Ni, the amount of Mg fed to the plasma was increased from 1.2 g/min to 1.6 g/min. However, there was only a slight increase in the Mg_2Ni content, and intensity of Mg peaks increased considerably. Fortunately, intensity of MgO peaks did not increase proportionally and the fraction of Mg_2Ni was slightly higher compared to that of Ni.

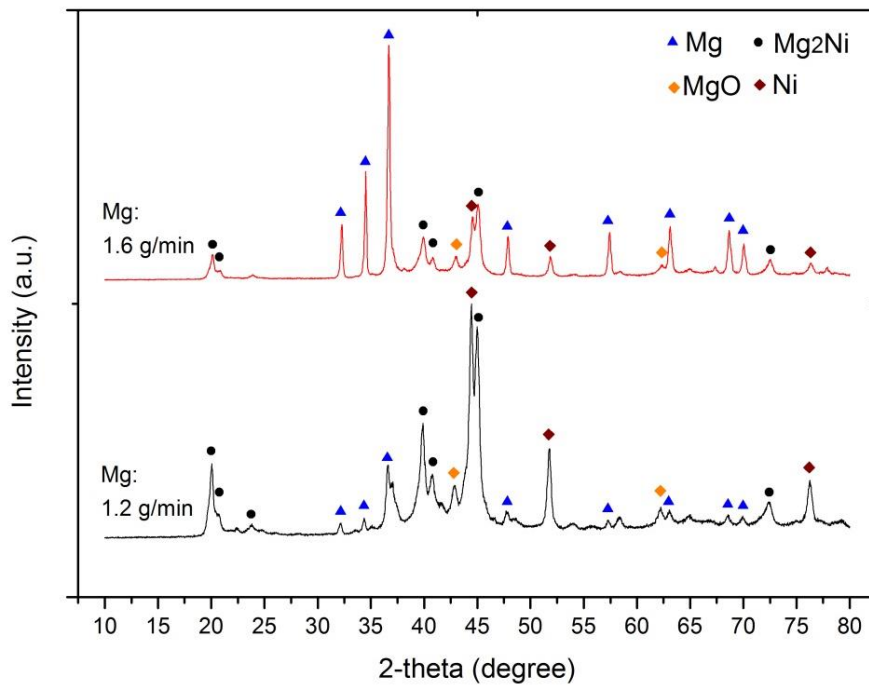


Figure 3.15 X-ray diffractograms of the samples obtained by feeding Ni (1.8 g/min) and Mg (1.2 and 1.6 g/min) separately (Ni - top injector, Mg – bottom injector).

3.3.4 Maximization of Mg_2Ni

Following the experiments reported above, it was decided to use elemental powders in two-probe configuration since the fraction of Mg_2Ni was highest at this geometry. So as to further increase Mg_2Ni yield, an approach was adopted in which the position of Mg probe was changed in the reactor. It was anticipated that, moving the injector towards the plasma torch would affect the precursor penetration into the different regions of the plasma and could lead to alterations in the volume fractions of the phases formed. Experiments involved the use of five locations; $z= 372, 322, 272, 222, 172$ mm.

XRD pattern of the nanopowders obtained with different values of ‘z’ are shown in Figure 3.16. It is seen that, patterns of the first two experiments (z= 372 and 322 mm) are quite similar yielding Mg₂Ni of comparable volume fractions. When the bottom injector was positioned at z = 272 mm, an increase in the Mg₂Ni yield was observed; but still there was a significant amount of Ni (ICDD# 4-0850). In addition, MgO (ICDD# 45-0946) which was present in the previous samples (z = 372, 322 mm) was reduced considerably. When injector tip was moved further towards the plasma (z = 222 mm), the same trend did not continue. The fraction of Mg₂Ni was now decreased while MgO peaks became comparable to those observed in the earlier positions. It might be worth mentioning that at z = 272 mm, the tip of the injector is located just below the inlet of the quenching gas.

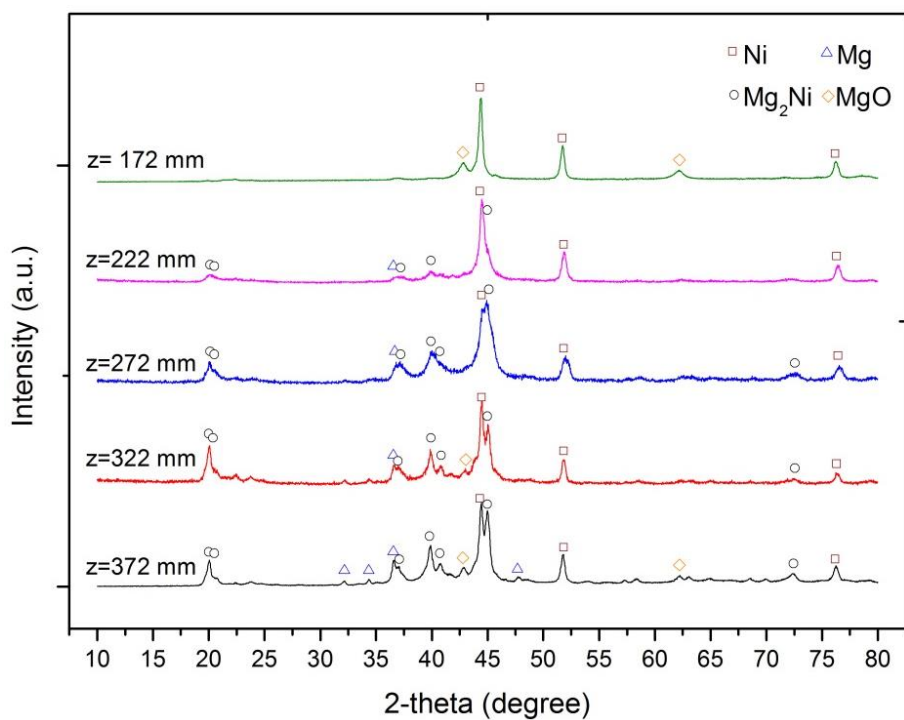


Figure 3.16 XRD patterns of samples obtained by feeding Ni via top injector and Mg via bottom injector while the position of the latter (z) changed from 372 to 172 mm.

In the final experiment, the bottom injector was moved to (z = 172 mm), i.e. the minimum ‘z’ value reachable with the current probe. This position was above the inlet of quenching gas; see Figure 3.3(a). XRD pattern obtained for this case was quite different as compared to the previous cases. As seen in Figure 3.16, nearly all Mg was oxidized and there was almost no Mg₂Ni formation.

The resulting nanopowders were analysed with SEM-EDS in each injector configuration so as to determine the amount of Mg and Ni. Results of these analysis are given in Table 3.3. It should be noted that despite the fact that Mg and Ni were fed into the system in the same ratio (Mg:Ni=2:3 by weight), the ratio in the resulting powders were quite different. The ratio decreases up to $z=222$ mm beyond which the value is increased.

Table 3.3 Elemental analysis results of the products collected from the powder collector (Pure Mg_2Ni : 45.3 wt% Mg – 54.7 wt% Ni).

Bottom Injector Position	Mg (wt%)	Ni (wt%)
$z = 372$ mm	55.2	44.8
$z = 322$ mm	47	53
$z = 272$ mm	44.7	55.3
$z = 222$ mm	36.4	63.6
$z = 172$ mm	57.2	42.8

A rough calculation shows that the amount of heat required to evaporate Mg from room temperature to the vapor phase is approximately 15-20% lower than the heat required for the evaporation of Ni. This was the reason why the ratio of feed rate was maintained at Mg:Ni=40:60 as opposed to the stoichiometric feed rate of Mg:Ni=45.3:54.7.

In fact, the degree of evaporation depends on many other parameters which may be more decisive such as particle flow history and ability of penetration into plasma, thermal conductivity and size of powders, turbulence gas flow and recirculation zones inside the reactor. The values reported in Table 3.3 also show that the position of injector is also influential in affecting the degree of evaporation. Since Ni is fed from the top injector, the position of which was not modified, the values reported in Table 3.3 may be used as an indication of the yield of Mg evaporation. It is seen in Table 3.3 that, fraction of evaporation was higher for Mg, but it decreased with the decreasing value of 'z'. It is interesting to note that the value increases again beyond $z=222$ and reaches to its highest value when the tip moves above the quenching zone, i.e. $z=172$.

The results reported above imply that the quenching gas can play an obstructive effect in Mg evaporation efficiency. As can be seen in Figure 3.3(a), the position at $z=222$ mm is nearly at the same level as the inlet of the quenching gas. More intense gas flow just at the inlet is expected to disturb the flow of Mg which occurs in the opposite direction. At the maximum position, $z=172$ mm, the injector tip is above the quenching zone and Mg easily reach the plasma. Noticeably, observed Mg content in powders increased to 57.2 wt% in this case. However, the penetration of magnesium into the hotter region of plasma just improved the Mg yield, but did not lead to Mg_2Ni formation.

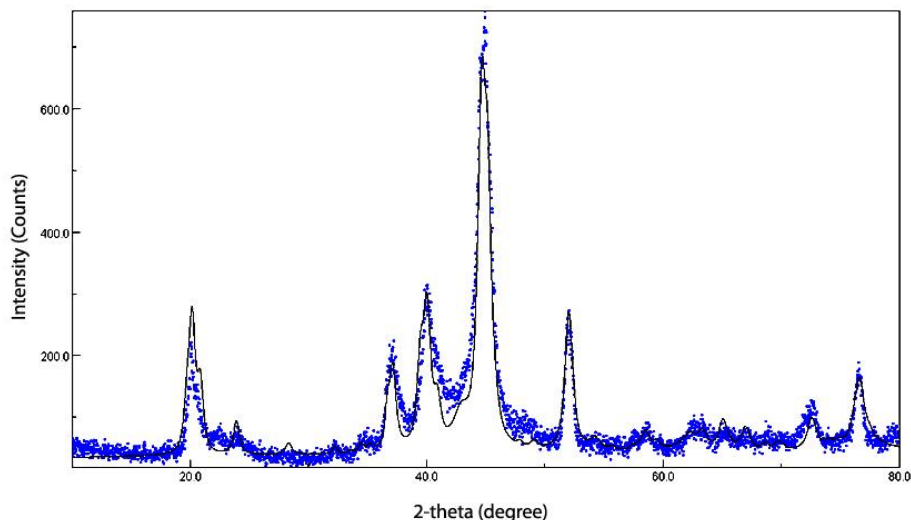


Figure 3.17 Rietveld refinement of the X-ray diffractogram of powder synthesized when $z = 272$ mm ($R_w = 24$, $\text{sig} = 2.24$).

As pointed out above in XRD measurement, Mg_2Ni yield was maximum at $z=272$. It is interesting to note that $\text{Mg}:\text{Ni}$ ratio is closest at this value of 'z' to the stoichiometric value. XRD pattern at $z=272$ mm was refined with Rietveld method using MAUD software. The refined pattern is shown in Figure 3.17. Here, there were some mismatch of the refined pattern with the data which was probably due to the low resolution of the pattern and perhaps also due to the presence of preferred orientation, particularly in the Mg_2Ni phase. The Rietveld analysis yields a weight fraction of 55 wt% for Mg_2Ni . The values for Ni and Mg were 26.5 wt% and 6.7 wt%, respectively. The remaining phase was MgO with 12 wt%. The total value of Mg content calculated from these phases is 41.4 wt%. This is quite close to the EDS value of 44.7 wt% Mg reported in Table 3.3.

This sample with maximum Mg_2Ni content was further analyzed with regard to its particle size. BET analysis yielded a specific surface area of $16 \text{ m}^2/\text{g}$. Assuming all the particles are spherical in shape, average particle size was calculated using Equation 3.1. This has yielded a value of 98 nm (average density used was determined from the weight fractions calculated by the phase fractions obtained via Rietveld analysis). This value was quite close to values obtained with SEM measurements which yielded an average particle size of 89 nm (with a standard deviation of 39 nm) determined over 110 particles (Figure 3.18).

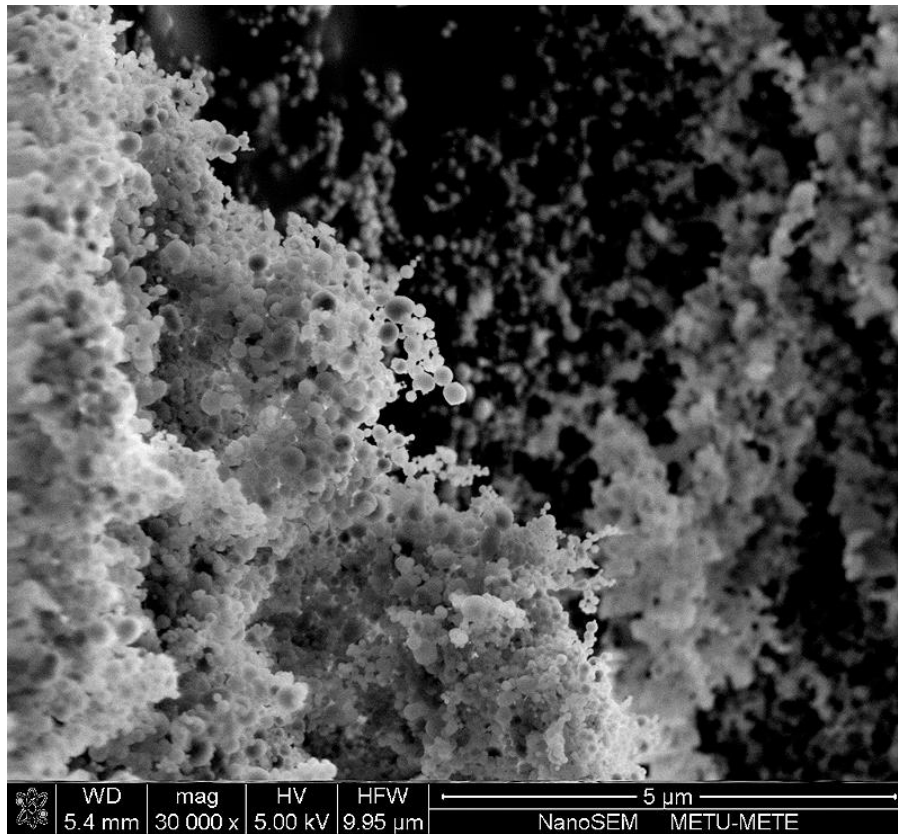


Figure 3.18 SEM image of powders synthesized using Ni (top injector, $z = 0$) and Mg (bottom injector, $z = 272$ mm) precursors.

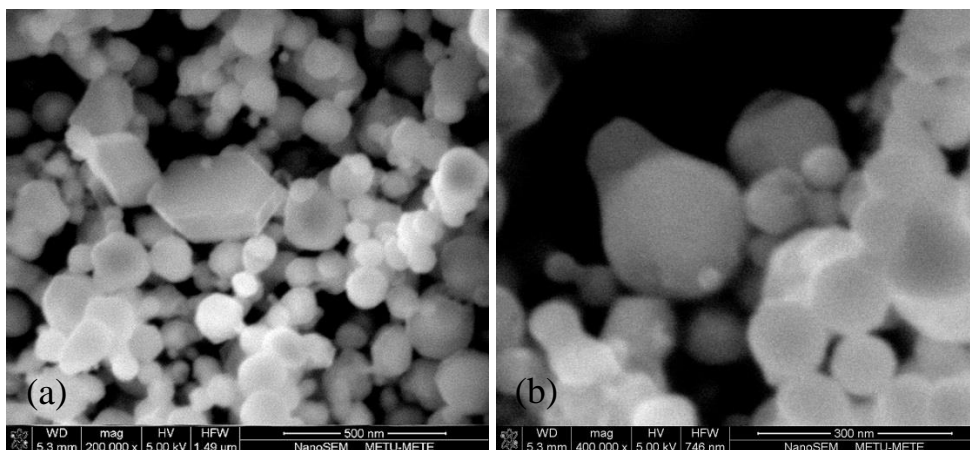


Figure 3.19 High magnification SEM images (a) and (b) of powders synthesized using Ni (top injector, $z = 0$) and Mg (bottom injector, $z = 272$ mm) precursors.

Returning back to the conditions of successful synthesis of Mg_2Ni with thermal plasma, it may be worth mentioning that high temperature exposure of Mg should be avoided. More importantly, when Mg and Ni follow similar pathways in the reactor, they prefer to nucleate separately, which is probably due to the large differences in their nucleation temperatures. When Mg feeding rate or its feeding position was changed, Mg_2Ni/Ni ratio does not change significantly as long as the injector position was below the quenching inlet. This may be interpreted as an indication that the flow history of Ni was more deterministic in the Mg_2Ni yield. As having higher nucleation temperature, some portion of Ni nucleates before it encounters the Mg atoms in the gas phase and after that both start to co-condense, while some Mg and Ni still nucleate separately.

Rapid cooling conditions make homogeneous nucleation more favorable. It can be expected that, when cooling rate is slow, Ni would largely complete its nucleation and its considerable growth so that Mg would nucleate heterogeneously on the Ni particles. If the cooling is quite fast, this time both Mg and Ni would nucleate homogeneously; however, number of cluster collisions would be insufficient for the Mg_2Ni formation and free Mg nanoparticles would be prone to oxidation. Therefore, it is expected that there would be an optimum condition for cooling rate for the Mg_2Ni formation. Additionally, a more homogeneous pathway for Ni and a sharper temperature gradient in the plasma flame may increase the Mg_2Ni content by decreasing the probability of separate nucleation of Ni.

3.3.5 Hydrogenation of Mg_2Ni Nanoparticles

The sample with Mg_2Ni content of 55 wt% was evaluated with regard to its hydrogenation behavior. This was carried out by means of temperature programmed sorption experiment which offers a fast and simple characterization of the hydrogen storage properties.

The experiment simply involved heating the sample under vacuum to the selected temperature (320°C) and charging hydrogen to the sample at the prescribed pressure. Having loaded the sample with hydrogen, the reactor is let to cool down to room temperature. During this treatment, the sample was expected to be hydrogenated, i.e. Mg_2Ni would react with hydrogen yielding Mg_2NiH_4 . This is reflected by a pressure change in the reactor which is more than that expected by the temperature change.

Having hydrided the sample, the temperature programmed sorption was initiated by heating the sample and monitoring the pressure change in the reactor. The pressure increases as the temperature is increased, but upon reaching the desorption temperature, the rate of pressure change increases rapidly.

Having followed the desorption of the sample and upon reaching the selected temperature, the measurement was switched to absorption mode. The reactor was cooled down and the pressure change was monitored as the temperature reached room temperature. During cooling the pressure decreases, but upon reaching the absorption temperature, the rate of pressure change is increased considerably.

The experiment therefore yields two curves, one for desorption and the other for absorption. Figure 3.20(a) shows desorption/absorption curves recorded at 9.7 bar initial pressure. It is seen that the sample desorbs its hydrogen in the temperature interval of 235–275°C and absorbs it at temperatures between 200–240°C. Similar curves determined at nominal initial pressure of 6 and 2.9 bar are given in Figure 3.20(b) and 3.20(c), respectively.

A rough determination of absorption and desorption temperature may be made by considering the mid-temperature in the relevant transition zone given in Figure 3.20. However, data reported in these figures refer to non-steady state experiments and therefore should be treated with caution. Van't Hoff construction, though not applicable for such data yields a desorption temperature that is around 200°C at 1 bar pressure. The nature of measurement carried out in the experimental set-up is such that this temperature is probably higher than what was calculated here. Nevertheless, data implies that there is no drastic reduction in the stability of Mg_2NiH_4 and temperatures similar to those used in ball milled Mg_2Ni would be required for the release of hydrogen from the synthesized nanoparticles.

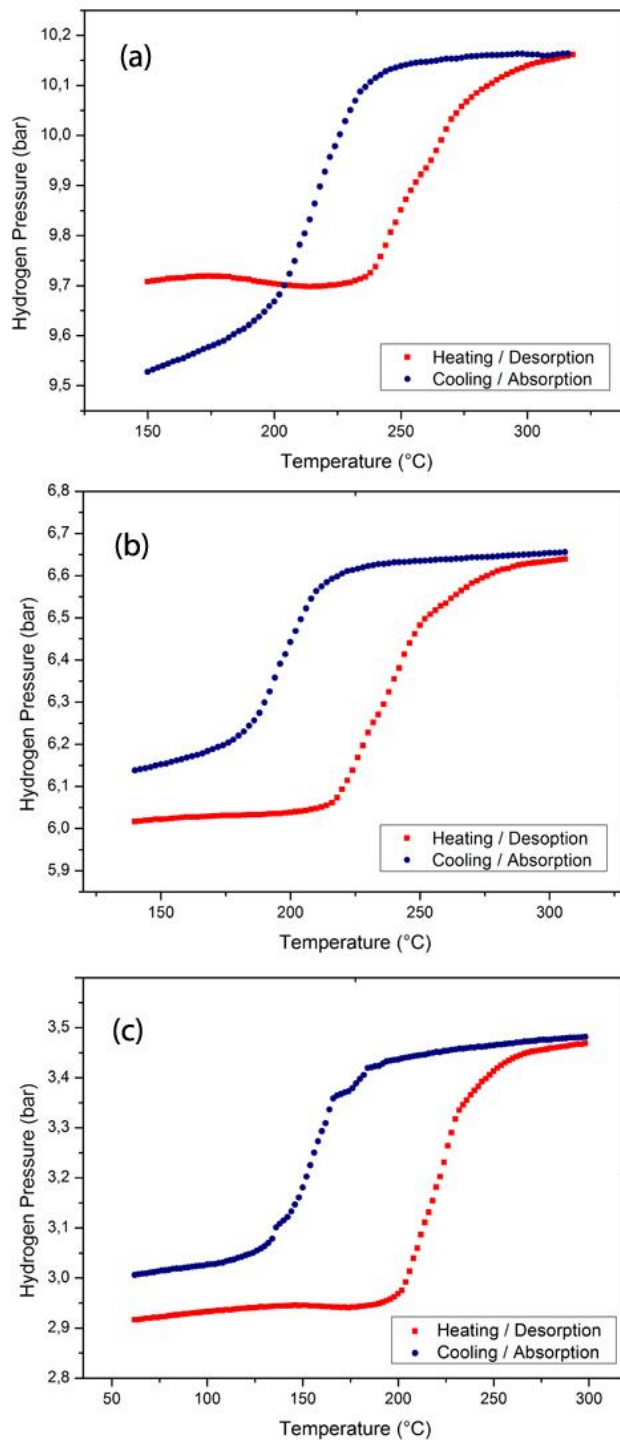


Figure 3.20 Temperature programmed sorption curves for Mg₂Ni nanoparticles. The curves refer to initial nominal hydrogen pressure of approximately (a) 9.7 bar, (b) 6 bar, (c) 2.9 bar.

3.4. CONCLUSIONS

In this chapter, it was shown that the induction plasma method is an effective way of synthesizing nanoparticles in large-scale. Particles were generally spherical in shape and less than 100 nm in size. Ni nanoparticles were successfully synthesized in one-step without being oxidized. It is also possible to synthesize multicomponent materials via induction plasma method. Intermetallic Mg_2Ni compound with a significant yield was synthesized; but it was seen that the injector configuration of the precursors was quite decisive for the relative content of products. Feeding Ni from the top of the plasma and Mg from the bottom of the plasma was found to be the most effective feeding configuration.

It was also found that Mg_2Ni nanoparticles react readily with hydrogen. Van't Hoff plot derived from temperature programmed sorption indicates that despite extremely small size, the desorption temperature of nanoparticles is little affected and not much less than those obtained with ball milling.

CHAPTER 4

CARBON ENCAPSULATION OF Mg-Ni NANOPARTICLES

4.1 INTRODUCTION

It is well known that the physical and chemical properties of materials change as their size decrease down to nanoscale. This arises partly due to extremely large surface area of these particles. Nanoparticles are of great scientific and industrial interest for a wide range of applications since these novel materials may offer superior size-dependent properties. In the case of metallic nanopowders; however, there are also some important drawbacks related to their size such as agglomeration and higher sensitivity to oxidation. These drawbacks usually limit their application and necessitate protective measures to be taken during their handling. One solution to this problem is seen as the stabilization of metallic nanoparticles by covering them by an inert material.

Stabilized nanoparticle materials providing such a protection against oxidation and agglomeration may be produced through several approaches. These include dispersion of particles in a protective matrix, encapsulation of particles by a different shell material and intercalation or infiltration into other protective structures. It is important to note that the geometry of such nanocomposites as well as the fractional amount of metal contained in the composite depends on the stabilization approach. Core-shell nanoparticles have been attracted considerably in this respect, since the geometry in this approach is mostly spherical and metal fraction in the composite is relatively high which are desirable for most applications. Materials used as protective shell include carbon (Xiaomin *et al.* 2006), silica (Wang *et al.* 2008), boron nitride (Tokoro *et al.* 2004), polymers (Borodina *et al.* 2009), Pt (Chen *et al.* 2008), intermetallics such as Mg₁₇Al₁₂ (Liu *et al.* 2012), etc. Among these shell materials, carbon is quite promising because it exhibits a good chemical and thermal resistance.

Carbon encapsulated metallic nanoparticles have been synthesized mainly by the arc discharge (Dong *et al.* 1999), thermal plasma (Bystrzejewski *et al.* 2011), hydrogen plasma (Liu *et al.* 2012), chemical vapor deposition (Xiaomin *et al.* 2006) and flame synthesis (Athanassiou *et al.* 2006). Other methods that could be used for this purpose include combustion synthesis (Borysiuk *et al.* 2008) and wet (chemical) synthesis (Sun

and Li 2005), etc. Metals such as Fe, Co and Ni have been well studied as carbon encapsulated metallic cores (Sun *et al.* 2000, Dong *et al.* 1999, Bystrzejewski *et al.* 2005). Other materials used as a core in core-shell structure are Cu, Ti, Pd, Ag, NiFe (Jiao and Seraphin 1998, Wang 1994, Sun and Li 2005, Teunissen *et al.* 2001); hydrides as sodium borohydride (Borodina *et al.* 2009) and carbides of Fe, Cr, Mo, W, T, and Si (Song and Chen 2003, Oku *et al.* 1998).

Carbon encapsulated metal cores have mostly been observed in systems not forming their stable carbides such as Co, Cu, Fe, Ni, Pd. However, according to Elliott *et al.* (1997), even carbide forming metals could be encapsulated by carbon through the use of a suitable encapsulation procedure.

Several carbon encapsulation mechanisms have been reported in literature (Elliott *et al.* 1997). Saito *et al.* (1994) suggested an encapsulation model which predicts the carbon layer formation with initial clusters of metal-carbon mixtures and subsequent expelling of carbon atoms to the surface during the crystallization. The model was based on the observations regarding the encapsulation process using graphite arc method. According to this model, encapsulation is an alternative to the formation of single wall carbon nanotubes. If the basal plane of graphite is perpendicular to the particle surface, this leads to the formation of carbon nanotubes. If not, this leads to the particle encapsulation. In another similar model, Seraphin (1995) suggested that the nucleation and growth occur between the outer graphene layer and the core particle by the expelling of carbon atoms from the core. This explains why there is an open space inside the encapsulated particles which originates from the shrinkage resulting from these expelled carbon atoms.

In the critique of Saito-Seraphin model, Elliott *et al.* (1997) stated that the open space would be explained by expelled carbons only if an inside-out growth is present. They further stated that the model is applicable when the carbon content of the core after the formation of first layer is over 20% by volume. In the case of outside-in growth, volume originated from the shrinkage of the core would be compensated by the volume of new graphene layers, so that the Seraphin's open space explanation would not be valid in these cases. It was stated also that the thermal contraction would not cause such an open space as the carbon contraction is actually larger than those of the most metals.

In the model proposed by Elliott *et al.* (1997), final morphology of an encapsulated powder is dependent on the formation mechanism of the first graphene layer such that the shell growth proceeds by duplicating always the previous layer. Two dominant processing parameters are described; local path carbon/metal ratio and global carbon/metal ratio. The morphology and geometry of the primary nanoscale products are dependent mostly on the local carbon/metal ratio. A schematic of the possible mechanisms of particle/carbon structure formation in this model can be seen in the Figure 4.1 taken from Elliot *et al.* (1997).

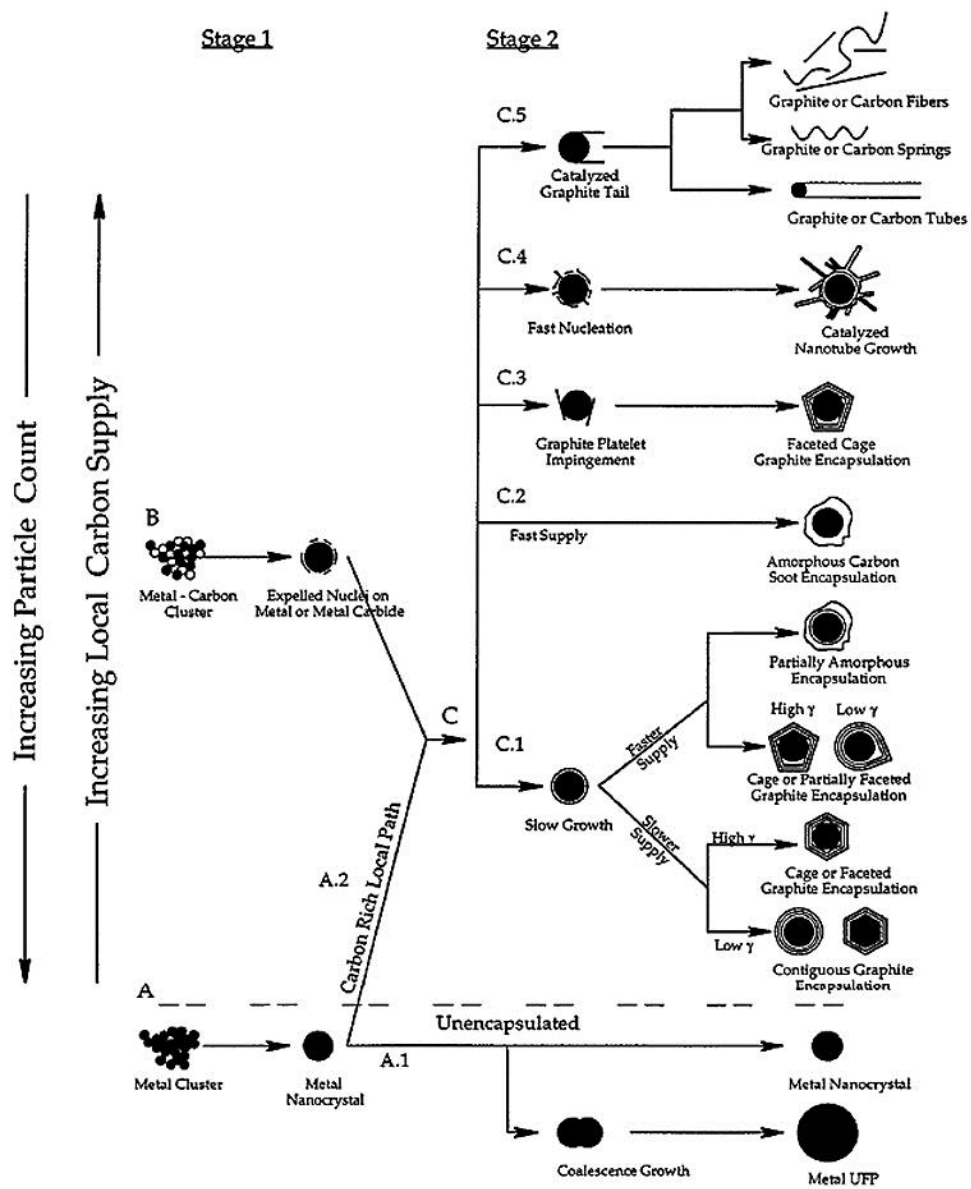


Figure 4.1 Effect of local carbon/metal ratio on the possible formation mechanisms for particles and carbon structures (Elliott *et al.* 1997).

In a typical nanopowder reactor, physical processing routes are usually not homogeneous for all particles. Different local carbon/metal ratios, quench rates, particle densities and recirculation histories are possible and as a result of this, more than one mechanism may operate at the same time. In this model, initially metal-carbon or pure metal clusters are formed. During the encapsulation process, required carbon may come from the core material itself (internal source) or from the gas phase surrounding the particle (external source). If the source is internal, clusters start to crystallize as the temperature decreases and at the same time excess carbon atoms diffuse to the surface and encapsulate the core particle.

According to Elliot *et al* (1997) another possibility is the deposition of carbon atoms (external carbon source) on the particle surface. Carbon deposition on the surface may occur if high carbon supply is faced during the particle flow. During this, graphite may nucleate on the existing particle surface by means of catalytic or heterogeneous nucleation. At the same time homogeneous nucleation of carbon in the gas phase may also occur. Elliot *et al.* (1997) further stated that the surface energy of the core-graphite interface is important and the probability of defect formation increases with low surface energy. In a similar manner, high surface energy would inhibit the encapsulation of powders since defects are required for the bending of graphene layers. Another form of carbon can be formed by fast nucleation or impingement of graphite sheets; these may result in radial growth of the graphite sheets from the particle. Moreover, crystallization of carbon atoms may not be completed; rapid deposition or carbon expulsion initiated by rapid quenching can result in amorphous carbon formation.

Elliot *et al.* (1997) further pointed out that carbon deposition is realized inside-out which means that the new layer is formed on the existing layer surface. However, layer formation by carbon expulsion takes place outside-in. New layer pushes the existing surface layer or carbon atoms diffuse through the surface and form a new layer inside. If there is enough open space between the core and the surface layer, new layer is formed on the inside. Catalytic surfaces help to the formation of first encapsulating layer by providing fast nucleation rates. Then other layers mimic the existing ones and encapsulation process continues more easily.

If the dominant mechanism is carbon expulsion from the core, larger size particles would be encapsulated by more layers of graphene, since volume increase is higher than the surface area increase in such a situation. Similarly, if the dominant mechanism is the external carbon deposition, thickness of the carbon layer would not be affected by the particle size (Elliott *et al.* 1997).

Catalytic effect of existing encapsulates were also reported by other authors. Fernández *et al.* (2009) compared the graphene layer growth in carbon encapsulated Ni particles with and without free Ni additions. It was verified in this study that the encapsulated particles would also act as catalyst for further growth of graphene layers.

Sun and Dong (2002) have synthesized carbon encapsulated Ni nanoparticles in a carbon arc discharge. A growth history of carbon shells was given. According to this study, there were no gaps or carbide phases between the carbon shell and the core, carbon atoms dissolved in molten metal and then graphite precipitated on the particle surface. Similar explanations were also made by Bystrzejewski *et al.* (2011) and Sun *et al.* (2002).

Bystrzejewski *et al.* (2007) listed some advantages of radio frequency thermal plasma reactor in forming carbon encapsulated particles. Induction plasma offers large plasma volume favoring high feed rate, low plasma velocity and high residence time of precursors which provide better carbon-carbon and carbon-metal interactions. These were reported to be favorable conditions for carbon encapsulation. Lastly, RF plasma offers a one step and continuous synthesis route for the carbon encapsulated metal nanoparticles. Bystrzejewski *et al.* (2007) synthesized carbon-encapsulated magnetic nanoparticles using $\text{Fe}_{14}\text{Nd}_2\text{B}$ powders using methane or acetylene as a carbon source.

Bystrzejewski *et al.* (2007) successfully encapsulated Fe, Fe_3C and NdC_2 nanoparticles into carbon cages. Plasma torch was operated at 50 kW and 2-5 MHz under 0.3 bar pressure, methane or acetylene flow rate was between 3–15 slpm (standard liter per minute). Non-encapsulated metal powders were eliminated by treatment in 4 M HCl for 24 hours. The cores of quasi-spherical shape were about 10-30 nm in size and carbon coatings were composed of 5-25 graphene layers. Use of methane as a carbon source was reported to be a better choice providing a well-developed crystal coating. Bystrzejewski *et al.* (2007) in a separate study reported that these encapsulated nanoparticles were thermally stable up to 500 K.

Bystrzejewski *et al.* (2011) in a subsequent study produced carbon encapsulated Fe nanoparticles using ethanol (as carbon source) and Fe powders with various sizes (18.1-77.6 μm). Encapsulation yield was decreased by increasing precursor size. Low C/Fe ratio was reported to be more useful for the encapsulating layer formation.

According to Bunch *et al.* 2008, theoretically, a graphene layer is impermeable to standard gases including helium. Figure 4.2 was taken from Berry (2013) and shows a representation of the graphene lattice. The geometric pore size here has a value of 0.064 nm which is smaller than the van der Waals radius of helium (0.28 nm) and hydrogen molecule (0.314 nm). A perfect graphene layer does not allow molecular hydrogen gas transport; however, it is known that nanoporous graphene layers may permit selective gas permeability.

Jiang *et al.* (2009) using a density functional theory has shown that nanoporous graphene membranes having pores of 2.5 Å would allow the transport of hydrogen but not methane. In another theoretical study, Du *et al.* (2011) have shown that, a graphene membrane with 6.5 Å pores would allow the separation of hydrogen gas from a mixture of hydrogen and nitrogen.

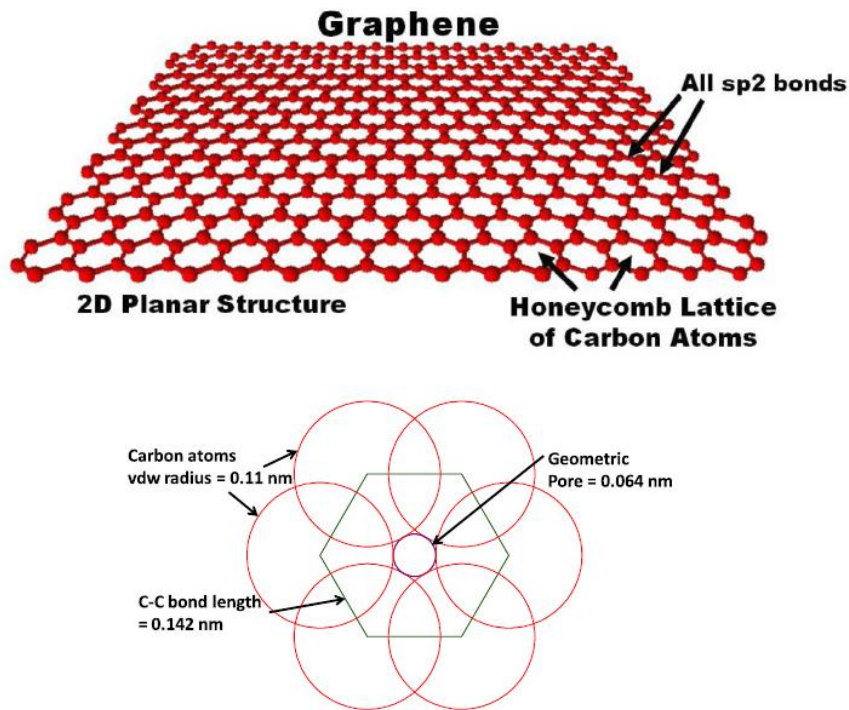


Figure 4.2 Geometrical representation of graphene lattice (upper image) and pore size (lower image), (Berry 2013).

In a carbon encapsulated particle, graphene layers are bended to provide the required curvature so that the shape is spherical. This is only possible by the introduction of structural defects. Terrones *et al.* (1996) have reported that spherical shaped carbon layers contain structural defects in the form of heptagon and octagon rings. Thus, if the encapsulates would be selective for the passage of gases such as hydrogen and not to the others such as oxygen, this would also require a careful control of the defect structure.

As indicated previously, Elliott *et al.* (1997) have shown that graphene encapsulation characteristics can be controlled by the amount of carbon supply and also supply location together with the cooling history of the particles. In the literature of carbon nanotubes (CNT's), in which the useful information can be drawn for the carbon encapsulates as

well, there are a variety of methods for the surface functionalization and purification including oxidation and acid treatment techniques. These techniques as applied produce defect generation in the graphitic network and sometimes cause to the CNT fragmentation (Pyrzynska 2010, Aviles *et al.* 2009, Datsyuk *et al.* 2008).

It is known that, carbon encapsulation of metallic nanoparticles provides protection in oxidative environment even when structural and geometrical defects exist in encapsulating layers. It can be considered that the hydrogen transport through these layers may be possible through these defects. In the case of impermeability towards the hydrogen, layers would be modified in order to deteriorate carbon shell quality. Also catalytic decoration may be added to the encapsulated particles so as to help splitting of hydrogen molecule into its atomic form on the surface.

Another aspect of carbon encapsulation is the confinement of the enclosed core. This is particularly important as there is considerable volume expansion of the core in the case of hydride formation. For instance, Ono *et al.* (1982) have reported that upon hydriding, Mg_2Ni is subject to a volume expansion of 27.81%. The possibility of a reversible toleration of carbon layers against volume changes of this magnitude is not known; but, it is clear that such a mechanism would be quite promising as a way of controlling (de)hydrogenation behavior of metal hydrides.

In this chapter, feasibility of encapsulating metallic nanoparticles with carbon is investigated with the method of induction plasma synthesis. First, Ni precursors were fed to the plasma torch together with the methane gas as carbon source. Two configurations of the precursor feeding were studied, Ni precursors were fed through top injection probe and methane was fed through bottom injection probe, or vice versa.

In the second set of experiments, an attempt has been made to encapsulate Mg with carbon. Mg powders and methane gas were used as precursors. Two feeding geometries were used. In one Mg and methane were fed through the top probe where two different rates of methane flow were studied. In the other, Mg feed rate was kept constant at 0.65 g/min and methane feed rate at 1 slpm. Here, Mg and methane were fed using separate injectors. When separate injectors were used, Mg was fed through top and methane through bottom injector, or vice versa. The experiments also involved the use of pre-alloyed Mg_2Ni powders with the top injector.

4.2 EXPERIMENTAL

Induction plasma system was operated at 25 kW under 0.97 bar pressure. A detailed description of the system was given in Chapter 3. Materials used as precursors included Methane (CH₄, 99.5% pure, Linde), nickel (99.9% pure, -325 mesh, Höganäs), magnesium (99.8% pure, -300 mesh, Alfa Aesar) and pre-alloyed Mg₂Ni (induction melted, -300 mesh). Typical duration of the production runs lasted 10–15 minutes.

With Ni, powder feeding rate was 3 g/min and methane flow rate was 2.5 slpm. Top and bottom injection probe was positioned at z=0 and z= 372 mm, respectively. With Mg₂Ni the powder feeding rate was similar, i.e. 2-3 g/min; but as a result of the large particle size distribution and irregularity of the powder morphology, it was hard to maintain a steady flow of powder.

With Mg, feeding rates of Mg were either 0.25 g/min or 0.65 g/min. Methane was used as carbon source and feeding rates were either 0.1 or 1 slpm.

Samples were examined with Jeol JEM2100F Field Emission Transmission Electron Microscope. For this purpose, a small amount of powder was added to ethanol and mixture was sonicated for 5 minutes. After 10 minutes at rest, 1-2 droplets of this liquid were dropped on a 200 mesh copper holey carbon grid. Samples were examined in high resolution mode. FFT images were used for the calculation of d-spacing values. FFT conversion and d-spacing measurements were made via ImageJ software.

4.3 RESULTS & DISCUSSION

4.3.1 Encapsulation of Nickel

Upon feeding Ni and methane to the plasma reactor, the product collected from the powder collector was mostly carbonaceous as they were black in color. In TEM images obtained from these powders, structures were mostly graphitic, but Ni particles could easily be located. Figure 4.3 and 4.4 show typical TEM images of such particles. As seen in these images, nickel nanoparticles were encapsulated by several outer layers. Interplanar spacing measured between these layers derived from the digital diffractogram (FFT image obtained with ImageJ software) was 0.33 nm which is in well agreement with the value reported for graphite in the literature (0.3347 nm, ICSD #031829). Also, lattice fringe separation inside the core yielded a value of 0.204 nm. This value is in agreement with the reported interplanar distance for (111) plane of Ni, which is 0.2041 nm (NIST #23929). Thus carbon encapsulated Ni particles were successfully synthesized where Ni particles of 5-200 nm in size were covered by 3-9 graphitic layers.

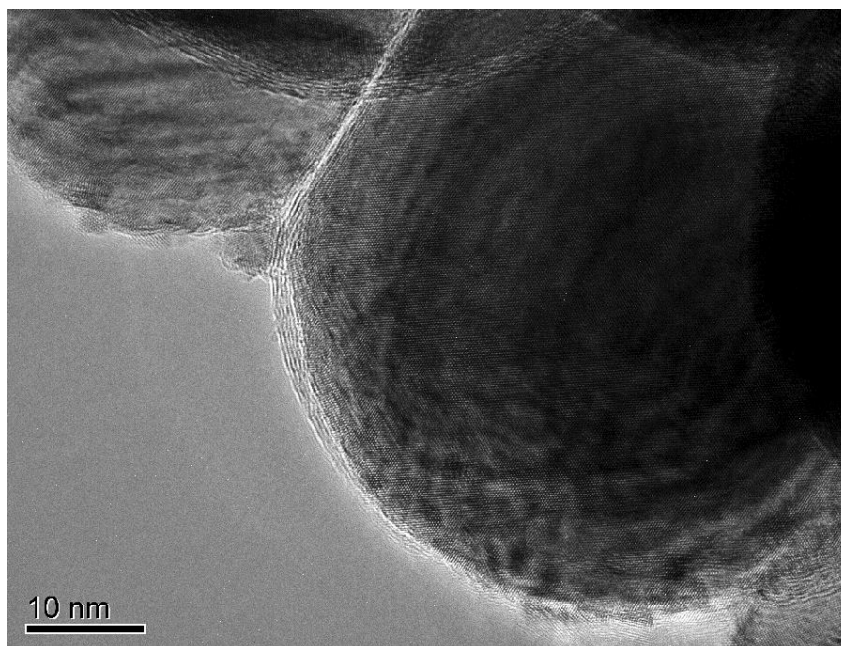


Figure 4.3 Carbon encapsulated nickel nanoparticles synthesized using top injector for nickel and bottom injector for methane feeding.

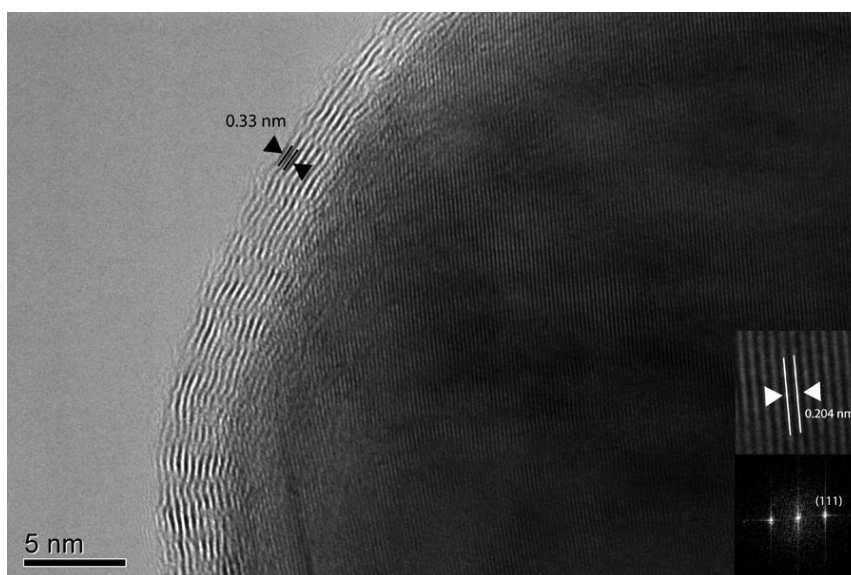


Figure 4.4 HR-TEM image of a nickel nanoparticle covered with 7-9 graphitic layers. Graphite shell ($d_{002} = 0.3347$ nm, ICSD #031829) and nickel core ($d_{111} = 0.2041$ nm, NIST #23929). Insets show a close-up image from the core and also its FFT image.

As pointed out, free carbon (not reacted with metals) as well as non-encapsulated nanopowders were also present in the sample. The diameter of particles was 56 nm with a standard deviation of 35 nm (measured over 35 particles). These values together with TEM images (Figure 4.3 and 4.4) refer to the case where Ni was fed from the top and methane was fed from the bottom injector. Similar observations were made for the case of reverse feeding. Figure 4.6 and 4.7 refer to encapsulated particles obtained from the reverse feeding configuration.

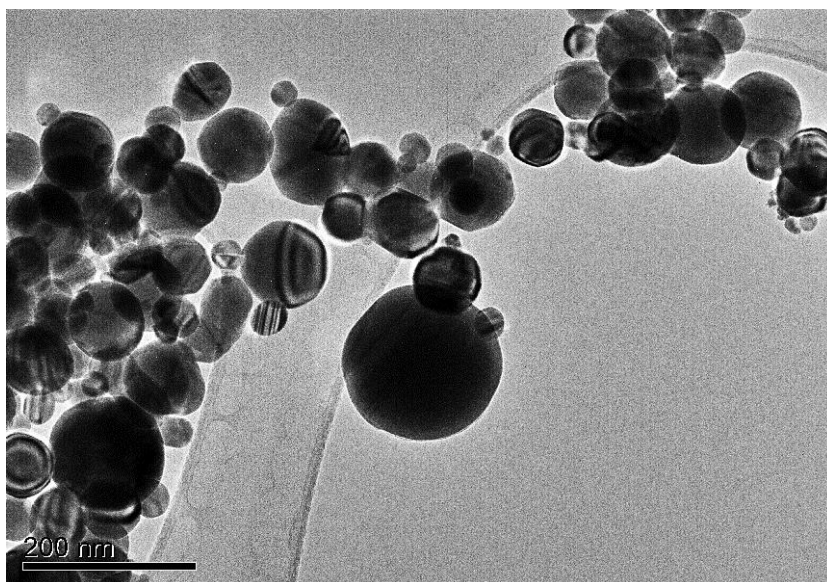


Figure 4.5 TEM image of nanoparticles synthesized using Ni and methane precursors.

The current results verify that Ni is a suitable metal for the carbon encapsulation. It does not form stable carbide and it is expected to show catalytic activity towards the graphitic layer formation on its surface (Fernández *et al.* 2009). The experiments reported have shown that both injector positions are suitable for the encapsulation of Ni particles.

It is anticipated that for the formation of encapsulated Ni particles, the use of separate injectors probably is not needed. Feeding both precursors using the same probe would again provide the suitable conditions for the encapsulation.

It should be mentioned that the average particle size obtained in encapsulation was approximately 56 nm. This value should be compared with 80 nm which was the average particle size obtained with Ni without the use of methane. Therefore, it can be concluded that carbon encapsulation also hinders the further particle growth by confining the particles within carbon layers resulting in finer particle size.

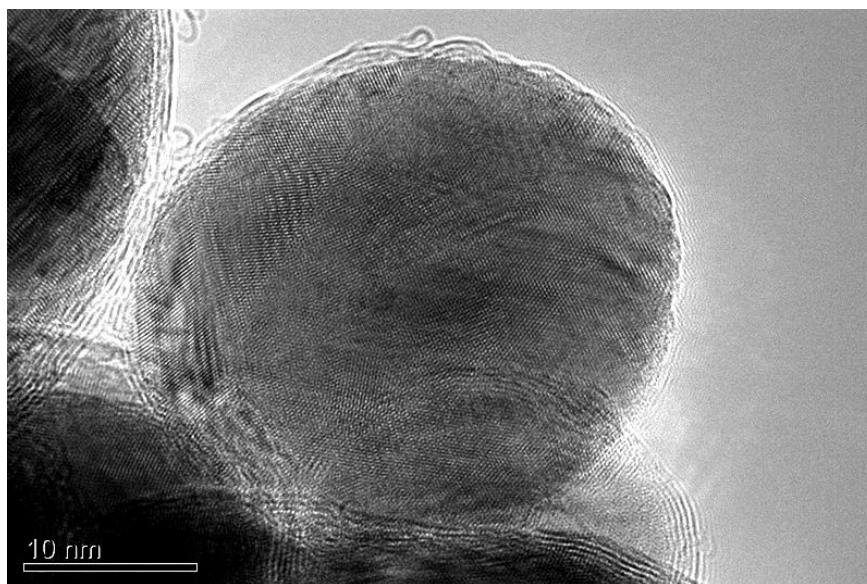


Figure 4.6 TEM image of carbon encapsulated nickel nanoparticles synthesized using top injector for methane and bottom injector for Ni feeding.

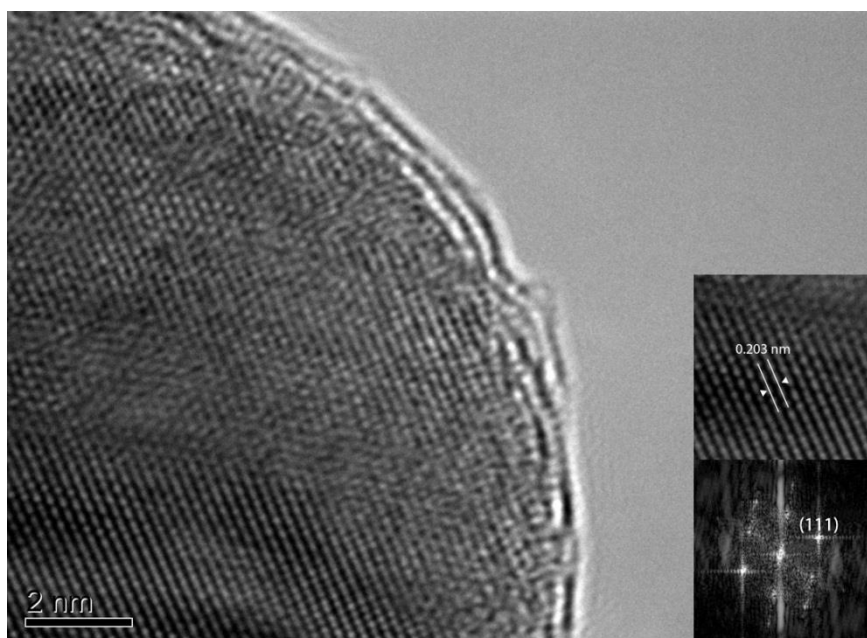


Figure 4.7 HR-TEM image of a Ni nanoparticle covered with 2-3 graphitic layers, these encapsulating layers have discontinuities as seen in the figure. Insets show a close-up image from the core and also its FFT image.

4.3.2 Encapsulation of Magnesium Nanoparticles

In the first experiment, Mg was injected with a rate of 0.25 g/min and methane with a flow rate of 1 slpm. X-ray diffractogram of particles collected from powder collector is given in Figure 4.8. This showed that the sample was largely made up of graphitic structure, no carbide phase was present. Mg (ICSD# 076259) was observed together with Mg(OH)₂ (ICDD# 7-0239) and MgO (ICDD# 45-0946).

Main carbon peak was at 25.9° (2θ). This angle should be compared with 26.6° (ICSD# 031829) of (002) plane of graphite. The current shift towards higher d-spacing values was observed in all XRD patterns reported below and implies that graphitic material is the so-called turbostratic carbon. Measured d-spacing for (002) was 0.3435 nm. Increased d-spacing is usually assigned to curved and imperfect stacking of the graphitic structure (Li *et al.* 2007).

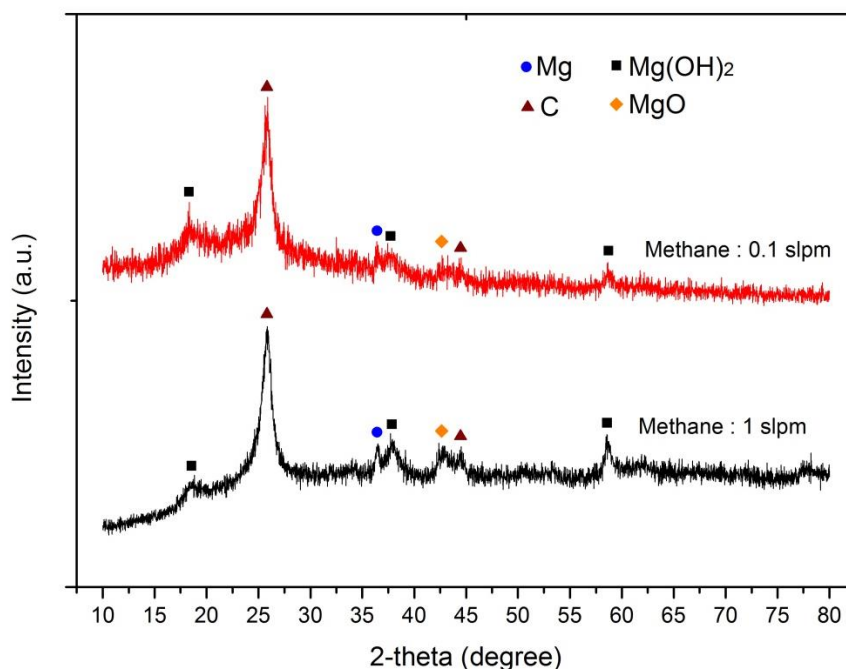


Figure 4.8 XRD patterns of powders synthesized by feeding Mg (0.25 g/min) and methane (1 slpm or 0.1 slpm) using the top injector.

As a check, a separate run was made in which only methane was fed through bottom probe. XRD pattern of the resulting powder is shown in Figure 4.9. It is seen that this pattern comprises graphite peaks at the same locations as those observed in the previous pattern. There were peaks belonging to Ni which probably originated from the

contamination of the system from the earlier experiments. But the pattern does contain additional peaks. These peaks were quite strong, actually stronger than those of graphite. These additional peaks were consistent with diamond like carbon (ICSD #067787). This f.c.c. carbon had previously been reported, e.g. Frenklach *et al.* (1989), in carbon products synthesized by plasma methods. It is also interesting that this f.c.c. carbon did not form in the previous experiment when methane was fed with Mg.

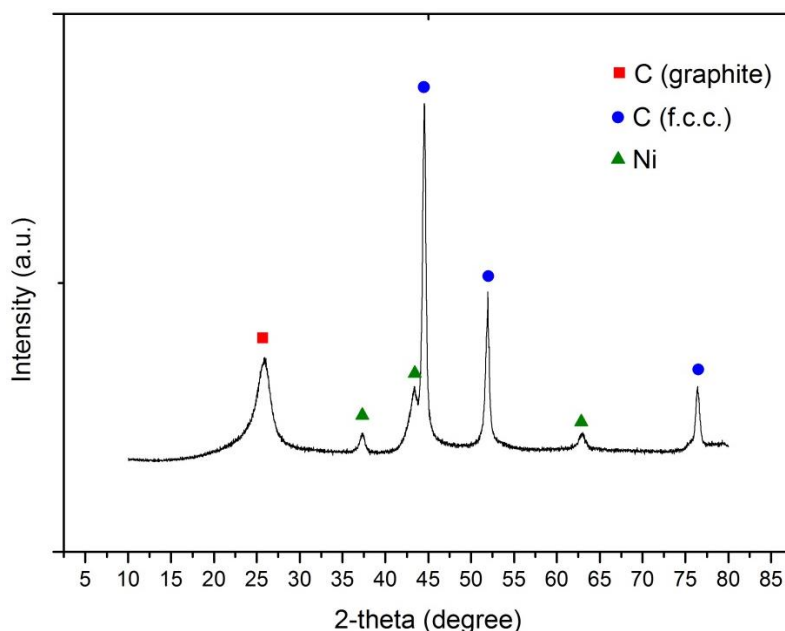


Figure 4.9 XRD pattern of powders synthesized by feeding only methane through the top injector.

TEM observations made on powders obtained from Mg and methane were consistent with XRD pattern. Thus the greater portion of the sample was graphitic, an example of which is given in Figure 4.10. Since the greater portion of the sample was graphitic, it was difficult to locate metallic particles. Figure 4.11 gives a high resolution TEM image of a particle that was encountered within the graphitic matrix. The particle displays an onion like shell. Here the lattice fringe separation derived from the FFT image of the particle core was 0.198 nm which is close to the value of (102) interplanar spacing of Mg (0.190 nm, ICSD #076259). The onion like shells around the Mg particle had a separation between them measured to be 0.334 nm, indicating that these are graphitic layers ($d_{002} = 0.3347$ nm, ICSD #031829). This particle was embedded in carbonaceous matrix and as such was not like Ni particles which occurred as individual particles wrapped around with graphitic layers.

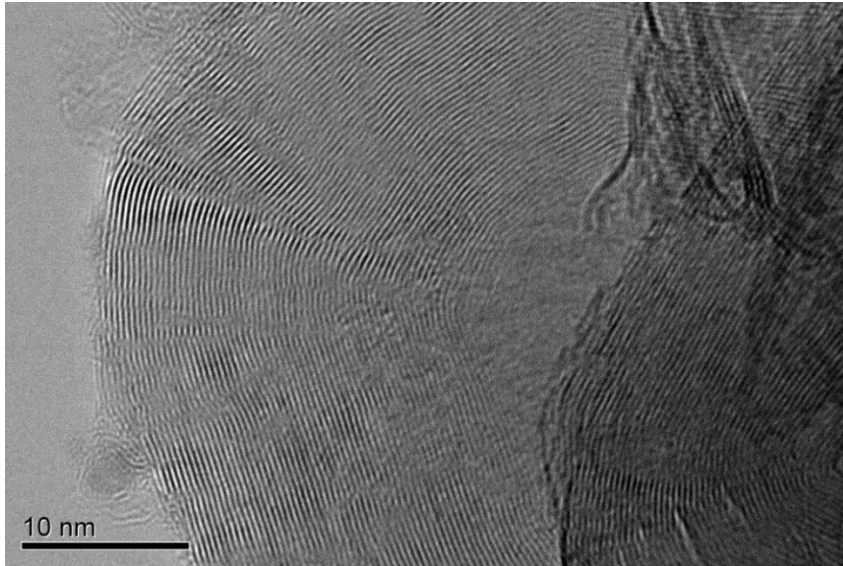


Figure 4.10 HR-TEM image of crystalline carbon structures.

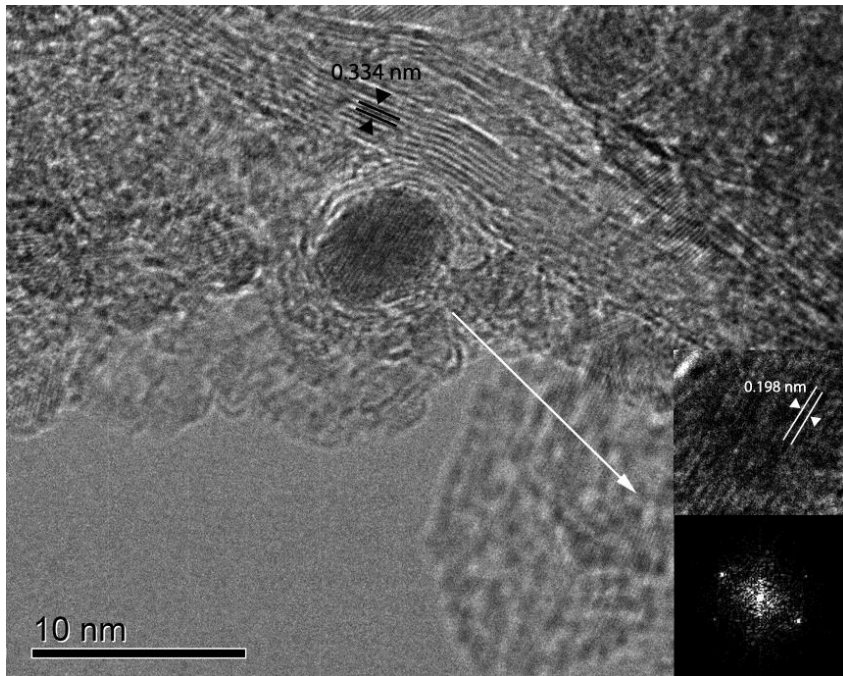


Figure 4.11 TEM image of a single Mg nanoparticle encapsulated by several graphitic layers. Insets show a close-up image from the particle and its FFT image.

With the flow rate of methane kept at 1 slpm, as reported above, the greater portion of the resulting powders were graphitic. So as to increase the metallic content, an additional experiment was carried out in which the methane flow rate was decreased to 0.1 slpm. XRD pattern of this sample is included in Figure 4.8. Here, as expected Mg bearing phases were more dominant. In TEM investigations no core-shell structure was observed, instead nanoparticles were rather small in size and were embedded in mostly carbonaceous matrix. An example of such structure is shown in Figure 4.12. Here the size of the particles is about 3-5 nm which is extremely small. Due to their small size, the lattice imaging did not lead to a conclusive result, but measured interplanar spacings were close to those of Mg.

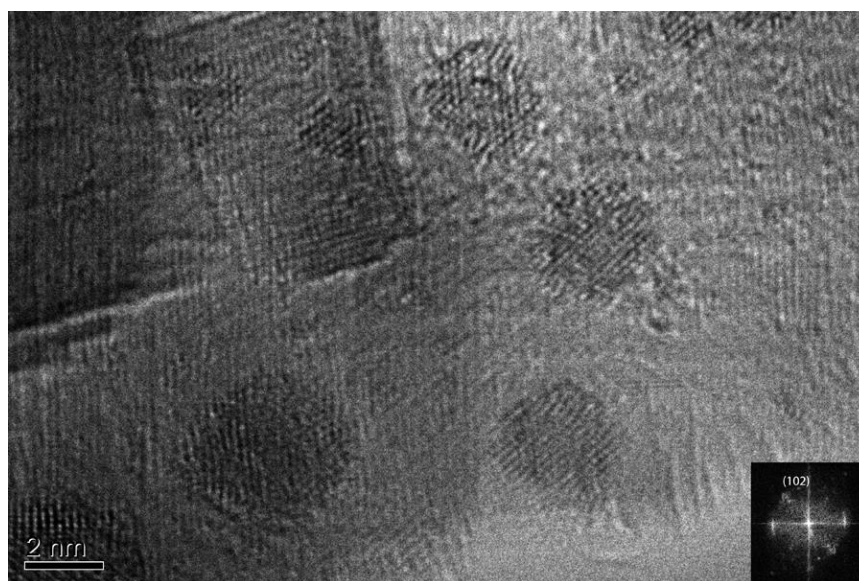


Figure 4.12 HR-TEM image of magnesium nanoparticles. Inset is the FFT image.

In the following three experiments, rather than reducing the methane feed rate, this was kept at its original value, i.e. 1 slpm, and instead Mg feed rate was increased to 0.65 g/min (from 0.25 g/min). First, Mg and methane were fed together through the top probe. XRD pattern of these powders is given in Figure 4.13. The main peaks corresponded to Mg, MgO and graphite. Where Mg and methane were fed through the separate injectors, i.e. Mg through top and methane through the bottom injector, or vice versa, the results were similar. HR-TEM images given in Figure 4.14 and 4.15 refer to these samples. Figure 4.15 shows several particles embedded in a graphitic structure. Interplanar spacings in these particles were measured as 0.242 nm, 0.211 nm and 0.148 nm using the FFT image given in the inset. These values were in agreement with the d-spacings of 0.243 nm (111), 0.211 nm (100) and 0.149 nm (220) of MgO (ICSD #044927). XRD

patterns of these powders are also given in Figure 4.13. It is seen that, relative intensities of Mg were higher compared to those of MgO in all three runs, but the difference was at its highest when Mg and methane were fed together using the top probe.

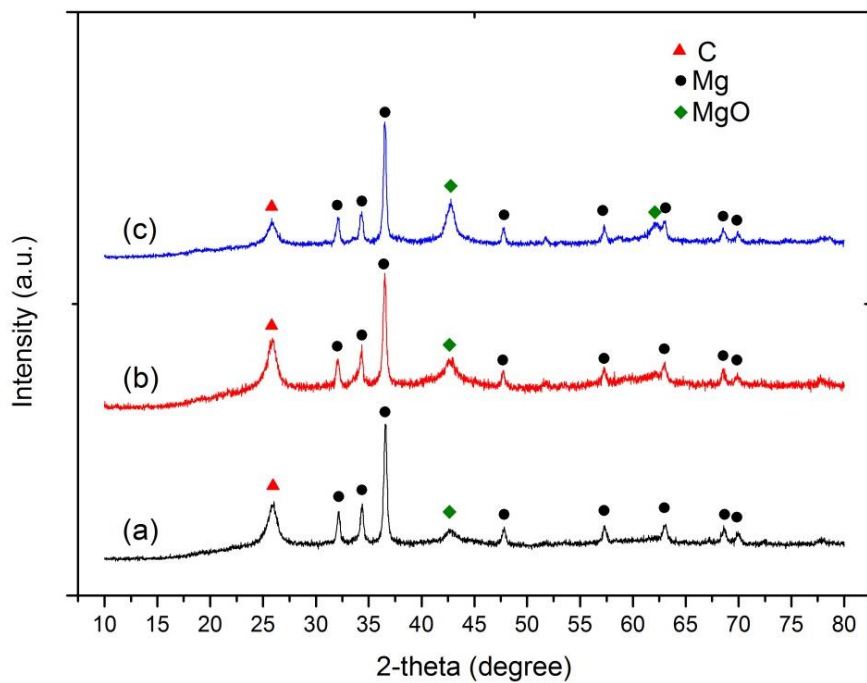


Figure 4.13 X-ray diffractograms of the powders obtained feeding (a) Mg and methane through top, (b) Mg with top and methane with bottom, (c) Mg with bottom and methane with top injector.

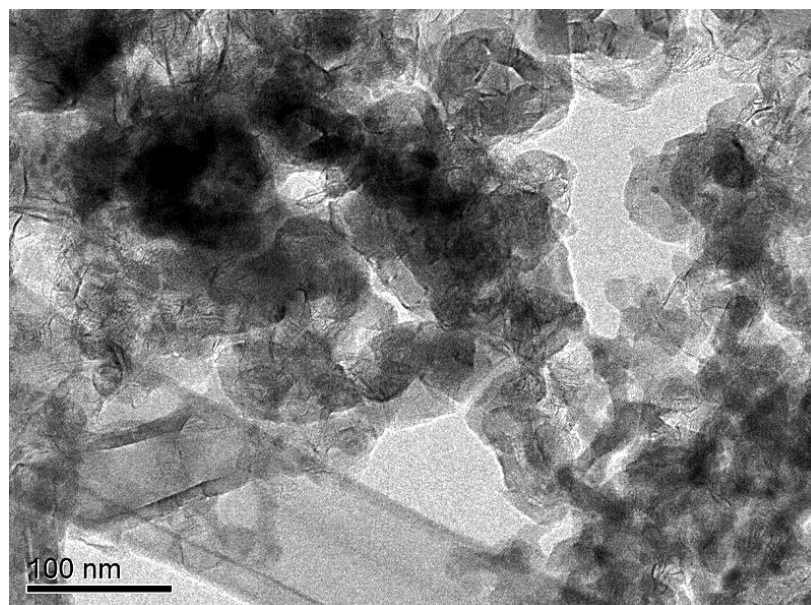


Figure 4.14 TEM image of the powders obtained using top injector (Mg) and bottom injector (methane).

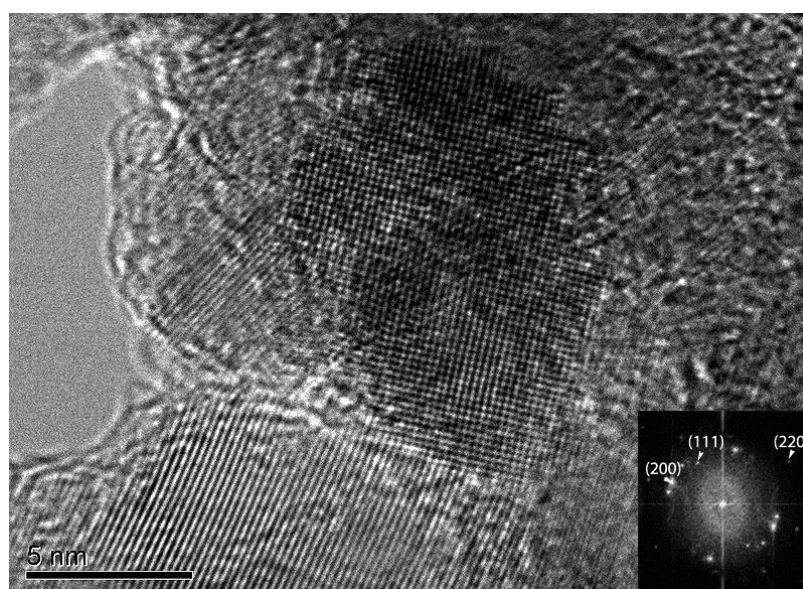


Figure 4.15 TEM image showing the presence of MgO phase in the products. Inset is the FFT image.

4.3.3 Encapsulation of Mg₂Ni Nanoparticles

Experiment with pre-alloyed Mg₂Ni powders was conducted in the same manner as that of Ni. Thus Mg₂Ni and methane were fed from the top injector with rates of 2-3 g/min and 2.5 slpm, respectively.

XRD pattern of particles collected from the powder collector is given in Figure 4.16. Here it is seen that there were no significant peaks corresponding to the Mg₂Ni phase. Instead, the pattern comprises peaks from Mg, Ni, MgO and graphite. Different from the previous experiments, there was also an additional phase. This phase appeared with peaks that were consistent with MgNi₃C as given by Bogdanovic *et al.* (1987).

Since there was no Mg₂Ni phase, encapsulated Mg₂Ni particles were not expected. TEM observations yielded carbon encapsulated nanoparticles of mainly Ni, an example of which is given in Figure 4.17. Another HR-TEM image is given in Figure 4.18. Here both Ni and MgNi₃C were observed in a single carbon encapsulated nanoparticle. Measured interplanar distances were 0.1252 nm which is agreement with the reported (220) interplanar distance of 0.125 nm for Ni (NIST# 23929) and 0.2205 nm which is in agreement with the reported (111) interplanar distance of 0.2203 nm for MgNi₃C (Bogdanovic *et al.* 1987).

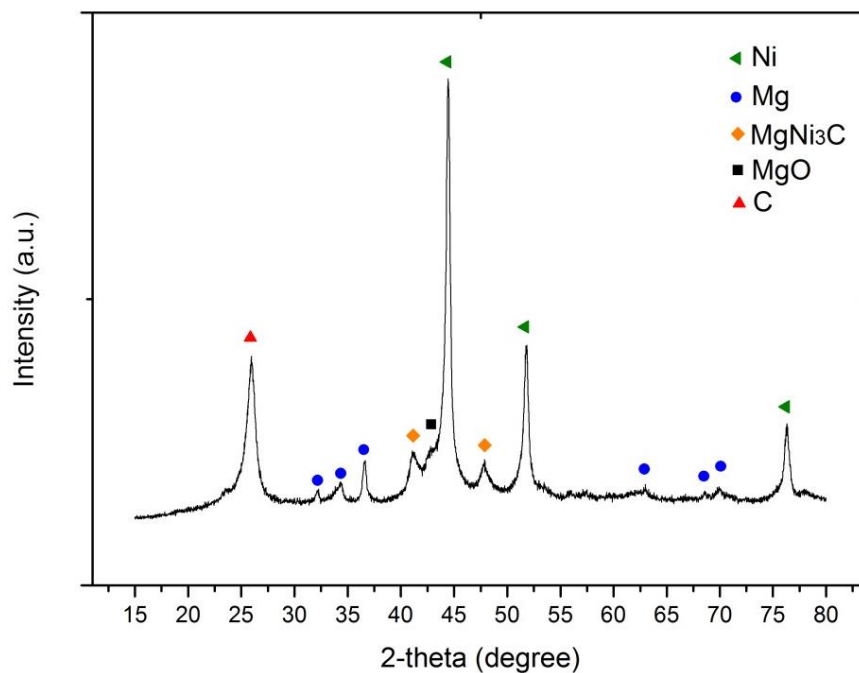


Figure 4.16 X-ray diffractogram of sample synthesized by feeding pre-alloyed Mg₂Ni with methane.

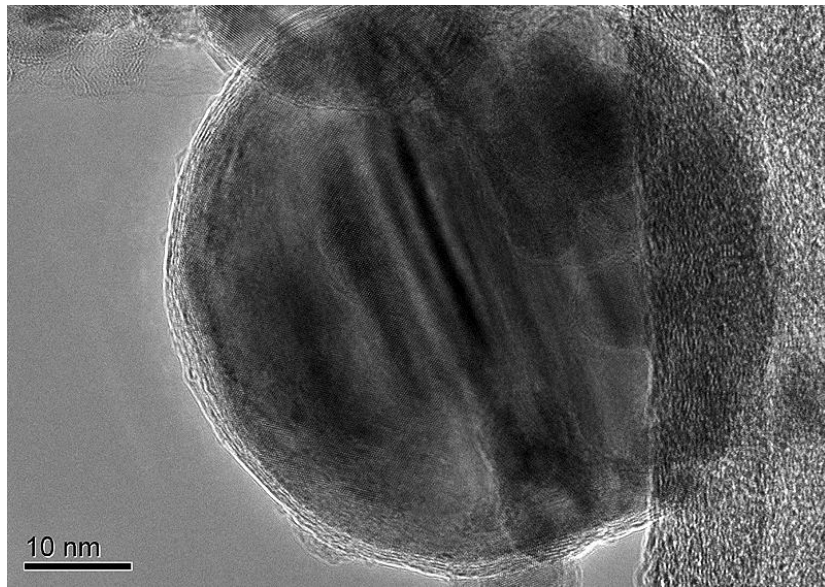


Figure 4.17 HR-TEM image of a carbon encapsulated Ni nanoparticle

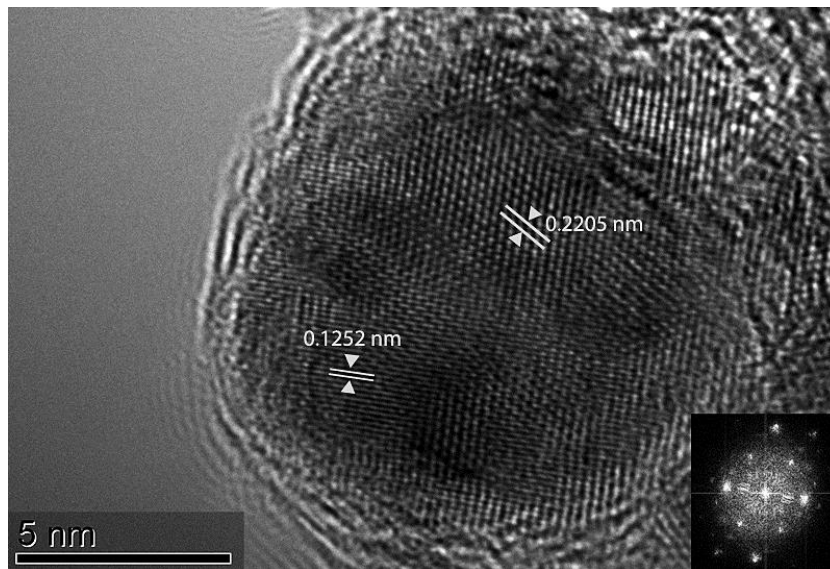


Figure 4.18 HR-TEM image of carbon encapsulated Ni and MgNi_3C .

4.4 CONCLUSIONS

In this chapter, it was shown that the induction plasma method is an effective way of synthesizing carbon encapsulated Ni nanoparticles, using methane gas as the carbon source. In addition, it was also shown that, it was possible to obtain Mg nanoparticles embedded in carbonaceous matrix. The study also showed that with the presence of methane, nanoparticles formed were smaller in size which probably originated from the earlier enclosure of nanoparticles with graphitic material.

CHAPTER 5

GENERAL CONCLUSIONS

In this study, RF induction plasma was used for the synthesis of Mg-Ni particles less than 100 nm in size for hydrogen storage purposes. The plasma reactor incorporated two injection probes which allowed feeding of precursors to different temperature zones.

In the first part, this study aimed at the synthesis of Mg₂Ni using Mg, Ni and Mg₂Ni powder as precursor material. The followings can be concluded from this study;

- i. A considerable amount of Mg₂Ni can be synthesized via induction plasma using elemental powders rather than pre-alloyed Mg₂Ni. Feeding Ni from the top and Mg from the bottom injector was found to be the most effective feeding configuration. Mg when penetrated into too high temperature regions impedes the formation of Mg₂Ni phase. A maximum Mg₂Ni content of 55 wt% was obtained in the current study where the injector is located just below the quenching inlet yielding particles with a mean size of 90-100 nm.
- ii. The powders with 55 wt% Mg₂Ni showed enhanced reaction kinetics without the need for activation. However, despite their extremely small size, there was no significant change in the stability of their hydrides. Desorption temperature under 1 bar of hydrogen pressure was not less than 200°C.

In the second part, the study aimed at the production of carbon encapsulated Mg-Ni nanoparticles. Mg, Ni, Mg₂Ni powders were used as precursors and methane was the carbon source. The study has shown the followings;

- iii. The method of induction plasma by feeding Ni together with methane can be used successfully for the synthesis of carbon encapsulated nickel nanoparticles.
- iv. Feeding methane together with Mg does not lead to the formation of individual encapsulated nanoparticles but instead leads to the formation of Mg particles embedded in graphitic structure.
- v. Feeding methane with metallic powders greatly reduces the size of the resulting particles. This size can be as small as 5 nm in the case of Mg.

However, encapsulation of Mg_2Ni was not possible since with the presence of methane there was no Mg_2Ni formation during synthesis.

REFERENCES

- Abbott, D.** (2010) Keeping the energy debate clean: How do we supply the world's energy needs? *Proceedings of the IEEE*, 98(1), 42-66.
- Akyıldız, H., & Öztürk, T.** (2010). Hydrogen sorption in crystalline and amorphous Mg–Cu thin films. *Journal of Alloys and Compounds*, 492(1), 745-750.
- Aminorroaya, S., Ranjbar, A., Cho, Y., Liu, H. K., & Dahle, A. K.** (2011). Hydrogen storage properties of mg-10 wt% ni alloy co-catalysed with niobium and multi-walled carbon nanotubes. *International Journal of Hydrogen Energy*, 36(1), 571-579.
- Andreasen, A.** (2004). *Predicting formation enthalpies of metal hydrides*.
- Athanassiou, E. K., Grass, R. N., & Stark, W. J.** (2006). Large-scale production of carbon-coated copper nanoparticles for sensor applications. *Nanotechnology*, 17(6), 1668.
- Atias-Adrian, I. C., Deorsola, F., Ortigoza-Villalba, G., DeBenedetti, B., & Baricco, M.** (2011). Development of nanostructured mg2ni alloys for hydrogen storage applications. *International Journal of Hydrogen Energy*, 36(13), 7897-7901.
- Aviles, F., Cauich-Rodriguez, J., Moo-Tah, L., May-Pat, A., & Vargas-Coronado, R.** (2009). Evaluation of mild acid oxidation treatments for MWCNT functionalization. *Carbon*, 47(13), 2970-2975.
- Baba, K., Shohata, N., & Yonezawa, M.** (1989). Synthesis and properties of ultrafine AlN powder by rf plasma. *Applied Physics Letters*, 54(23), 2309-2311.
- Bai, L., Fan, J., Hu, P., Yuan, F., Li, J., & Tang, Q.** (2009). RF plasma synthesis of nickel nanopowders via hydrogen reduction of nickel hydroxide/carbonate. *Journal of Alloys and Compounds*, 481(1), 563-567.
- Bardhan, R., Ruminski, A. M., Brand, A., & Urban, J. J.** (2011). Magnesium nanocrystal-polymer composites: A new platform for designer hydrogen storage materials. *Energy & Environmental Science*, 4(12), 4882-4895.

- Bernardi, D.**, Colombo, V., Ghedini, E., & Mentrelli, A. (2003). Three-dimensional modelling of inductively coupled plasma torches. *The European Physical Journal D-Atomic, Molecular, Optical and Plasma Physics*, 22(1), 119-125.
- Bernardi, D.**, Colombo, V., Ghedini, E., & Mentrelli, A. (2003). Three-dimensional effects in the modelling of ICPTs. *The European Physical Journal D-Atomic, Molecular, Optical and Plasma Physics*, 25(3), 271-277.
- Berry, V.** (2013). Impermeability of graphene and its applications. *Carbon*.
- Bobet, J.**, Grigorova, E., Khrussanova, M., Khristov, M., Stefanov, P., Peshev, P., & Radev, D. (2004). Hydrogen sorption properties of graphite-modified magnesium nanocomposites prepared by ball-milling. *Journal of Alloys and Compounds*, 366(1), 298-302.
- Bogaerts, A.**, Neyts, E., Gijbels, R., & van der Mullen, J. (2002). Gas discharge plasmas and their applications. *Spectrochimica Acta Part B: Atomic Spectroscopy*, 57(4), 609-658.
- Bogdanović, B.**, Brand, R. A., Marjanović, A., Schwickardi, M., & Tölle, J. (2000). Metal-doped sodium aluminium hydrides as potential new hydrogen storage materials. *Journal of Alloys and Compounds*, 302(1), 36-58.
- Bogdanović, B.**, & Schwickardi, M. (1997). Ti-doped alkali metal aluminium hydrides as potential novel reversible hydrogen storage materials. *Journal of Alloys and Compounds*, 253, 1-9.
- Bonizzoni, G.**, & Vassallo, E. (2002). Plasma physics and technology; industrial applications. *Vacuum*, 64(3), 327-336.
- Borodina, T.**, Grigoriev, D., Andreeva, D., Mohwald, H., & Shchukin, D. (2009). Polyelectrolyte multilayered nanofilms as a novel approach for the protection of hydrogen storage materials. *ACS Applied Materials & Interfaces*, 1(5), 996-1001.
- Borysiuk, J.**, Grabias, A., Szczytko, J., Bystrzejewski, M., Twardowski, A., & Lange, H. (2008). Structure and magnetic properties of carbon encapsulated Fe nanoparticles obtained by arc plasma and combustion synthesis. *Carbon*, 46(13), 1693-1701.
- Bouaricha, S.**, Dodelet, J., Guay, D., Huot, J., Boily, S., & Schulz, R. (2000). Effect of carbon-containing compounds on the hydriding behavior of nanocrystalline Mg₂Ni. *Journal of Alloys and Compounds*, 307(1), 226-233.

- Boulos, M.** (2011). Induction plasma processing of materials for powders, coatings, and near-net-shape parts. *Advanced Materials & Processes*, 169(8), 52-53.
- Boulos, M. I.** (1985). The inductively coupled RF (radio frequency) plasma. *Pure&Appl. Chem.*, Vol. 57, No. 9, pp. 1321—1352.
- Boulos, M. I.** (1991). Thermal plasma processing. *Plasma Science, IEEE Transactions on*, 19(6), 1078-1089. doi:10.1109/27.125032
- Bunch, J. S.,** Verbridge, S. S., Alden, J. S., van der Zande, Arend M, Parpia, J. M., Craighead, H. G., & McEuen, P. L. (2008). Impermeable atomic membranes from graphene sheets. *Nano Letters*, 8(8), 2458-2462.
- Bystrzejewski, M.,** Huczko, A., Lange, H., Baranowski, P., Cota-Sanchez, G., Soucy, G., Twardowski, A. (2007). Large scale continuous synthesis of carbon-encapsulated magnetic nanoparticles. *Nanotechnology*, 18(14), 145608.
- Bystrzejewski, M.,** Károly, Z., Szépvölgyi, J., Huczko, A., & Lange, H. (2011). Continuous synthesis of controlled size carbon-encapsulated iron nanoparticles. *Materials Research Bulletin*, 46(12), 2408-2417.
- Bystrzejewski, M.,** Cudziło, S., Huczko, A., Lange, H., Soucy, G., Cota-Sanchez, G., & Kaszuwara, W. (2007). Carbon encapsulated magnetic nanoparticles for biomedical applications: Thermal stability studies. *Biomolecular Engineering*, 24(5), 555-558.
- Bystrzejewski, M.,** Huczko, A., & Lange, H. (2005). Arc plasma route to carbon-encapsulated magnetic nanoparticles for biomedical applications. *Sensors and Actuators B: Chemical*, 109(1), 81-85.
- Çakmak, G.,** Károly, Z., Mohai, I., Öztürk, T., & Szépvölgyi, J. (2010). The processing of Mg–Ti for hydrogen storage; mechanical milling and plasma synthesis. *International Journal of Hydrogen Energy*, 35(19), 10412-10418.
- Cermak, J., & Kral, L.** (2012). Alloying of Mg/Mg₂Ni eutectic by chosen non-hydride forming elements: Relation between segregation of the third element and hydride storage capacity. *Journal of Power Sources*, 197, 116-120.
- Chen, I.,** Chen, L., Gapin, A., Jin, S., Yuan, L., & Liou, S. (2008). Iron–platinum-coated carbon nanocone probes on tipless cantilevers for high resolution magnetic force imaging. *Nanotechnology*, 19(7), 075501.

- Cheng, Y.,** Shigeta, M., Choi, S., & Watanabe, T. (2012). Formation mechanism of titanium boride nanoparticles by RF induction thermal plasma. *Chemical Engineering Journal*, 183, 483-491.
- Cheng, Y., & Watanabe, T.** (2011). Synthesis of titanium boride nanoparticles by induction thermal plasmas. *Journal of Chemical Engineering of Japan*, (0), 1105190203.
- Colombo, V.,** Deschenaux, C., Ghedini, E., Gherardi, M., Jaeggi, C., Leparoux, M., Sanibondi, P. (2012). Fluid-dynamic characterization of a radio-frequency induction thermal plasma system for nanoparticle synthesis. *Plasma Sources Science and Technology*, 21(4), 045010.
- Colombo, V.,** Ghedini, E., & Sanibondi, P. (2010). Three-dimensional investigation of particle treatment in an RF thermal plasma with reaction chamber. *Plasma Sources Science & Technology*, 19(6)
- Cota-Sanchez, G.,** Soucy, G., Huczko, A., & Lange, H. (2005). Induction plasma synthesis of fullerenes and nanotubes using carbon black–nickel particles. *Carbon*, 43(15), 3153-3166.
- Cota-Sanchez, G.,** Soucy, G., Huczko, A., & Lange, H. (2005). Induction plasma synthesis of fullerenes and nanotubes using carbon black–nickel particles. *Carbon*, 43(15), 3153-3166.
- Datsyuk, V.,** Kalyva, M., Papagelis, K., Parthenios, J., Tasis, D., Siokou, A., Galiotis, C. (2008). Chemical oxidation of multiwalled carbon nanotubes. *Carbon*, 46(6), 833-840.
- Ding, H.,** Zhang, S., Zhang, Y., Huang, S., Wang, P., & Tian, H. (2012). Effects of nonmetal element (B, C and Si) additives in Mg₂Ni hydrogen storage alloy: A first-principles study. *International Journal of Hydrogen Energy*, 37(8), 6700-6713.
- Dong, X.,** Zhang, Z., Jin, S., & Kim, B. (1999). Carbon-coated Fe–Co (C) nanocapsules prepared by arc discharge in methane. *Journal of Applied Physics*, 86(12), 6701-6706.
- Du, H.,** Li, J., Zhang, J., Su, G., Li, X., & Zhao, Y. (2011). Separation of hydrogen and nitrogen gases with porous graphene membrane. *The Journal of Physical Chemistry C*, 115(47), 23261-23266.

- Eliasson, B., & Kogelschatz, U.** (1991). Nonequilibrium volume plasma chemical processing. *Plasma Science, IEEE Transactions on*, 19(6), 1063-1077.
- Elliott, B.,** Host, J., Dravid, V., Teng, M., & Hwang, J. (1997). A descriptive model linking possible formation mechanisms for graphite-encapsulated nanocrystals to processing parameters. *Journal of Materials Research*, 12(12), 3328-3344.
- Esawi, A. M., & El Borady, M. A.** (2008). Carbon nanotube-reinforced aluminium strips. *Composites Science and Technology*, 68(2), 486-492.
- Fan, X.,** Ishigaki, T., & Sato, Y. (1997). Phase formation in molybdenum disilicide powders during in-flight induction plasma treatment. *Journal of Materials Research*, 12(5), 1315-1326.
- Fernandez, Y.,** Menendez, J., Phillips, J., & Luhrs, C. (2009). Graphitic encapsulation of micron-and nano-sized ni particles using ethylene as precursor. *Applied Surface Science*, 256(1), 194-201.
- German, R. M.** (2005). *Powder metallurgy & particulate materials processing* Metal powder industries federation Princeton, NJ.
- Ghoniem, A. F.** (2011). Needs, resources and climate change: Clean and efficient conversion technologies. *Progress in Energy and Combustion Science*, 37(1), 15-51.
- Girshick, S.,** Chiu, C., & McMurry, P. (1990). Time-dependent aerosol models and homogeneous nucleation rates. *Aerosol Science and Technology*, 13(4), 465-477.
- Gonzalez, N. Y. M.,** El Morsli, M., & Proulx, P. (2008). Production of nanoparticles in thermal plasmas: A model including evaporation, nucleation, condensation, and fractal aggregation. *Journal of Thermal Spray Technology*, 17(4), 533-550.
- Guo, J.,** Gitzhofer, F., & Boulos, M. (1997). Effects of process parameters on ultrafine SiC synthesis using induction plasmas. *Plasma Chemistry and Plasma Processing*, 17(2), 219-249.
- Guray, A.,** Kudas, T., Pluym, T., & Xiong, Y. (1993). Aerosol processing of materials. *Aerosol Science and Technology*, 19(4), 411-452.
- Güvendiren, M.,** Baybörü, E., & Öztürk, T. (2004). Effects of additives on mechanical milling and hydrogenation of magnesium powders. *International Journal of Hydrogen Energy*, 29(5), 491-496.

- Henne, R.** (1999). Thermal plasmas for material processing. *Contributions to Plasma Physics*, 39(5), 385-397. doi:10.1002/ctpp.2150390503
- Hopwood, J.** (1992). Review of inductively coupled plasmas for plasma processing. *Plasma Sources Science and Technology*, 1(2), 109.
- Hsu, C., Lee, S., Jeng, R., & Lin, J.** (2007). Mass production of Mg₂Ni alloy bulk by isothermal evaporation casting process. *International Journal of Hydrogen Energy*, 32(18), 4907-4911.
- Ichikawa, T., Isobe, S., Hanada, N., & Fujii, H.** (2004). Lithium nitride for reversible hydrogen storage. *Journal of Alloys and Compounds*, 365(1), 271-276.
- Ishigaki, T., & Li, J.** (2007). Synthesis of functional nanocrystallites through reactive thermal plasma processing. *Science and Technology of Advanced Materials*, 8(7), 617-623.
- Jain, I., Lal, C., & Jain, A.** (2010). Hydrogen storage in mg: A most promising material. *International Journal of Hydrogen Energy*, 35(10), 5133-5144.
- Janot, R., Aymard, L., Rougier, A., Nazri, G., & Tarascon, J.** (2004). Fast hydrogen sorption kinetics for ball-milled mg₂ni alloys. *Journal of Physics and Chemistry of Solids*, 65(2), 529-534.
- Jeon, K., Moon, H. R., Ruminski, A. M., Jiang, B., Kisielowski, C., Bardhan, R., & Urban, J. J.** (2011). Air-stable magnesium nanocomposites provide rapid and high-capacity hydrogen storage without using heavy-metal catalysts. *Nature Materials*, 10(4), 286-290.
- Jiang, D., Cooper, V. R., & Dai, S.** (2009). Porous graphene as the ultimate membrane for gas separation. *Nano Letters*, 9(12), 4019-4024.
- Jiang, H., & Xu, Q.** (2011). Catalytic hydrolysis of ammonia borane for chemical hydrogen storage. *Catalysis Today*, 170(1), 56-63.
- Jiao, J., & Seraphin, S.** (1998). Carbon encapsulated nanoparticles of ni, co, cu, and ti. *Journal of Applied Physics*, 83(5), 2442-2448.
- Jiayin, G., Xiaobao, F., Dolbec, R., Siwen, X., Jurewicz, J., & Boulos, M.** (2010). Development of nanopowder synthesis using induction plasma. *Plasma Science and Technology*, 12(2), 188.

- Jiayin, G.**, Xiaobao, F., Dolbec, R., Siwen, X., Jurewicz, J., & Boulos, M. (2010). Development of nanopowder synthesis using induction plasma. *Plasma Science and Technology*, 12(2), 188.
- Jongh, P. E. d.**, Wagemans, R. W., Eggenhuisen, T. M., Dauvillier, B. S., Radstake, P. B., Meeldijk, J. D., Jong, K. P. d. (2007). The preparation of carbon-supported magnesium nanoparticles using melt infiltration. *Chemistry of Materials*, 19(24), 6052-6057.
- Károly, Z.**, Mohai, I., Klébert, S., Keszler, A., Sajó, I., & Szépvölgyi, J. (2011). Synthesis of SiC powder by RF plasma technique. *Powder Technology*, 214(3), 300-305.
- Kim, K. S.**, Cota-Sanchez, G., Kingston, C. T., Imris, M., Simard, B., & Soucy, G. (2007). Large-scale production of single-walled carbon nanotubes by induction thermal plasma. *Journal of Physics D: Applied Physics*, 40(8), 2375.
- Kim, K.**, Moradian, A., Mostaghimi, J., & Soucy, G. (2010). Modeling of induction plasma process for fullerene synthesis: Effect of plasma gas composition and operating pressure. *Plasma Chemistry and Plasma Processing*, 30(1), 91-110.
- Ko, S.**, Koo, S., Cho, W., Hwnag, K., & Kim, J. (2012). Synthesis of SiC nano-powder from organic precursors using RF inductively coupled thermal plasma. *Ceramics International*, 38(3), 1959-1963.
- Kobayashi, N.**, Ishigaki, T., Watanabe, T., & Li, J. (2011). Synthesis of pure, crystalline (ba, sr) TiO₃ nanosized powders in radio frequency induction thermal plasma. *International Journal of Applied Ceramic Technology*, 8(5), 1125-1135.
- Kobayashi, N.**, Kawakami, Y., Kamada, K., Li, J., Ye, R., Watanabe, T., & Ishigaki, T. (2008). Spherical submicron-size copper powders coagulated from a vapor phase in RF induction thermal plasma. *Thin Solid Films*, 516(13), 4402-4406.
- Kodera, Y.**, Yamasaki, N., Yamamoto, T., Kawasaki, T., Ohyanagi, M., & Munir, Z. A. (2007). Hydrogen storage mg₂ni alloy produced by induction field activated combustion synthesis. *Journal of Alloys and Compounds*, 446, 138-141.
- Kogelschatz, U.** (2004). Atmospheric-pressure plasma technology. *Plasma Physics and Controlled Fusion*, 46(12B), B63.

- Lee, M.,** Kim, J., & Seo, J. (2012). Radio-frequency thermal plasma synthesis of nano-sized indium zinc tin oxide powders with reduced indium content. *Thin Solid Films*, 521, 60-64.
- Leparoux, M.,** Leconte, Y., Wirth, A., & Buehler, T. (2010). In situ treatment of thermal RF plasma processed nanopowders to control their agglomeration and dispersability. *Plasma Chemistry and Plasma Processing*, 30(6), 779-793.
- Li, J.,** Ikeda, M., Ye, R., Moriyoshi, Y., & Ishigaki, T. (2007). Control of particle size and phase formation of TiO₂ nanoparticles synthesized in RF induction plasma. *Journal of Physics D: Applied Physics*, 40(8), 2348.
- Li, Q.,** Lin, Q., Jiang, L., Chou, K., Zhan, F., & Zheng, Q. (2004). Characteristics of hydrogen storage alloy Mg₂Ni produced by hydriding combustion synthesis. *Journal of Materials Science and Technology-Shenyang-*, 20(2), 209-212.
- Li, Z. Q.,** et al. "X-ray diffraction patterns of graphite and turbostratic carbon." *Carbon* 45.8 (2007): 1686-1695.
- Li, W.,** Li, C., Ma, H., & Chen, J. (2007). Magnesium nanowires: Enhanced kinetics for hydrogen absorption and desorption. *Journal of the American Chemical Society*, 129(21), 6710-6711.
- Liang, G.,** Boily, S., Huot, J., Van Neste, A., & Schulz, R. (1998). Mechanical alloying and hydrogen absorption properties of the Mg–Ni system. *Journal of Alloys and Compounds*, 267(1), 302-306.
- Liang, G.,** Huot, J., Boily, S., Van Neste, A., & Schulz, R. (1999). Hydrogen storage properties of the mechanically milled MgH₂V nanocomposite. *Journal of Alloys and Compounds*, 291(1), 295-299.
- Liu, T.,** Qin, C., Zhang, T., Cao, Y., Zhu, M., & Li, X. (2012). Synthesis of mg@Mg₁₇Al₁₂ ultrafine particles with superior hydrogen storage properties by hydrogen plasma–metal reaction. *Journal of Materials Chemistry*, 22(37), 19831-19838.
- Liu, X.,** Zhu, Y., & Li, L. (2007). Hydriding characteristics of Mg₂Ni prepared by mechanical milling of the product of hydriding combustion synthesis. *International Journal of Hydrogen Energy*, 32(13), 2450-2454.
- Mandal, T., & Gregory, D.** (2010). Hydrogen: A future energy vector for sustainable development. *Proceedings of the Institution of Mechanical Engineers, Part C: Journal of Mechanical Engineering Science*, 224(3), 539-558.

- Mendoza-Gonzalez, N.,** Proulx, P., & Goortani, B. (2006). Numerical study of the synthesis of nanoparticles in an inductively coupled plasma reactor. *Czechoslovak Journal of Physics*, 56(2), B1263-B1270.
- Metin, O., & Ozkar, S.** (2009). Hydrogen generation from the hydrolysis of ammonia-borane and sodium borohydride using water-soluble polymer-stabilized cobalt (0) nanoclusters catalyst. *Energy & Fuels*, 23(7), 3517-3526.
- Mohai, I.,** Gál, L., Szépvölgyi, J., Gubicza, J., & Farkas, Z. (2007). Synthesis of nanosized zinc ferrites from liquid precursors in RF thermal plasma reactor. *Journal of the European Ceramic Society*, 27(2), 941-945.
- Mostaghimi, J.,** Proulx, P., & Boulos, M. I. (1984). Parametric study of the flow and temperature fields in an inductively coupled rf plasma torch. *Plasma Chemistry and Plasma Processing*, 4(3), 199-217.
- Nielsen, T. K.,** Manickam, K., Hirscher, M., Besenbacher, F., & Jensen, T. R. (2009). Confinement of MgH₂ nanoclusters within nanoporous aerogel scaffold materials. *ACS Nano*, 3(11), 3521-3528.
- Nishiyama, H.,** Muro, Y., & Kamiyama, S. (1996). The control of gas temperature and velocity fields of a RF induction thermal plasma by injecting secondary gas. *Journal of Physics D: Applied Physics*, 29(10), 2634.
- Oelerich, W.,** Klassen, T., & Bormann, R. (2001). Metal oxides as catalysts for improved hydrogen sorption in nanocrystalline mg-based materials. *Journal of Alloys and Compounds*, 315(1), 237-242.
- Ono, S.,** Ishido, Y., Imanari, K., Tabata, T., Cho, Y. K., Yamamoto, R., & Doyama, M. (1982). Phase transformation and thermal expansion of MgNi alloys in a hydrogen atmosphere. *Journal of the Less-Common Metals*, 88(1), 57-61.
- Orimo, S.,** Fujii, H., & Ikeda, K. (1997). Notable hydriding properties of a nanostructured composite material of the mg₂ni-H system synthesized by reactive mechanical grinding. *Acta Materialia*, 45(1), 331-341.
- Orimo, S.,** Nakamori, Y., Eliseo, J. R., Züttel, A., & Jensen, C. M. (2007). Complex hydrides for hydrogen storage. *Chemical Reviews*, 107(10), 4111-4132.

- Pristavita, R.,** Mendoza-Gonzalez, N., Meunier, J., & Berk, D. (2011). Carbon nanoparticle production by inductively coupled thermal plasmas: Controlling the thermal history of particle nucleation. *Plasma Chemistry and Plasma Processing*, 31(6), 851-866.
- Punjabi, S. B.,** Joshi, N., Mangalvedekar, H., Lande, B., Das, A., & Kothari, D. (2012). A comprehensive study of different gases in inductively coupled plasma torch operating at one atmosphere. *Physics of Plasmas*, 19, 012108.
- Pyrzynska, K.** (2010). Carbon nanostructures for separation, preconcentration and speciation of metal ions. *TrAC Trends in Analytical Chemistry*, 29(7), 718-727.
- Reed, T. B.** (1961). Induction-Coupled plasma torch. *Journal of Applied Physics*, 32(5), 821-824.
- Reilly Jr, J. J., & Wiswall Jr, R. H.** (1968). Reaction of hydrogen with alloys of magnesium and nickel and the formation of Mg₂NiH₄. *Inorganic Chemistry*, 7(11), 2254-2256.
- Ross, D. A.** (1991). *Plasma Torch with Axial Reactant Feed*, U.S. Patent No. 5,008,511. 16 Apr. 1991.
- Saito, Y.,** Yoshikawa, T., Okuda, M., Fujimoto, N., Sumiyama, K., Suzuki, K., Nishina, Y. (1993). Carbon nanocapsules encaging metals and carbides. *Journal of Physics and Chemistry of Solids*, 54(12), 1849-1860
- Sakintuna, B.,** Lamari-Darkrim, F., & Hirscher, M. (2007). Metal hydride materials for solid hydrogen storage: A review. *International Journal of Hydrogen Energy*, 32(9), 1121-1140.
- Santos, D., & Sequeira, C.** (2011). Sodium borohydride as a fuel for the future. *Renewable and Sustainable Energy Reviews*, 15(8), 3980-4001.
- Schlapbach, L., & Züttel, A.** (2001). Hydrogen-storage materials for mobile applications. *Nature*, 414(6861), 353-358.
- Scott, J. H. J.,** Turgut, Z., Chowdary, K., Mchenry, M. E., & Majetich, S. A. (1997). Thermal plasma synthesis of fe-co alloy nanoparticles. *MRS Proceedings*, , 501(1)
- Seo, J., & Hong, B.** (2012). Thermal plasma synthesis of nano-sized powders. *Nuclear Eng Technol*, 44(1), 9-20.

- Seraphin, S.** (1995). Single-Walled tubes and encapsulation of nanocrystals into carbon clusters. *Journal of the Electrochemical Society*, 142(1), 290-297.
- Shao, H.,** Xu, H., Wang, Y., & Li, X. (2004). Preparation and hydrogen storage properties of Mg₂Ni intermetallic nanoparticles. *Nanotechnology*, 15(3), 269.
- Shigeta, M., & Watanabe, T.** (2007). Growth mechanism of silicon-based functional nanoparticles fabricated by inductively coupled thermal plasmas. *Journal of Physics D: Applied Physics*, 40(8), 2407.
- Shigeta, M., & Watanabe, T.** (2008). Two-dimensional analysis of nanoparticle formation in induction thermal plasmas with counterflow cooling. *Thin Solid Films*, 516(13), 4415-4422.
- Shigeta, M., & Watanabe, T.** (2009). Two-directional nodal model for co-condensation growth of multicomponent nanoparticles in thermal plasma processing. *Journal of Thermal Spray Technology*, 18(5-6), 1022-1037.
- Shigeta, M., & Watanabe, T.** (2010). Growth model of binary alloy nanopowders for thermal plasma synthesis. *Journal of Applied Physics*, 108(4), 043306-043306-15.
- Shin, J.,** Miyazoe, H., Leparoux, M., Siegmann, S., Dorier, J., & Hollenstein, C. (2006). The influence of process parameters on precursor evaporation for alumina nanopowder synthesis in an inductively coupled rf thermal plasma. *Plasma Sources Science and Technology*, 15(3), 441.
- Si, T., Liu, D., & Zhang, Q.** (2007). Microstructure and hydrogen storage properties of the laser sintered Mg₂Ni alloy. *International Journal of Hydrogen Energy*, 32(18), 4912-4916.
- Siegel, R.** (1994). Nanophase materials: Synthesis, structure, and properties. *Physics of new materials* (pp. 65-105) Springer.
- Son, S.,** Swaminathan, R., & McHenry, M. (2003). Structure and magnetic properties of rf thermally plasma synthesized mn and Mn–Zn ferrite nanoparticles. *Journal of Applied Physics*, 93(10), 7495-7497.
- Son, S.,** Taheri, M., Carpenter, E., Harris, V., & McHenry, M. (2002). Synthesis of ferrite and nickel ferrite nanoparticles using radio-frequency thermal plasma torch. *Journal of Applied Physics*, 91(10), 7589-7591.

- Soucy, G.,** Rahmane, M., Fan, X., & Ishigaki, T. (2001). Heat and mass transfer during in-flight nitridation of molybdenum disilicide powder in an induction plasma reactor. *Materials Science and Engineering: A*, 300(1), 226-234.
- Suh, M. P.,** Park, H. J., Prasad, T. K., & Lim, D. (2011). Hydrogen storage in metal-organic frameworks. *Chemical Reviews*, 112(2), 782-835.
- Sun, X., & Dong, X.** (2002). Magnetic properties and microstructure of carbon encapsulated ni nanoparticles and pure ni nanoparticles coated with NiO layer. *Materials Research Bulletin*, 37(5), 991-1004.
- Sun, X., & Li, Y.** (2005). Ag@ C core/shell structured nanoparticles: Controlled synthesis, characterization, and assembly. *Langmuir*, 21(13), 6019-6024.
- Suresh, K.,** Selvarajan, V., & Mohai, I. (2008). Synthesis and characterization of iron aluminide nanoparticles by DC thermal plasma jet. *Vacuum*, 82(5), 482-490.
- Szépölggyi, J.,** Mohai, I., Károly, Z., & Gál, L. (2008). Synthesis of nanosized ceramic powders in a radiofrequency thermal plasma reactor. *Journal of the European Ceramic Society*, 28(5), 895-899.
- Terrones, M.,** Hsu, W. K., Terrones, H., Zhang, J. P., Ramos, S., Hare, J. P., Walton, D. R. M. (1996). Metal particle catalysed production of nanoscale BN structures. *Chemical Physics Letters*, 259(5-6), 568-573.
- Teunissen, W.,** de Groot, F. M., Geus, J., Stephan, O., Tence, M., & Colliex, C. (2001). The structure of carbon encapsulated NiFe nanoparticles. *Journal of Catalysis*, 204(1), 169-174.
- Todorovic-Marković, B.,** Marković, Z., Mohai, I., Karoly, Z., Gal, L., Föglein, K., Szépölggyi, J. (2003). Efficient synthesis of fullerenes in RF thermal plasma reactor. *Chemical Physics Letters*, 378(3), 434-439.
- Tokoro, H.,** Fujii, S., & Oku, T. (2004). Microstructures and magnetic properties of boron nitride-and carbon-coated iron nanoparticles synthesized by a solid phase reaction. *Journal of Materials Chemistry*, 14(2), 253-257.
- Turgut, Z.,** Scott, J., Huang, M., Majetich, S., & McHenry, M. (1998). Magnetic properties and ordering in C-coated Fe_xCo_{1-x} alloy nanocrystals. *Journal of Applied Physics*, 83(11), 6468-6470.

- Turner, M., & Lieberman, M.** (1999). Hysteresis and the E-to-H transition in radiofrequency inductive discharges. *Plasma Sources Science and Technology*, 8(2), 313.
- Umemoto, M., Udaka, M., Kawasaki, K., & Liu, X.** (1998). Formation of ultrafine powders of binary alloy systems by plasma jet. *Journal of Materials Research*, 13(06), 1511-1516.
- Vajo, J. J., Skeith, S. L., & Mertens, F.** (2005). Reversible storage of hydrogen in destabilized LiBH₄. *The Journal of Physical Chemistry B*, 109(9), 3719-3722.
- Vons, V., Anastasopol, A., Legerstee, W., Mulder, F., Eijt, S., & Schmidt-Ott, A.** (2011). Low-temperature hydrogen desorption and the structural properties of spark discharge generated mg nanoparticles. *Acta Materialia*, 59(8), 3070-3080.
- Vorobev, A., Zikanov, O., & Mohanty, P.** (2008). A co-condensation model for in-flight synthesis of metal-carbide nanoparticles in thermal plasma jet. *Journal of Thermal Spray Technology*, 17(5-6), 956-965.
- Vyas, D., Jain, P., Agarwal, G., Jain, A., & Jain, I.** (2012). Hydrogen storage properties of mg₂ni affected by cr catalyst. *International Journal of Hydrogen Energy*.
- Vyas, D., Jain, P., Khan, J., Kulshrestha, V., Jain, A., & Jain, I.** (2012). Effect of cu catalyst on the hydrogenation and thermodynamic properties of mg₂ni. *International Journal of Hydrogen Energy*, 37(4), 3755-3760.
- Wagemans, R. W., van Lenthe, J. H., de Jongh, P. E., Van Dillen, A. J., & de Jong, K. P.** (2005). Hydrogen storage in magnesium clusters: Quantum chemical study. *Journal of the American Chemical Society*, 127(47), 16675-16680.
- Wang, C., Inazaki, A., Shirai, T., Tanaka, Y., Sakuta, T., Takikawa, H., & Matsuo, H.** (2003). Effect of ambient gas and pressure on fullerene synthesis in induction thermal plasma. *Thin Solid Films*, 425(1), 41-48.
- Wang, P.** (2012). Solid-state thermolysis of ammonia borane and related materials for high-capacity hydrogen storage. *Dalton Transactions*, 41(15), 4296-4302.
- Wang, X., Li, J., Kamiyama, H., & Ishigaki, T.** (2006). Fe-doped TiO₂ nanopowders by oxidative pyrolysis of organometallic precursors in induction thermal plasma: Synthesis and structural characterization. *Thin Solid Films*, 506, 278-282.

- Watanabe, T.,** Nezu, A., Abe, Y., Ishii, Y., & Adachi, K. (2003). Formation mechanism of electrically conductive nanoparticles by induction thermal plasmas. *Thin Solid Films*, 435(1), 27-32.
- Xiaomin, W.,** Bingshe, X., Husheng, J., Xuguang, L., & Hideki, I. (2006). HRTEM and raman study of onion-like fullerenes encapsulated Fe. *Journal of Physics and Chemistry of Solids*, 67(4), 871-874.
- Ye, R., Li, J., & Ishigaki, T.** (2007). Controlled synthesis of alumina nanoparticles using inductively coupled thermal plasma with enhanced quenching. *Thin Solid Films*, 515(9), 4251-4257.
- Yoshida, T., & Akashi, K.** (1981). Preparation of ultrafine iron particles using an rf plasma. *Trans.Jpn.Inst.Met.*, 22(6), 371-378.
- Young, R., & Pfender, E.** (1985). Generation and behavior of fine particles in thermal plasmas—A review. *Plasma Chemistry and Plasma Processing*, 5(1), 1-37.
- Zachariah, M. R., & Carrier, M. J.** (1999). Molecular dynamics computation of gas-phase nanoparticle sintering: A comparison with phenomenological models. *Journal of Aerosol Science*, 30(9), 1139-1151.
- Zaluska, A.,** Zaluski, L., & Ström-Olsen, J. (1999). Synergy of hydrogen sorption in ball-milled hydrides of Mg and Mg₂Ni. *Journal of Alloys and Compounds*, 289(1), 197-206.
- Zaluska, A.,** Zaluski, L., & Ström-Olsen, J. (2001). Structure, catalysis and atomic reactions on the nano-scale: A systematic approach to metal hydrides for hydrogen storage. *Applied Physics A*, 72(2), 157-165.
- Zhang, C.,** Ikeda, M., Isobe, M., Uchikoshi, T., Li, J., Watanabe, T., & Ishigaki, T. (2011). Phase composition and magnetic properties of niobium-iron codoped TiO₂ nanoparticles synthesized in Ar/O₂ radio-frequency thermal plasma. *Journal of Solid State Chemistry*, 184(9), 2525-2532.
- Zhang, M.,** Cushing, B. L., & O'Connor, C. J. (2008). Synthesis and characterization of monodisperse ultra-thin silica-coated magnetic nanoparticles. *Nanotechnology*, 19(8), 085601.

- Zhang, X.**, Yang, R., Yang, J., Zhao, W., Zheng, J., Tian, W., & Li, X. (2011). Synthesis of magnesium nanoparticles with superior hydrogen storage properties by acetylene plasma metal reaction. *International Journal of Hydrogen Energy*, 36(8), 4967-4975.
- Zhang, Y.**, Qi, Y., Zhao, D., Guo, S., Ma, Z., & Wang, X. (2011). An investigation of hydrogen storage kinetics of melt-spun nanocrystalline and amorphous mg₂ni-type alloys. *Journal of Rare Earths*, 29(1), 87-93.
- Züttel, A.** (2004). Hydrogen storage methods. *Naturwissenschaften*, 91(4), 157-172.

APPENDIX

SPARK DISCHARGE SYNTHESIS OF Mg-Ni NANOPARTICLES

A.1 INTRODUCTION

Hydrogen has a great potential as an energy carrier for future applications, as being nonpolluting, harmless and being easily producible by renewable energy sources such as sunlight, wind, geothermal heat, etc. Hydrogen generated from solar energy (or from other renewable energy sources) is a clean and zero emission fuel that could be used for transportation as well as for other mobile and stationary applications. Hydrogen generated in this way can simply be used in internal combustion engines or more efficiently in fuel cells. Unfortunately, the lack of a compact and safe storage method restricts the utilization of hydrogen for such applications (Mandal and Gregory 2010). Presently, the storage of hydrogen gas is largely accomplished within pressurized cylinders which need very high pressures for storage and have low volumetric storage density making such cylinders non suitable for mobile applications. Also, storage in liquid phase needs cryogenic conditions meaning a considerable energy to be used for cooling to a very low temperature of few degrees Kelvin. Solid storage in metal hydrides offers an advantageous storage of hydrogen in comparison to the methods mentioned by having high volumetric storage capacity. However, there are some obstacles that need to be overcome for its practical use, i.e. in hydrogen powered vehicles. These obstacles are mainly the requirements of fast uptake and release rate, long term reversibility and 1 bar desorption temperature below 100°C. For instance, magnesium has a high theoretical storage capacity of 7.6 wt%; but it shows sluggish absorption and desorption kinetics and requires high temperatures to release hydrogen (desorption enthalpy of 75 kJ/mole H₂, 1 bar plateau at 300°C), (Vons *et al.* 2010).

Decreasing the particle size down to nanolevel has a dramatic effect on the chemical and physical properties of the material, i.e. better hydrogen uptake and release kinetics. This behavior can be related with the much larger surface area available for hydrogen uptake, shorter distance for hydrogen to diffuse and elimination of the blocking effect of freshly formed hydrides against further hydrogen diffusion.

Hydrogen absorption and desorption properties can also be favored by making compositional alterations. Such attempts made to improve hydrogen storage characteristics of magnesium and magnesium based hydrides include additions of transition metals as Ni, Cu, Co, Ti, Fe, Pd, Cr, Mn and V (Reilly and Wiswall 1968, Aminorroaya *et al.* 2011, Vyas *et al.* 2012, Liang *et al.* 1999). In addition, oxides such as Fe₃O₄, V₂O₅, Cr₂O₃, TiO₂, and Mn₂O₃ can be used as catalysts to accelerate reaction kinetics (Oelerich *et al.* 2001).

Compositional alterations and structural modifications are usually performed together and for the Mg-Ni based materials, ball milling technique is a widely used technique for this purpose (Zaluska *et al.* 1999). Other methods include melt spinning (Zhang *et al.* 2011), acetylene plasma-metal reaction (Zhang *et al.* 2011), mechanically activated self-propagating high temperature synthesis (Atias-Adrian *et al.* 2011), thin film deposition (Akyıldız and Öztürk 2010), melt infiltration (Jongh *et al.* 2007), solution based methods (Jeon *et al.* 2011), etc.

In this study, spark discharge method was used to synthesize nanosized particles. The method (Schwyn *et al.* 1988) is normally used for aerosol generation based on electrical discharges. This technique has the advantages to yield very fine particles from many different conductive or semi-conductive materials (Vons *et al.* 2011).

In a spark discharge generator, a high voltage, that is larger than the breakdown voltage of the gas between the electrodes, is applied and electrical breakdown occurs. At this short breakdown period, non-conducting gas becomes conducting and it generates the plasma. The breakdown phase is characterized by very high peak values of voltage and current in a very short duration. The energy dissipated in every discharge depends on capacitance (C) and breakdown voltage (V_b) which depends on the electrode gap distance and the pressure. As the distance increases, V_b also increases. Pressure increase also has a similar effect (Tabrizi 2009).

Upon discharge, high energy plasma forms a cylindrical channel at the early stage, with temperature that can reach up to 20,000 K, and it erodes both anode and cathode. Electrodes directly evaporate on the spark contact region, and this is followed by a rapid cooling with adiabatic expansion and radiation (Reinmann *et al.* 1997). Cooling of vapor below the boiling points of constituents are quite fast. Nanoparticles form as a result of this rapid cooling from the gas phase.

The size of resulting particles depends on mainly on discharge characteristics. Increase of breakdown energy causes more material to erode from the electrodes and the probability of collisions of the particles increases correspondingly. This results in larger particle size. Increased gas flow rate is expected to decrease primary particle size by increasing the cooling and dilution rate. But usually there is a limit to this effect (Tabrizi *et al.* 2009).

Production rate mainly depends on frequency and spark discharge energy as well as on physical properties of the electrodes (melting point, thermal conductivity, etc.). High boiling point, high thermal conductivity and high density result in low erosion of the electrode and low production rate.

A variety of metallic nanoparticles have been synthesized via this technique, recent reports include the synthesis of magnesium nanoparticles having 10 nm primary particle size (coated with 2 nm magnesium oxide), palladium particles with 4 nm size, or mixed particles of Cr-Co, Au-Pd and Ag-Pd (Vons *et al.* 2009, Vons *et al.* 2010, Tabrizi 2009). For the synthesis of alloyed nanoparticles, pre-alloyed electrodes or alternatively electrodes (anode, cathode or both of them) having different compositions are used. Electrodes used for this purpose may be in compacted and sintered form.

Nanoparticles generated using electrodes of mixed powders include Mg-Cu and Mn-Al. For the Mg-Cu case (Lei *et al.* 2009), a W rod was used as cathode. Micron-sized Mg and Cu powders were weighed, compressed and used as anode. Considering the stoichiometric composition of Mg₂Cu, the molar ratio of Mg to Cu was set as 2:1. Four phases, i.e. Mg, Mg₂Cu, MgO and MgCu₂ were observed in the product. Main phase was Mg and its content was excessive compared to the starting electrode composition. In another example (Lee *et al.* 2010), alloys Mn_xAl_{100-x} (x=20, 30, 40, 48, 60) and (Mn₂₀Al₈₀)_{0.95}C_{0.05} were prepared by mixing powders of Mn, Al and C in appropriate proportions. The mixtures were weighed and pressed into cylinders (diameter of 25 mm). These cylinders were used as anode. An upper W electrode was used as the cathode. Mn content in the resulting particles was higher compared to the electrode material. It was reported that the difference was greatest for the intermediate compositions. It was concluded that, if vapor pressures of the metals are quite different, this would lead to compositional differences between the electrode material and the resulting particles.

Synthesis of carbon encapsulated metallic nanoparticles has also been reported using spark discharge method. Carbon source may be the electrode (graphite) or the carrier gas (methane, acetylene, etc.). For instance, as reported by Bystrzejewski *et al.* (2005), carbon encapsulated nanoparticles were synthesized using graphite anodes drilled and filled with a mixture of Fe₁₄Nd₂B and graphite. Non-encapsulated metals and graphite which were present in the product were separated using a suitable method. The encapsulated particles were composed of a core 10-30 nm in size and a shell consisting of graphitic layers. It was stated that the increased pressure was beneficial for the graphitization process.

In another study (Si *et al.* 2003), ethanol vapor was used as the carbon source to coat Fe and Ni. Liquid ethanol and argon gas were introduced into the reaction chamber. Fe and Ni were used as anode, and graphite as cathode. Oxides of the metals were not observed, indicating a protective layer had formed during the synthesis. C-Fe had a size of about 6-40 nm and C-Ni was about 30-70 nm.

The current study was undertaken for the purpose of investigating the possibility of the production of Mg-Ni nanoparticles for hydrogen storage purposes. For this purpose, a commercial type spark discharge generator (PALAS GFG-1000) was used. Focus in this study is on the control of composition and production rate.

A.2 EXPERIMENTAL

The commercial spark discharge generator, Palas GFG-1000, was originally designed to produce carbon aerosol using graphite electrodes. But the equipment was adaptable for use of electrodes other than graphite. It basically includes a reaction chamber, two electrodes (anode and cathode), power source, capacitor and gas inlet/outlet. Generator includes a belt driven mechanism to hold the gap distance constant during the operation. It has the ability to produce nanoparticles down to 3-5 nm primary size. A schematic drawing of the generator is given in Figure A.1.

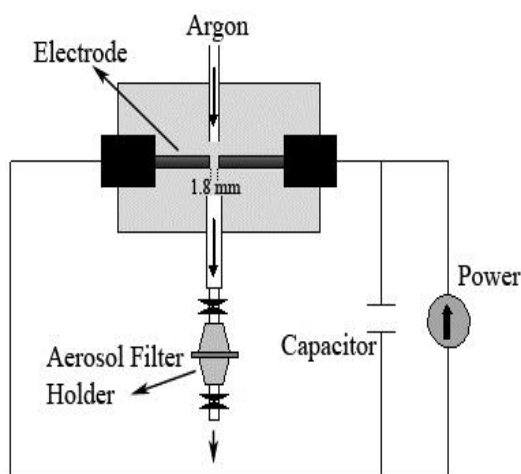


Figure A.1 Schematic drawing of the spark discharge generator
(Adapted from Tabrizi *et al.* 2009).

Nanoparticles generated were collected by means of a filter (PALL Emfab, 47 mm diameter, 99.95% aerosol retention ability). The filter was inserted into an air-tight purpose-built filter holder. The holder had two valves one at the inlet and the other at the outlet, so that the holder could be moved into the glovebox without exposing the collected powders to air.

A.3 RESULTS & DISCUSSION

First, graphite electrodes (6 mm diameter) were used so as to check the size and the morphology of the resulting particles. SEM images of powders collected on membrane filter are seen in Figure A.2. Spark frequency was 250 Hz and argon flow rate was 5.3 slpm. Electrode gap distance was kept constant at 1.8 mm. Primary particle size was 17.6 nm with a standard deviation of 3.7 nm (over 30 particles excepting large particles seen in Figure A.2).

So as to produce metallic nanopowders, graphite electrodes were replaced with the relevant metals. Nickel electrodes were obtained by compacting Ni powder into 6 mm rods which were then sintered at 700°C. The generator was operated in the same conditions as above. The resulting Ni nanoparticles had a mean size of 25 nm. These primary particles were highly agglomerated, Figure A.3(a). Thus there were also larger particles in sintered form which were approximately 250 nm in size, Figure A.3(b). These have probably originated from smaller primary particles due to high degree of agglomeration and coagulation. At the same time, there was rare occurrence of micron size particles. These were believed to originate from melted and condensed droplets, which were not able to evaporate.

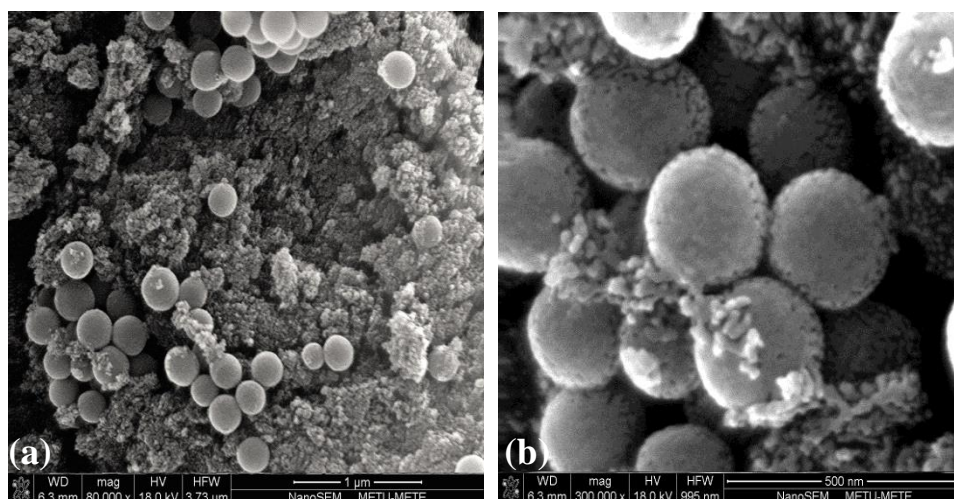


Figure A.2 SEM images of carbon nanoparticles. At some regions, large (~ 250 nm in size) particles were also present, (a) and (b).

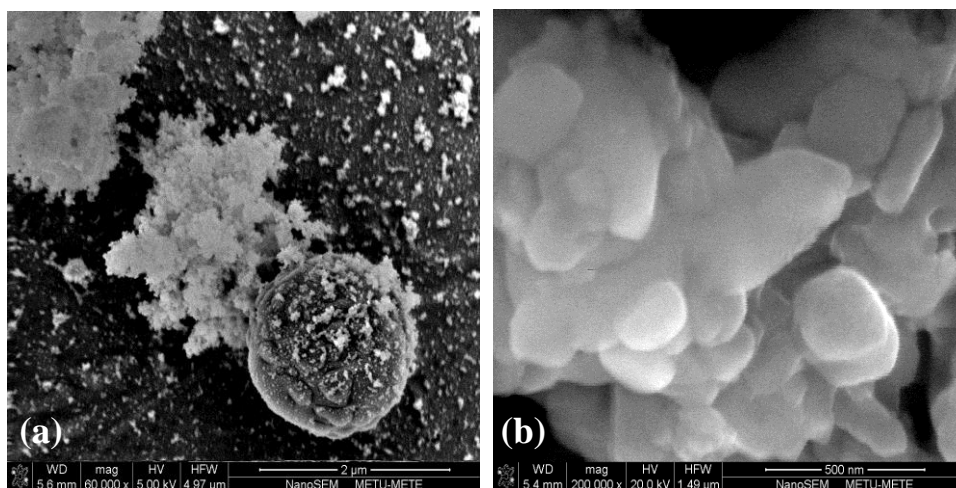


Figure A.3 SEM images of nickel nanoparticles. Nanoparticles were observed either in cloud-like assemblies (a) with average size of ~25 nm or as room temperature sintered particles (b) with average size of ~250 nm.

For Mg nanoparticles, Mg electrodes were machined from commercial grade magnesium plates, resulting in rods of 6 mm in diameter. The spark generator using these electrodes yielded particles with an average size of 12 nm with a standard deviation of 3 nm (over 50 particles). SEM images of these particles are shown in Figure A.4. XRD patterns of the powders (together with membrane filter) are given in Figure A.5. It is seen that the pattern comprise peaks that are consistent with MgO. The powders were weighed in glovebox and also outside where there was no increase in weight indicating that they had been already oxidized during the synthesis. There was also a slight shift in 2-theta values the reason of which was not explored as it might be due to errors during the measurement.

In order to investigate the effect of flow rate and electrode geometry on the product yield, additional experiments were conducted. First, magnesium electrodes having 6 mm diameters were used and argon flow rate was altered from 4 slpm to 7 slpm. As seen in Figure A.6, the amount of powder produced decreased with increase in the argon flow rate. This is probably due to the cooling effect of the argon gas sent into the spark zone which decreases the evaporation efficiency of the process. For all cases, the rate of nanoparticle production was within 3–5 mg/hour.

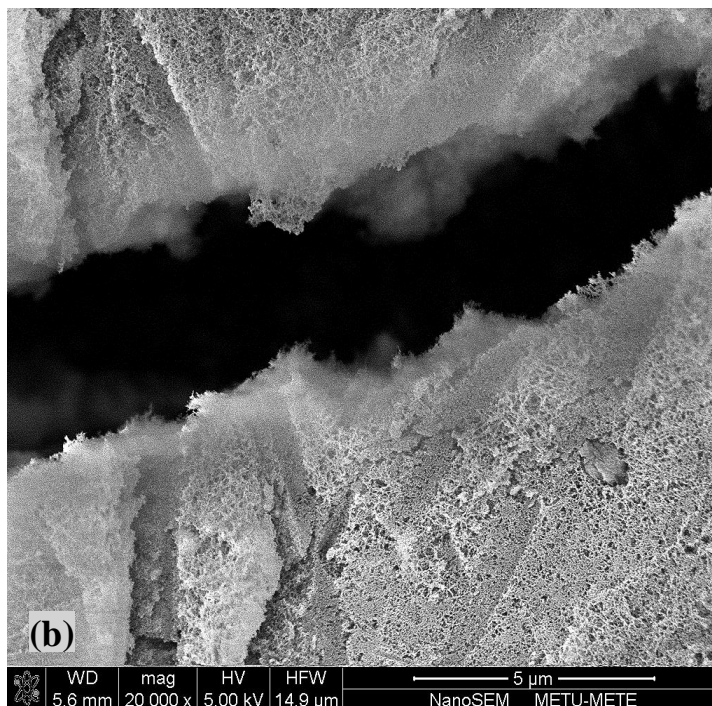
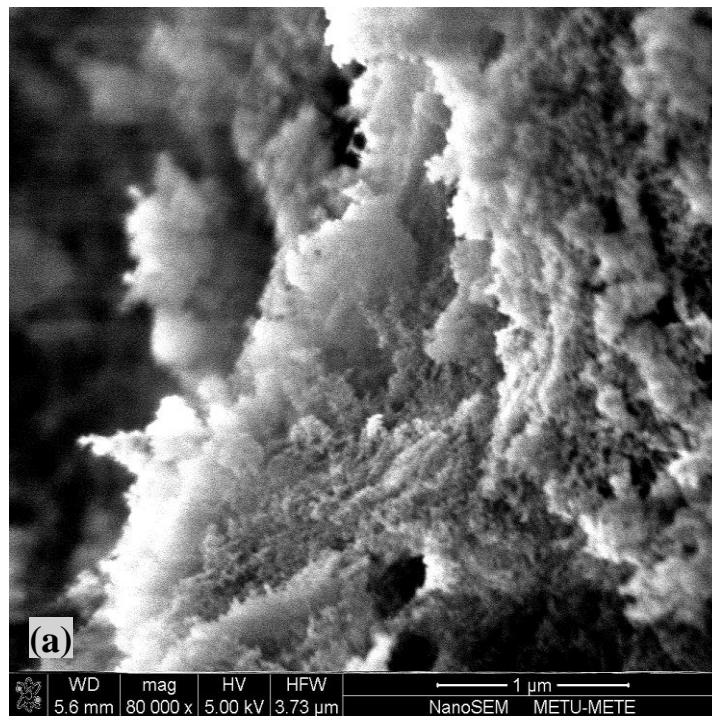


Figure A.4 SEM images of nanoparticles generated from magnesium electrodes, (a) and (b).

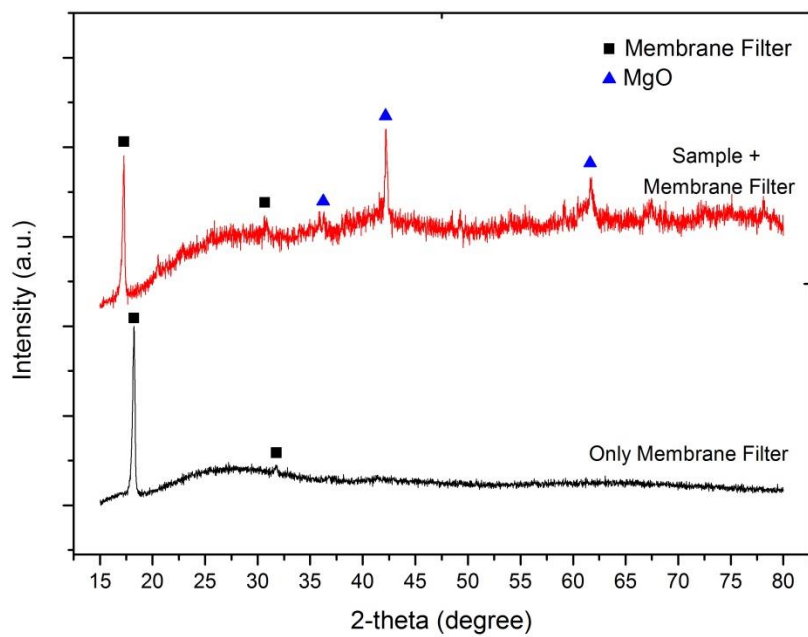


Figure A.5 XRD patterns of the powders on membrane filter and membrane filter alone.

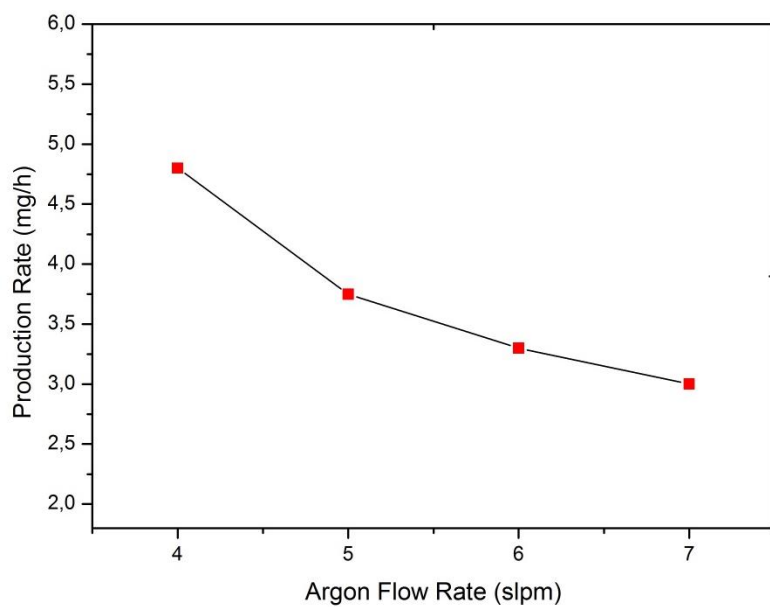


Figure A.6 Effect of argon flow rate on the production rate.

In a subsequent experiment, one of the electrodes was machined down to 2 mm at its tip. This electrode was used as cathode. Electrode configuration was then reversed in a separate experiment, i.e. Mg with 2 mm tip was made anode. Mass differences of the electrodes before and after the experiments were recorded so as to follow the rate of evaporation (Figure A.7). When used as cathode, it was noted that more material was eroded from the cathode. When used as anode, it was seen that the evaporation loss was higher at the cathode. The mass difference was higher in the latter case compared to the previous experiment. Thus the total amount of evaporation was higher in the second test when 2mm electrode was anode. This might be explained with the fact that, cations in the plasma move towards the cathode and anions to the anode. Cations have higher mass and correspondingly have higher energy, so energy transfer in a single spark to the electrode is expected to be higher for the cathode.

The use of different diameter anode and cathode might affect the discharge process. When both electrodes have similar diameters, contact points on the electrode surface change randomly after each spark. Overall, spark contact points spread all over the electrode surface. Since in every spark formation contact point changes, heat is more homogeneously distributed over the electrode tip providing more effective cooling of the electrode. When one of the electrodes has smaller tip, the contact point of spark is restricted. This also restricts the contact point at the counter electrode having larger diameter. This probably causes temperature increase around the spark contact regions by decreasing the cooling efficiency. A photograph of the electrode tip which was taken after the production run of approximately 24 hours is given in Figure A.8.

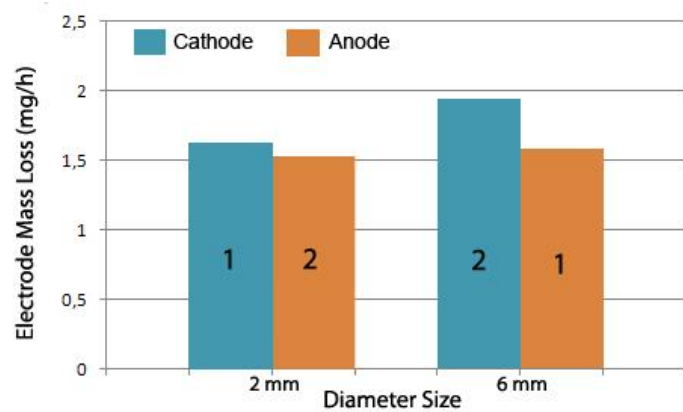


Figure A.7 Electrode mass loss values for the 4-6 mm Mg electrode pair (1: first experiment and 2: second experiment).

If anode and cathode were made of different metals, it might be possible to generate nanoparticles of different compositions. Composition control involving multicomponent electrodes could be problematic for elements having different physical properties (vapor pressure, thermal conductivity, etc.) as each would evaporate with different rates. The fact that anode and cathode have different evaporation rates and this rate could also be affected with modifications in the electrode diameter would enable to modify the composition of the product.

Size of powders synthesized in spark discharge method is quite small which is smaller than most of the other plasma techniques. However, preventing the oxidation of powders requires extensive precautions. Also, production rate is rather low making this technique impractical for large scale and cost-effective applications, especially compared to other plasma techniques as RF thermal plasma and DC thermal plasma.

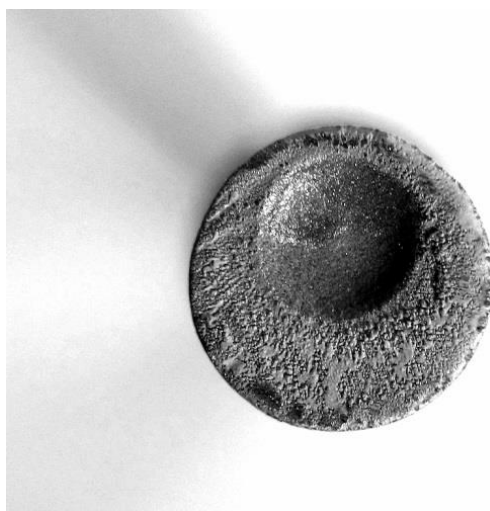


Figure A.8 A photograph of the electrode having 6 mm diameter, image was taken after the experiment, where the counter electrode had 2 mm diameter.

A.4 CONCLUSIONS

The current study shows that, spark discharge method can be used to synthesize very fine particles, usually less than 50 nm in size. This was shown for graphite and nickel. However, the synthesis of magnesium nanoparticles was not possible due to the high reactivity of Mg which leads to the formation of MgO. The use of this method seems to be practical for the synthesis of noble metals, especially for applications not requiring large amount of materials, e.g. catalysts. A limited control of the composition is also possible when mixtures of different elements are desired in product; electrode geometry and polarity can be changed for this purpose.

A.5 REFERENCES

- Akyıldız, H., & Öztürk, T.** (2010). Hydrogen sorption in crystalline and amorphous Mg–Cu thin films. *Journal of Alloys and Compounds*, 492(1), 745-750.
- Aminorroaya, S., Ranjbar, A., Cho, Y., Liu, H. K., & Dahle, A. K.** (2011). Hydrogen storage properties of mg-10 wt% ni alloy co-catalysed with niobium and multi-walled carbon nanotubes. *International Journal of Hydrogen Energy*, 36(1), 571-579.
- Atias-Adrian, I. C.,** Deorsola, F., Ortigoza-Villalba, G., DeBenedetti, B., & Baricco, M. (2011). Development of nanostructured mg₂ni alloys for hydrogen storage applications. *International Journal of Hydrogen Energy*, 36(13), 7897-7901.
- Bystrzejewski M et al.,** Arc plasma route to carbon encapsulated magnetic nanoparticles for biomedical applications, *Sensors and Actuators B* 109 (2005).
- Jeon, K., Moon, H. R.,** Ruminski, A. M., Jiang, B., Kisielowski, C., Bardhan, R., & Urban, J. J. (2011). Air-stable magnesium nanocomposites provide rapid and high-capacity hydrogen storage without using heavy-metal catalysts. *Nature Materials*, 10(4), 286-290.
- Jongh, P. E. d.,** Wagemans, R. W., Eggenhuisen, T. M., Dauvillier, B. S., Radstake, P. B., Meeldijk, J. D., Jong, K. P. d. (2007). The preparation of carbon-supported magnesium nanoparticles using melt infiltration. *Chemistry of Materials*, 19(24), 6052-6057.
- Lee J G,** Synthesis of Mn-Al alloy nanoparticles by plasma arc discharge, *Thin Solid Films* 2010.

- Lei J P**, Formation and hydrogen storage properties of in situ prepared Mg–Cu alloy nanoparticles by arc discharge, *J Hydrogen Energy* 34 ; 8127-8134.
- Liang, G.**, Huot, J., Boily, S., Van Neste, A., & Schulz, R. (1999). Hydrogen storage properties of the mechanically milled MgH₂V nanocomposite. *Journal of Alloys and Compounds*, 291(1), 295-299.
- Mandal, T.**, & Gregory, D. (2010). Hydrogen: A future energy vector for sustainable development. *Proceedings of the Institution of Mechanical Engineers, Part C: Journal of Mechanical Engineering Science*, 224(3), 539-558.
- Oelerich, W.**, Klassen, T., & Bormann, R. (2001). Metal oxides as catalysts for improved hydrogen sorption in nanocrystalline mg-based materials. *Journal of Alloys and Compounds*, 315(1), 237-242.
- Reilly Jr, J. J.**, & Wiswall Jr, R. H. (1968). Reaction of hydrogen with alloys of magnesium and nickel and the formation of Mg₂NiH₄. *Inorganic Chemistry*, 7 112254-2256.
- Reinmann, R.**, and M. Akram. "Temporal investigation of a fast spark discharge in chemically inert gases." *Journal of Physics D: Applied physics* 30.7 (1997): 1125.
- Schwyn, S., E.** Garwin, and A. Schmidt-Ott. "Aerosol generation by spark discharge." *Journal of Aerosol Science* 19.5 (1988): 639-642.
- Si P Z et al.**, Synthesis and characteristics of carbon-coated iron and nickel nanocapsules produced by arc discharge in ethanol vapor, *Carbon* 41 247-251 (2003).
- Tabrizi N S**, PhD Thesis, Delft University of Technology, Delft, 2009.
- Tabrizi, N. S.**, et al. "Synthesis of mixed metallic nanoparticles by spark discharge." *Journal of nanoparticle Research* 11.5 (2009): 1209-1218.
- Tabrizi, Nooshin Salman**, et al. "Generation of nanoparticles by spark discharge." *Journal of Nanoparticle Research* 11.2 (2009): 315-332.
- Vons V A**, Leegwater H, Legerstee W J, Eijt S W H, Schmidt-Ott a, Hydrogen storage properties of spark generated Pd nanoparticles. In *J Hydrogen Energy* 35 ; 5479-5489, 2010.
- Vons, V. A.**, et al. "Hydrogen storage properties of spark generated palladium nanoparticles." *International Journal of Hydrogen Energy* 35.11 (2010): 5479-5489.

- Vons, V. A.**, et al. "Low-temperature hydrogen desorption and the structural properties of spark discharge generated Mg nanoparticles." *Acta Materialia* 59.8 (2011): 3070-3080.
- Vons, Vincent A.**, et al. "Silicon nanoparticles produced by spark discharge." *Journal of Nanoparticle Research* 13.10 (2011): 4867-4879.
- Vyas, D.**, Jain, P., Agarwal, G., Jain, A., & Jain, I. (2012). Hydrogen storage properties of Mg₂Ni affected by Cr catalyst. *International Journal of Hydrogen Energy*
- Zaluska, A.**, Zaluski, L., & Ström-Olsen, J. (1999). Synergy of hydrogen sorption in ball-milled hydrides of Mg and Mg₂Ni. *Journal of Alloys and Compounds*, 289(1), 197-206.
- Zhang, Xuanzhou**, et al. "Synthesis of magnesium nanoparticles with superior hydrogen storage properties by acetylene plasma metal reaction." *International Journal of Hydrogen Energy* 36.8 (2011): 4967-4975.
- Zhang, Yanghuan**, et al. "An investigation of hydrogen storage kinetics of melt-spun nanocrystalline and amorphous Mg₂Ni-type alloys." *Journal of Rare Earths* 29.1 (2011): 87-93.